UNIVERSITÀ DEGLI STUDI DI NAPOLI FEDERICO II

Ph.D. School in
EARTH SCIENCES
XXVI Cycle

Ph.D. Thesis

THERMOGRAPHIC DATA INVERSION PROCEDURES. ARCHITECTURAL AND ENVIRONMENTAL APPLICATIONS

Cecilia Mancini

Supervisor

Prof. Rosa Di Maio

Co-supervisor

Dr. Ester Piegari

Table of contents

Introduction

In last decades, the use of non-invasive measurement techniques is increasing and spreading in many diverse fields of applied physics. In particular, Infrared thermography (IRT) has emerged among nondestructive evaluation methods to determine the integrity of a structure and to detect and characterize buried objects. IRT is a fast and contactless technique able to provide images of the surface temperature distribution of the investigated structure by measuring the infrared radiation emitted by the structure itself. Due to the great informative content of thermal images, analysis of maps of surface temperature (thermograms) is widely used not only in monitoring thermal conditions of structures, buildings, engines, electric circuits and components, but also in monitoring of volcanic activity and geothermal phenomena, soil, river and coastal pollution and to control human and animal bodies.

The general objectives of this thesis are the development, testing and application of numerical methods for solving heat transfer problems and analyzing thermographic data in different application fields of thermography.

First, Finite Difference approximations are used to solve one- and two- dimensional heat conduction problems and to simulate the thermal response of non-homogeneous structures with variable thermal conductivity and out of equilibrium. The implemented numerical codes are tested on the thermal response of two specimens made of different types of masonry structures with enclosed defects simulating common building degradation causes, such as voids, detachments, and variation in porosity. Then, two examples of application of the codes to different study areas are discussed in order to

show how the proposed numerical method can be applied for obtaining helpful information on the state of conservation of ancient buildings. The first case study is related to a quantitative analysis of experimental data acquired in the Marcus Fabius Rufus' House located in the archaeological area of Pompei (Naples, Italy), where IRT survey was conducted in combination with a ground-penetrating radar prospecting in collaboration with a research team of Roma Tre University (Rome, Italy). The second case study is related to a quantitative analysis of thermographic data acquired on the Dome of Magdeburg (Germany) by the research team of Dr. Maierhofer. This analysis has been conducted during a period of two months spent at the Federal Institute for Materials Research and Testing (BAM) in Berlin as a visiting student.

In both these cases, heat propagates from the surface to the interior and the developed numerical methods are used to provide synthetic curves that are compared with experimental thermal decays of the surface of the investigated walls.

In this thesis, the developed numerical algorithms are also used to study conductive heat problems where the point of view is upside down. Indeed, they are applied in the attempt to reproduce the thermal evolution of the Phlegraean magmatic system (Naples, southern Italy) during the last 40,000 years. In this case, the thermal source is a magma chamber and, therefore, heat propagates from the interior to the surface. Thus, the main aim is to verify if the high temperatures measured in the geothermal wells drilled inside the Campi Flegrei caldera can reasonably be reproduced under the assumption of heat loss of a magma chamber through conduction in inhomogeneous media.

Generally, thermographic data are integrated in surveillance systems of active volcanic areas and are mainly used to report absence of eruptive activity, gaseous emission and lava effusion. During the PhD period, a collaboration is started with a research team of the National Institute of Geophysics and Volcanology (INGV), Naples branch, to investigate possible quantitative uses of thermal images. In particular, a new method for analyzing long-term time series of thermographic data has been developed in order to quantify information from continuous IR data recorded by permanent network located at the monitoring station of Pisciarelli (Campi Flegrei).

Finally, a new approach to invert IRT data has been searched as inverse procedures are of fundamental importance in applied geophysics allowing determination of physical parameters from measured data. Inverse thermal problems are really difficult to solve, since they are often ill-posed due to the high sensitivity to input errors, the large number of parameters to be estimated, and/or the infinite number of possible solutions of which the "right" one has to be found. Inspired by the Induced Polarization experiments, whose discharge curves can be described by a sum of decreasing exponentials and, therefore, analyzed by the Prony's method, in this thesis the idea of using the Prony's algorithm for the quantitative interpretation of cooling transients is presented and discussed.

Chapter I

Infrared Thermography

Infrared thermography (IRT) is a fast and contactless technique, which consists in measuring the infrared radiation emitted by materials (or structures) using a radiometer, i.e. an IR camera.

The radiometer converts the energy radiated from media in the infrared band of the electromagnetic spectrum into an electric signal and finally into a visible image (thermogram). The energy emitted by a body is mainly a function of its surface temperature and so infrared thermography may be considered as a two-dimensional technique of temperature measurement [Meola and Carlomagno, 2004].

Analysis of thermograms is successfully applied in many fields, such as non-destructive testing in civil and aeronautic engineering [Maierhofer et al., 2004; Meola et al., 2005; Grinzato et al., 2007; Dumoulin et al., 2009], cultural heritage [Vavilov et al., 1997; Carlomagno and Meola, 2001; Grinzato et al., 2002; Avdelidis and Moropoulou, 2004; Di Maio et al., 2012a], medicine [Hooshmand et al., 2001a, b; Di Carlo, 2004; Gerasimova et al., 2012; Zore et al., 2012], and agriculture [Wisniewski et al., 1997; Catena and Catena, 2001; Bucur, 2003]. Other applications of the IRT methodology concern environmental studies, such as monitoring of sea, river and coastal pollution [Lega et al., 2010, 2012], of landfill gas emission [Treagoureas et al., 1999; Desideri et

al., 2007], as well as volcanoes and geothermal phenomena [Harris et al., 2000; Spampinato et al., 2011; Sansivero et al., 2012].

In the following sections a description of infrared thermography principles and techniques is presented.

1.1 Principles of Infrared Thermography

Any object emits electromagnetic energy proportional to its surface temperature. The energy emitted is called the spectral radiance and is defined by the Planck's law, which describes the spectral distribution of the radiation intensity from a blackbody:

$$E_{\lambda b}(t) = \frac{C_1}{\lambda^5\left(e^{C_2/\lambda T}-1\right)} \tag{1.1}$$

where $E_{\lambda b}$ is the blackbody monochromatic radiation intensity [W/m^{2}μm], T is the absolute temperature of the blackbody [K], λ is the wavelength of the emitted radiation [μm], C_1 and C_2 are, respectively, the first and second radiation constants, i.e. $C_1 = 2\pi hc^2 = 3.742x10^{-16}$ W/m^2 and $C_2 = hc/k = 1.4388x10^{-2}$ mK, with h Planck's constant ($=6.626x10^{-34}$Js), c speed of light in vacuum ($=3x10^8$ m/s) and k Boltzmann's constant ($=1.381x10^{-23}$J/K).

The Fig. 1.1 shows the spectral distributions $E_{\lambda b}$ of a blackbody, determined by Eq. (1.1), versus wavelength λ for different temperatures T.

By integrating the Planck's law over the entire spectrum, the total hemispherical radiation intensity is obtained for a blackbody:

$$E_b = \int_0^\infty E_{\lambda b}\, d\lambda = \sigma T^4 \tag{1.2}$$

where σ ($=5.67x10^{-8}$ W/m^{2}K^4) is the Stefan-Boltzman constant.

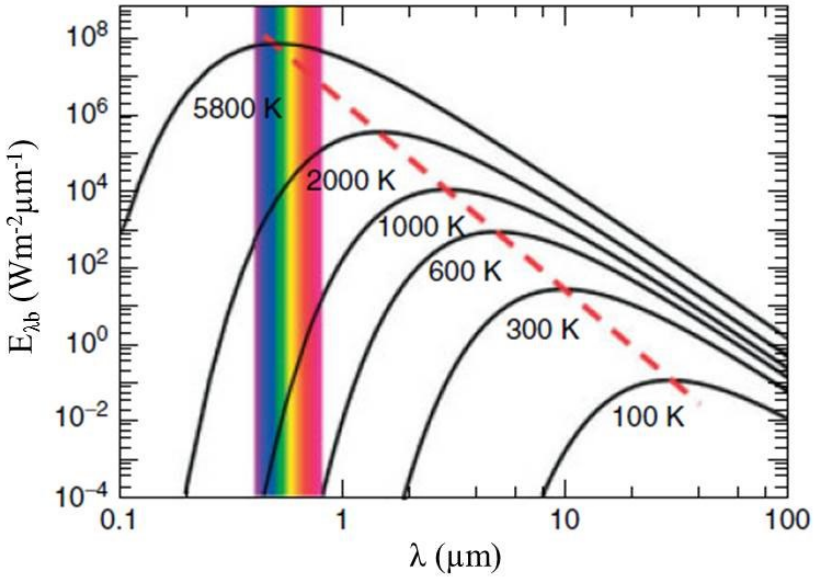

Figure 1.1: Spectral distributions of a blackbody according to Planck's law [from Vollmer and Möllmann, 2010].

Eq. (1.1) allows determining the radiation emitted for fixed temperature and wavelength from a blackbody. However, under real conditions, the Planck's law describes only an upper limit of the thermal flux density because all physical bodies have limited absorbing capacity [De Witt and Nutter, 1988; Siegel and Howell, 2001; Minkina and Dudzik, 2009]. In particular, in IR imaging, where real bodies are investigated, it is not possible to detect radiation of the whole spectrum but rather the radiation in a spectral range [Minkina and Dudzik, 2009]. This fraction of the blackbody spectral radiance is given by the property of the body surface called the spectral emissivity coefficient, ε_λ:

$$\varepsilon_\lambda = \frac{E_\lambda}{E_{\lambda b}} \quad , \tag{1.3}$$

which depends on λ, T, viewing angle, material type and surface condition [Vollmer and Möllmann, 2010]. Therefore, for real bodies, Eq. (1.1) can be rewritten by multiplying its second term by ε_λ.

Since the emissivity describes the fraction of blackbody radiant emittance produced by a real object at the same temperature and for the same spectral and directional conditions

of the blackbody, the knowledge of the emissivity of the body under test permits to calculate its temperature from the emitted thermal radiation [Avdelidis and Moropoulou, 2003; Minkina and Dudzik, 2009; Ciocia and Marinetti, 2012].

The energy really detected depends not only on the emissivity coefficient of the investigated surface but also on the detector, the optics of the camera and the environment. In particular, a fraction of energy may be absorbed by the atmosphere between the object and the camera, and/or added as reflected by the surface from the surroundings [Meola and Carlomagno, 2004]. To take into account these factors, calibration of the system has to be performed. The calibration function, i.e.

$$E = \varepsilon \frac{A}{\left(e^{B/T} - C\right)}, \tag{1.4}$$

simulates real operating conditions and relates the real amount of detected energy E to the emissivity coefficient ε and to the surface temperature T of the object through the calibration constants A, B and C, which take into account Planck's constant as well as spurious quantities of energy from, or to, the environment [Meola and Carlomagno, 2004; Minkina and Dudzik, 2009; Vollmer and Möllmann, 2010].

1.2 Thermographic techniques

Infrared Thermography techniques generally bases on two approaches: passive and active [Ibarra-Castanedo et al., 2007a]. In passive thermography, features of interest are naturally at temperatures higher or lower than the surrounding temperature, while in active thermography, the thermal contrasts are induced by artificial energy sources.

A wide variety of energy sources can be used to induce thermal contrasts between defective and non-defective zones. They can be divided in:

- external: if the energy is released to the surface and then propagated through the material until it encounters an anomaly. External excitation is typically performed with optical devices such as photographic flashes (for heat pulsed stimulation) or halogen lamps (for periodic or step heating);

- internal: if the energy is injected into the specimen in order to stimulate exclusively the defects. Internal excitation can be achieved by means of mechanical oscillations, with a sonic or ultrasonic transducer for both burst and amplitude modulated stimulation.

Among various modes of thermal stimulation, lock-in thermography, pulse and long pulse thermography are the most common techniques, and, therefore, they will be briefly illustrated in the following. In particular, more details will be given about pulse thermography as it represents the technique used in this thesis work.

1.2.1 Lock-in thermography

Lock-in thermography (LT) technique consists of stimulating periodically a specimen surface by one or several modulated heating sources, e.g. halogen lamps, for injecting thermal waves (with preserved frequency and shape) into the specimen (Fig. 1.2). The thermal response is recorded at the same time using an infrared camera, which is able to monitor the entire surface, and is decomposed to extract the amplitude and the phase of the modulation [Carlomagno and Berardi, 1976; Kuo et al., 1988; Busse et al., 1992; Busse, 1994;].

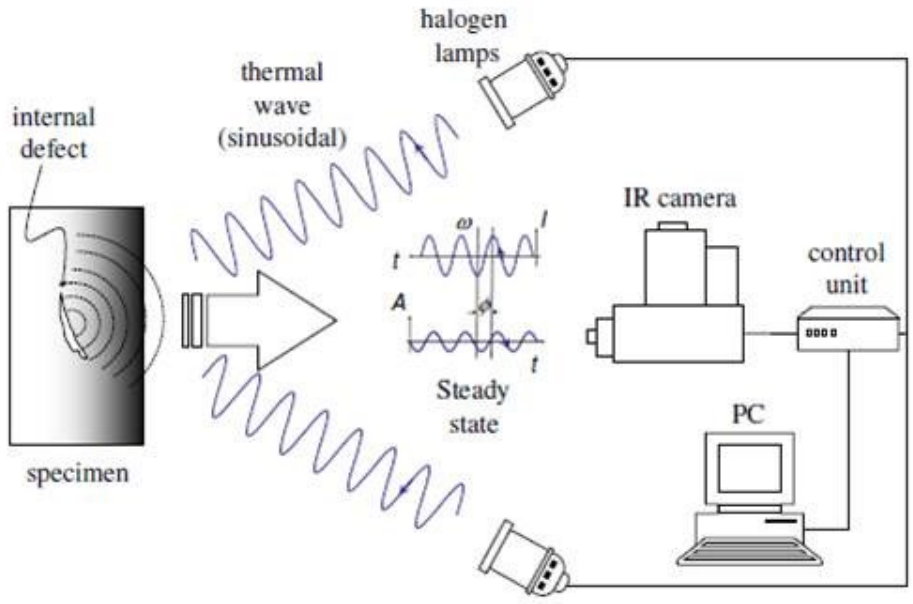

Figure 1.2: Experimental set-up for lock-in thermography [from Ibarra-Castanedo et al., 2007a].

Heat diffusion through a solid is a complex 3D problem that can be described by the Fourier's law of the heat diffusion:

$$\nabla^2 T - \frac{1}{\alpha}\frac{\partial T}{\partial t} = 0\,, \tag{1.5}$$

where $\alpha = k/\rho c_p$ [m^2/s] is the thermal diffusivity of the inspected material, k [W/mK] its thermal conductivity, ρ [kg/m^3] its density and c_p [J/kgK] its specific heat at constant pressure [Carslaw and Jaeger, 1986]. This equation will be derived in the next Chapter (sec. 2.1).

The 1D solution of the heat equation for a periodic thermal wave propagating through a semi-infinite homogeneous material can be expressed as:

$$T(z,t) = T_0 e^{-z/\mu}\cos\left(\frac{2\pi z}{\lambda} - \omega t\right)\,, \tag{1.6}$$

where T_0 [K] is the initial change temperature produced by the heat source, $\omega = 2\pi f$ [rad/s] is the modulation frequency, f [Hz] is the frequency, $\lambda = 2\pi\mu$ [m] is the thermal wavelength and μ [m] is the thermal diffusion length, which provides the rate of decay of the thermal wave when it travels through the material and is defined as [Meola and Carlomagno, 2004]:

$$\mu = \sqrt{\frac{2\alpha}{\omega}} = \sqrt{\frac{\alpha}{\pi f}}\,. \tag{1.7}$$

The strength of LT is that the amplitude does not depend on signals superposition due to reflection effects, and the phase angle is also independent of local power density and thermal emission coefficient [Busse and Rosencwaig, 1980]. From the amplitude images, it is possible to evaluate the diffusion length, μ [Eq. (1.7)], while from the phase images it is possible to calculate the maximum depth, p, which is given by [Busse, 1979; Thomas et al., 1980; Letho et al., 1981; Bennett and Patty, 1982]:

$$p = 1.8\sqrt{\frac{\alpha}{\pi f}} = 1.8\mu\ . \tag{1.8}$$

Inspection by lock-in thermography is in general slower than other approaches because tests for every investigation depth and stabilization waiting time are required before reaching a permanent regime. However, the energy required to perform a LT inspection is generally less than in other active techniques; this is very important if a low power source is available or if special care has to be given to the inspected part, e.g. cultural heritage pieces, works of art, frescoes, etc. [Wu and Busse, 1998; Carlomagno and Meola, 2002].

Typical applications of the LT technique include measurements of thickness and/or density and/or porosity of ceramic coatings [Rantala et al., 1996; Wu et al., 1996a], detection of delaminations [Wu, 1994], determination of fibre orientation in composites [Karpen et al., 1994] and inspection of aircraft components [Wu et al. 1996b, 1998].

1.2.2 Pulse thermography

Although LT data analysis permits to evaluate the depth of thermal anomaly sources [Eq. (1.8)], investigation depth of the order of 10 centimetres could be reached only increasing the oscillation period. For this reason, pulse thermography (PT) investigations are preferred when a deeper investigation is needed and, therefore, it is used for investigating thick masonry walls [Maierhofer et al., 2006; Meola, 2007; Carlomagno et al., 2011].

With PT the object under test is stimulated by a heating pulse (Fig. 1.3a), through flash lamps, and its temperature transient is recorded during the cooling phase (Fig. 1.3c). Once the thermal wave reaches the specimen's surface, a thermal front travels from the surface through the specimen. As time spends, the surface temperature distribution will decrease uniformly if the heating is uniform and the material is homogeneous. Conversely, the presence of discontinuities (e.g. pores, delaminations, disbonds, fiber breakages, inclusions, etc.) produces localized temperature differences on the surface because of interferences with the heat flow (Fig. 1.3b).

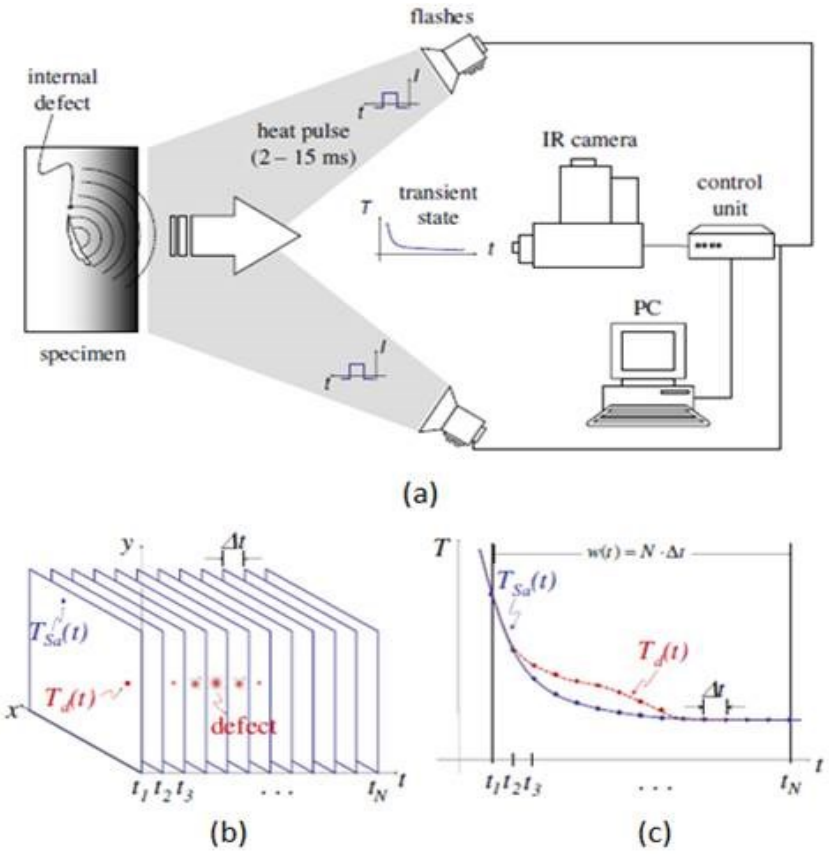

Figure 1.3: (a) Experimental set-up example of pulsed thermography. Temperature evolution: (b) acquisition data as a 3D matrix of images, (c) cooling transient for defective (red line) and non-defective (blue line) pixels [from Ibarra-Castanedo et al., 2007a].

Generally, a shallow defect becomes visible earlier than a deeper one and a large defect produces a higher temperature contrast than a smaller one. In first approximation, the relationship that relates the observation time t and the subsurface defect depth z is given by:

$$t \sim \frac{z^2}{\alpha} \quad . \tag{1.9}$$

Information about defect parameters, such as size, depth and thermal resistance, can be obtained by applying post-processing procedures to the thermograms.

Observation with pulsed thermography can be performed in two different modes: reflection and transmission (Fig. 1.4). In reflection mode the thermal source and the IR

camera are located on the same side of the investigated object; in transmission mode, instead, the detector views the opposite face, e.g. opposite to heating/cooling source. Generally, the reflection mode is used for detection of defects located close to the heated surface, while the transmission mode allows for detection of defects close to the opposite surface (due to the spreading effect of the energy propagating within the specimen) [Maldague, 2002]. However, in real applications, often is not possible to access at the rear side, so the reflection mode have to be used with both the infrared camera and the heating source on the same side [Meola and Carlomagno, 2004].

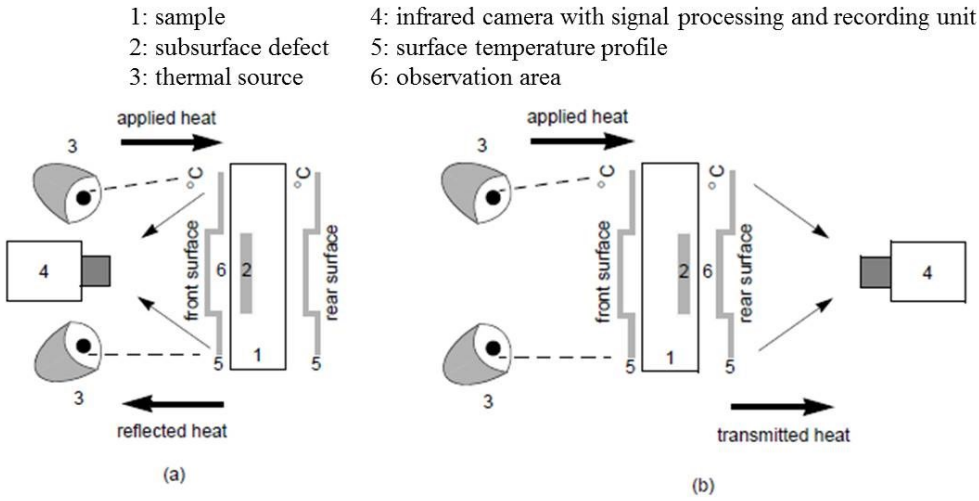

Figure 1.4: Observation methods for pulse thermography technique: (a) in reflection, (b) in transmission.

The thermal energy propagation within the material under inspection can be described by the Fourier diffusion equation [Eq. (1.5)]. The 1D solution for propagation of a heating pulse in a semi-infinite isotropic solid by conduction has the form:

$$T(z,t) = T_0 + \frac{Q}{\sqrt{k\rho c_p \pi t}} e^{-z^2/4\alpha t}, \tag{1.10}$$

where Q [J/m^2] is the energy absorbed by the surface and T_0 [K] is the initial temperature. This equation is only an approximation of the complex 3D diffusion

problem. For this reason, many data processing techniques were developed based on this simplified formula in order to perform quantitative data analysis (see Paragraph 1.3).

Pulsed thermography inspection is quick (from few seconds for high conductivity materials to a few minutes for low conductivity materials) and easy to employ, but it is affected by local variations of the emissivity and non-uniform heating that can mask the defect visibility [Maldague, 2002; Meola and Carlomagno, 2004; Sun, 2006]. Moreover, high computational costs are required for quantitative data interpretation.

The surface heating may be improved by using the lateral heating (LHT) method [Grinzato et al., 1998] or a set of automated routines that automatically remove any non-uniformity caused by the flash heating [Pickering and Almond, 2008].

If the pulse is long compared to the observation time and acts as a temporal step function (long pulse), the technique is called time-resolved-infrared (TRIR) because the temperature is monitored as it evolves during and after the heating process [Aamodt et al., 1990]. In this case, the heating is generally performed by lamps, flash lamps, scanning lasers or hot air jets, while the cooling can be got by cold air jets.

Various configurations of the heating source are possible:

(a) Point inspection: only a point of the object's surface is heated with a laser or a focused light beam; it has the advantage of uniform heating, but the inspection process is slow due to the necessity to move the inspection head to fully examine the surface (Fig 1.5a).

(b) Line inspection: a vertical or horizontal line is projected to the surface being inspected using line lamps, heated wire, scanning laser, line of air jets (cool or hot); it permits a fast inspection rate (up to 1 m/s) and a good heating uniformity thanks to the lateral motion of the specimen, but only a part of the temperature history curve is available because of this motion and the fixed distance between thermal stimulation and temperature signal pick-up (Fig. 1.5b).

(c) Surface inspection: an area of the inspected object is heated at once by using lamps, flash lamps, scanning laser; the complete analysis of the phenomenon is possible since the whole temperature history curve is recorded, but the heating is not uniform (Fig 1.5c).

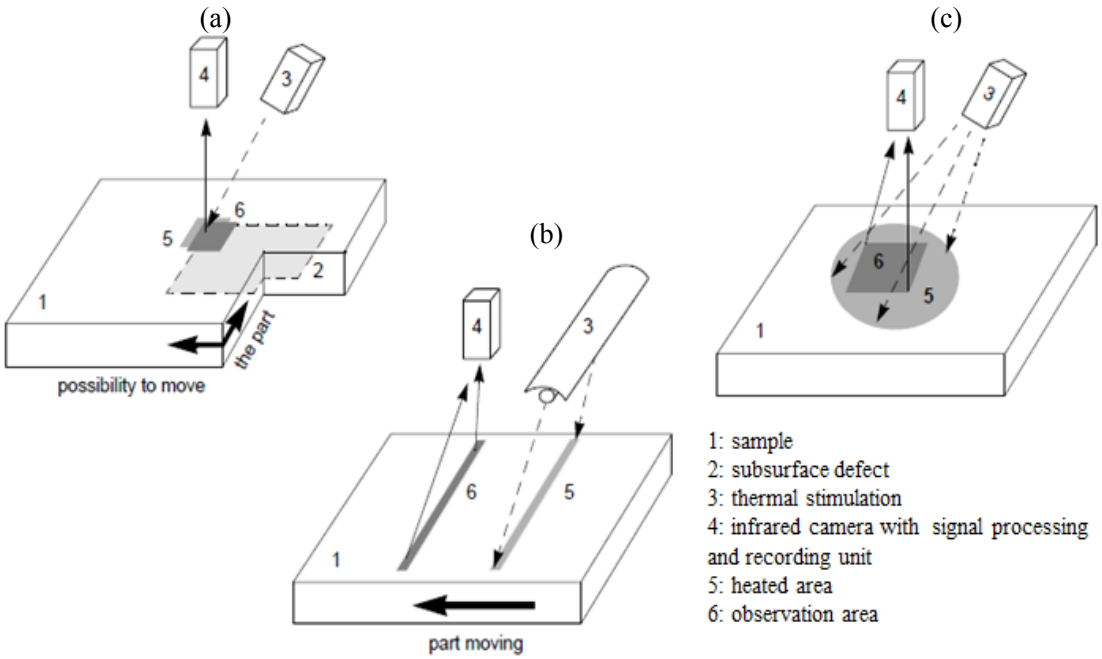

Figure 1.5: Configurations for infrared thermography inspection: (a) by point, (b) by line, (c) by surface [from Maldague, 2002].

This technique is particularly indicated for the analysis of multilayered coatings or composite structures [Maclachlan-Spicer et al., 1991; Vavilov et al., 1997; Osiander et al., 1998; Meola et al., 2005] and for ancient building or mosaic investigations, because the flash excitation could be dangerous [Di Maio et al. 2010, 2012a; Mazioud et al., 2010].

1.3 PT data analysis and interpretation

Although PT is probably the most handled thermographic technique due to its easiness of use, raw PT data are difficult to analyse in a quantitative way, so many processing techniques have been developed to enhance PT data interpretation and also this thesis work is aimed at giving a contribution to this challenging issue.

In the following paragraphs, a brief summary of the most common methods for quantitative analyses of pulse thermography data will be given to provide the state of art on the topic of this thesis.

1.3.1 Thermal contrast technique

The thermal contrast technique is the most used procedure of PT data analysis, as it allows estimating quantitatively the depth of the defects.

The *absolute* thermal contrast is defined as:

$$\Delta T(t) = T_d(t) - T_{S_a}(t)\,, \tag{1.11}$$

where $T(t)$ is the temperature at time t, $T_d(t)$ the temperature of a pixel or the average value of a group of pixels related to a defected area and $T_{Sa}(t)$ the temperature at time t for the sound area S_a (Fig. 1.6).

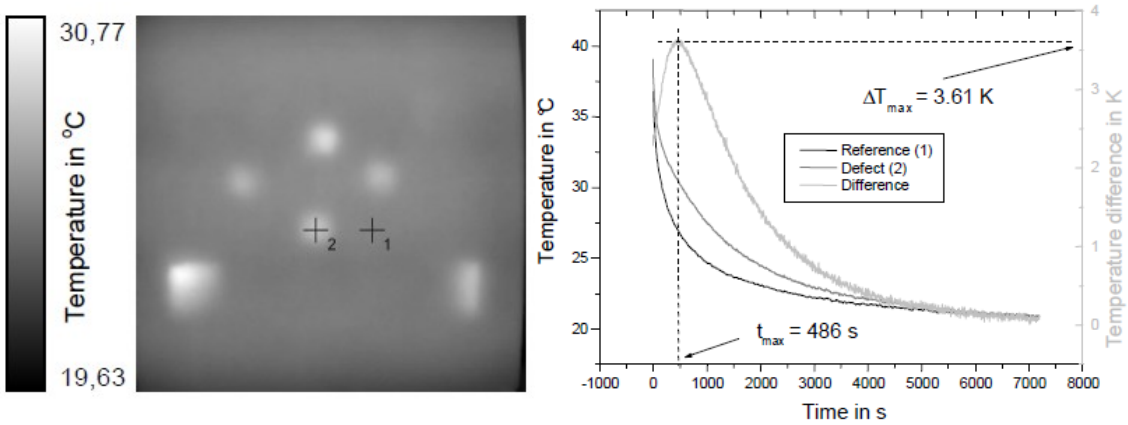

Figure 1.6: Estimation of the thermal contrast. (a) Thermogram showing a defect area (2) and a sound area (1); (b) Temperature versus time curves for the selected areas (defect and sound) and relative difference curve that shows a maximum temperature difference at a distinct time [from Brink et al., 2002].

The main disadvantage of this method is that it is difficult to identify the sound area (different locations of the sound involve significant changes in the thermal contrast profiles), especially when sufficient information about the investigated medium are not available and the results are influenced by the non-uniform heating. In all these cases, the computation of absolute thermal contrast may be inaccurate [Grinzato et al., 2002].

Thus, a new technique, which allows overcoming these difficulties and obtaining a reliable thermal contrast, was developed, i.e. the differential absolute contrast (DAC) method [Pilla et al., 2002]. It requires to compute an ideal S_a temperature locally by assuming that this local point acts as sound zone for the first few images (at least one image at time *t'* in particular). The first step is to define the time *t'* between the instant when the pulse has been sent, t_0, and the time when there is enough contrast for detecting the defect t_1. At *t'*, there is no indication of the existence of a defective zone yet, therefore the local temperature for a S_a is exactly the same as for a defective area, $T_{Sa}(t')=T(t')$ [Pilla et al., 2002].

Assuming a Dirac pulse applied to a semi-infinite body, in first approximation the 1D solution of the Fourier equation gives:

$$\Delta T_{S_a}(t') = \Delta T(t') = \frac{Q}{e\sqrt{\pi t'}} \rightarrow \frac{Q}{e} = \sqrt{\pi t'}\,\Delta T(t')\,, \tag{1.12}$$

where Q [J/m^2] is the energy absorbed by the surface and $e = (\rho k c_p)^{1/2}$ [J/m^{2}ks$^{1/2}$] is the thermal effusivity and ΔT is the temperature increase from t=0.

In this way, from Eq. (1.12) the temperature of the sound area can be defined locally as a function of *t*:

$$\Delta T_{S_a}(t) = \frac{Q}{e\sqrt{\pi t}} = \frac{\sqrt{\pi t'}}{\sqrt{\pi t}}\Delta T(t') = \sqrt{\frac{t'}{t}}\Delta T(t') \quad . \tag{1.13}$$

Finally,

$$\Delta T_{dac}(t) = \Delta T(t) - \sqrt{\frac{t'}{t}}\Delta T(t')\,. \tag{1.14}$$

This technique is very efficient in reducing artifacts from non-uniform heating and surface geometry and it provides a good approximation even for the case of anisotropic materials at early times (Fig. 1.7) [Ibarra-Castanedo et al., 2005].

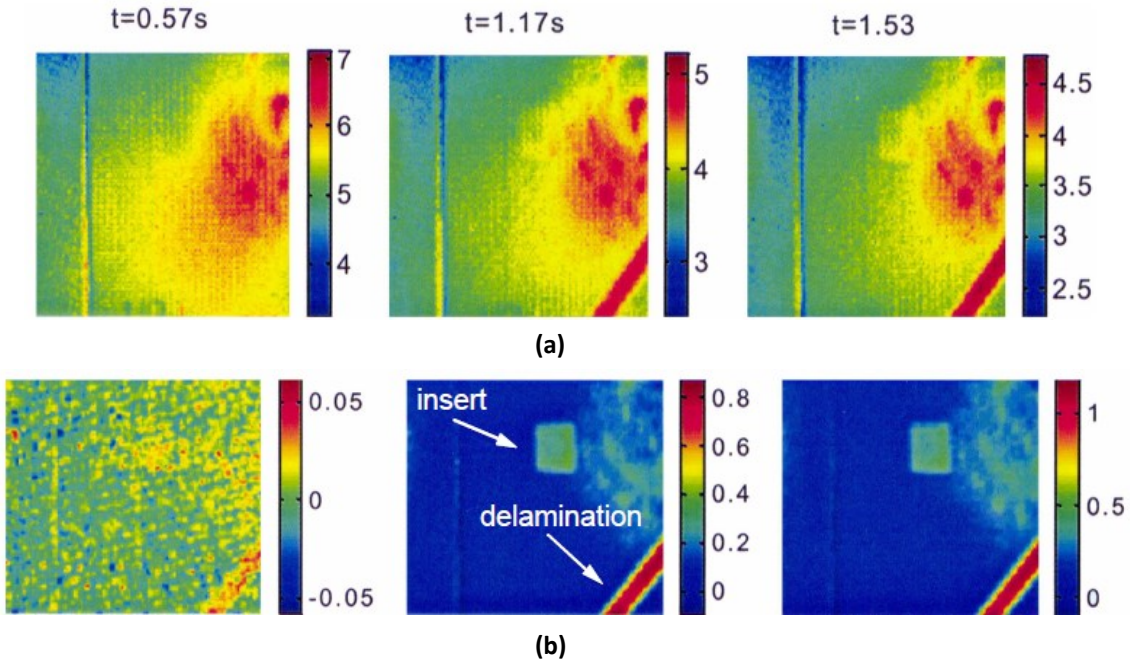

Figure 1.7: (a) Raw thermograms for a graphite-epoxy specimen at t=0.57, 1.17, 1.53 s; (b) new absolute contrast images at the same times [from Pilla et al., 2002].

However, once the thermal contrast was calculated, the depth of the defects can be assessed considering the maximum thermal contrast value (ΔT_{max}) and the respective time (t_{max}):

$$z = A\sqrt{t_{max}}\Delta T_{max}^{h}\,, \tag{1.15}$$

where A and h are parameters obtained from a calibration process [Ibarra-Castanedo et al., 2007b].

The thermal contrast analysis is also used to obtain calibration curves for the determination of defect depth from the experimental data [Brink et al., 2002; Maierhofer et al., 2003]. In practice, a thermographic investigation on a specimen, characterized by defects localized at different depths, is made. The thermal contrast curve versus time is calculated for every defect and the maximum thermal contrast value is considered; then the corresponding time is plotted versus defect depth for different heating time (Fig. 1.8) [Brink et al., 2002]. Maierhofer et al. [2003] validate the results of the thermal contrast

analysis through a qualitative comparison with the results of georadar data analysis. Brink et al. [2002], instead, compare the results of the thermal contrast analysis with those from synthetic models. In this case, by varying the heating time for each defect the nominal depth and the mean depth, as result from inverse solution, are compared. However, the agreement between nominal and predicted depths is not always found; the authors suggest that probably the nominal depth changed during the concreting process [Brink et al., 2002].

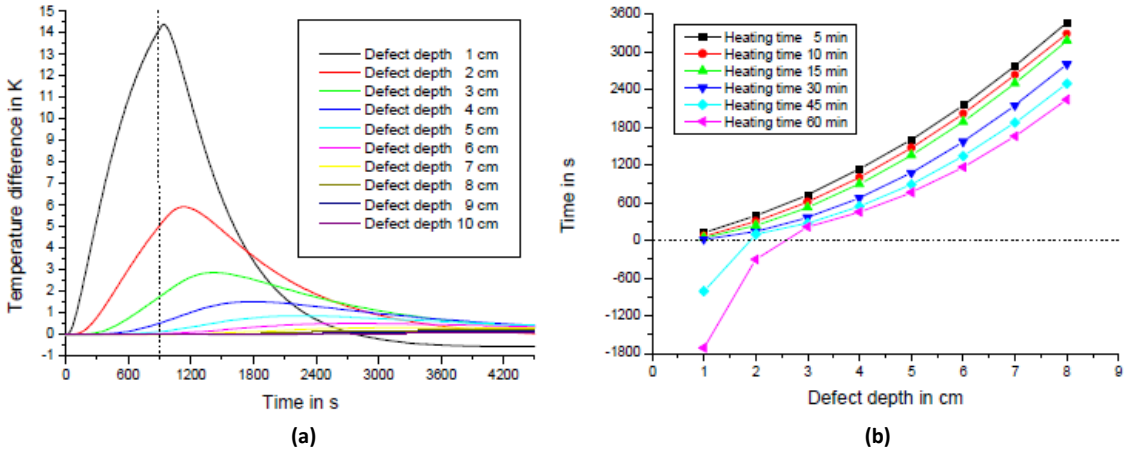

Figure 1.8: (a) Simulated temperature difference curves for different defect depths for 15 min of heating time. (b) Time of maximum temperature difference for various defect depths and heating times [from Brink et al., 2002].

1.3.2 Pulse phase thermography

In pulse phase thermography (PPT), although the specimen is heated as in PT, the acquired data are transformed from the time domain to the frequency spectra domain using the one-dimensional discrete Fourier transform (DFT),

$$F_n = \Delta t \sum_{k=0}^{N-1} T(k\Delta t) e^{-2\pi j n k / N} = \mathrm{Re}_n + \mathrm{Im}_n \,, \qquad (1.16)$$

thus permitting the computation of phase images as in lock-in thermography [Maldague and Marinetti, 1996; Ibarra-Castanedo and Maldague, 2004]. In Eq. (1.16), j is the unit imaginary number, n is the frequency increment ($n=0,1,\ldots,N$), Δt is the sampling interval, Re and Im are the real and the imaginary parts of the transform, respectively, which can be used to calculate the amplitude and the phase of the transform:

$$A_n = \sqrt{Re_n^2 + Im_n^2} \tag{1.17}$$

$$\varphi_n = tan^{-1}\left(\frac{Im_n}{Re_n}\right) . \tag{1.18}$$

Another way to extract amplitude and phase information from PT data is through wavelet transforms (WT) [Galmiche et al., 2000]. In PT, the time information is related to the defect depth, so the advantage of this type of analysis is that, preserving the time information of the signal after the transformation, allows for quantitative evaluations [Ibarra-Castanedo et al., 2007a]. Using the WT, the signal $T(k)$ for a pixel (i, j) is decomposed into stretched and scale replicas of the base wavelet:

$$W_f(S,T) = \int_{-\infty}^{+\infty} f(t) h^*_{ST_r}(t) dt = Re + jIm , \tag{1.19}$$

where W_f denotes the WT, $f(t)$ is the analyzed function and h_{STr} is the daughter wavelet defined from the mother wavelet:

$$h_{ST_r}(t) = \frac{1}{\sqrt{S}} h\left(\frac{t-T}{S}\right) , \tag{1.20}$$

where T_r is the translation factor, related to the time, and S is the scaling factor related to the frequency [Galmiche et al., 2000].

A common used mother wavelet is the Morlet wavelet, defined as:

$$h(t) = e^{j\omega_0 t} e^{-t^2/2} , \tag{1.21}$$

where ω_0 provides the size of the Morlet wavelet. From Eq. (1.19), the real and imaginary parts become available and then it is possible to compute phase and amplitude images.

However, whether DFT or WT are used, the phase φ is less affected than raw thermal data by environmental reflections, emissivity variations, non-uniform heating, surface geometry and orientation [Ibarra-Castanedo, 2006]. These phase characteristics are very important not only for qualitative inspections, but also for quantitative characterization of materials. More in detail, experimental evidences show that a linear relationship exists between defect depth z and the inverse square root of the *blind* frequency f_b, i.e. the frequency at which a defect, located at a given depth, presents enough phase contrast to be detected [Bai and Wong, 2001; Ibarra-Castanedo et al., 2007b; Rodriguez et al., 2011]. The thermal diffusion length μ, expressed by Eq. (1.7), can be used to fit experimental data [Ibarra-Castanedo, 2007b]:

$$z = C_1 \sqrt{\frac{\alpha}{\pi f_b}} = C_1 \mu \,, \tag{1.22}$$

where C_1 is an empirical constant and f_b [Hz] is the blind frequency.

It has been observed that C_1=1 for amplitude images, so the depth range is given by the thermal diffusion equation $z \sim \mu$, whilst for phase images $1.5<C_1<2$, so $1.5\mu<z<2\mu$ [Ibarra-Castanedo, 2006; Ibarra-Castanedo et al., 2007b]. In this way, the inversion problem is reduced to the estimation of f_b from the phase, i.e. to the estimation of the phase contrast defined as [Bai and Wong, 2001]:

$$\Delta\varphi = \varphi_d - \varphi_{S_a} \,, \tag{1.23}$$

where φ_d and φ_{Sa} are the phase of a defect area and a reference sound area, respectively. For these reasons, although amplitude images are sometimes of interest, the use of phase is more appealing in Nondestructive Testing and Evaluation (NDT&E) especially for quantitative evaluation of materials, since contrast changes between the defects and the sound area can be more clearly observed compared with those in conventional thermal images (Fig. 1.9).

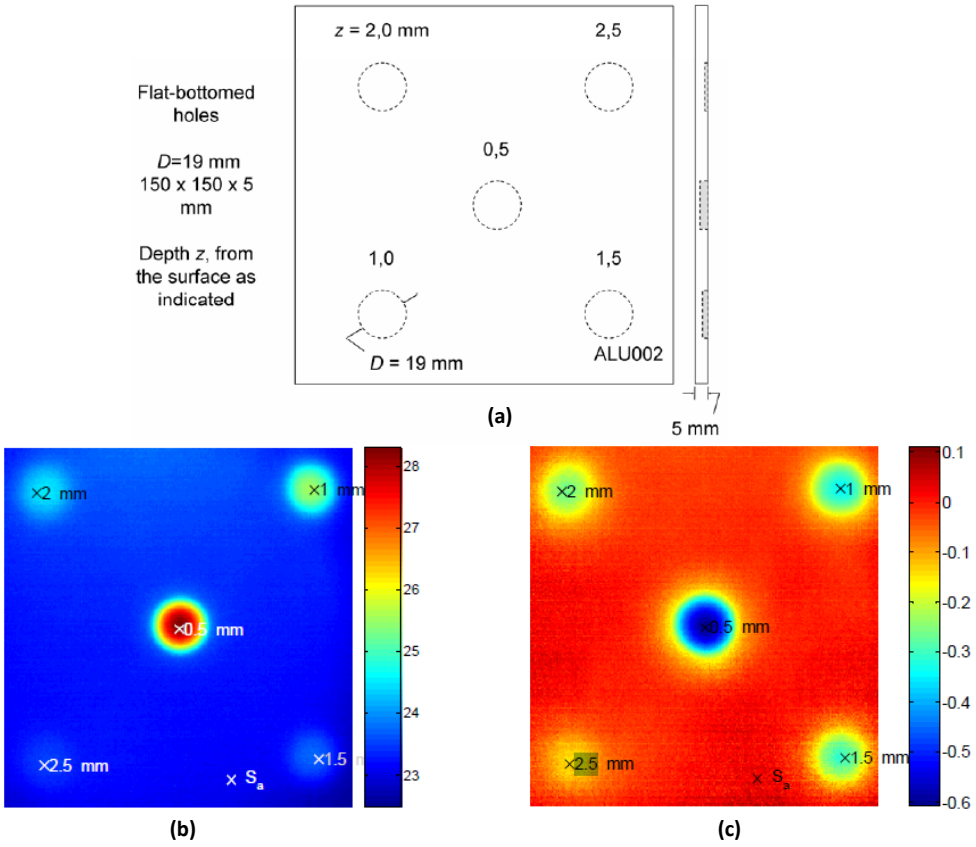

Figure 1.9: (a) Specimen: aluminum plate with 5 flat-bottomed holes. (b) Thermogram at t=25 ms showing defect locations. I Phasegram at f=0.47 Hz [modified from Ibarra-Castanedo, 2006].

1.3.3 Thermographic signal reconstruction

Thermographic Signal Reconstruction (TSR) is a technique developed by Shepard (2001). It is based on the assumption that temperature profiles for sound areas follow decay curves given by the one-dimensional solution of the Fourier Equation, i.e. Eq. (1.5), which may be rewritten in logarithmic form as:

$$\ln(\Delta T) = \ln\left(\frac{Q}{e}\right) - \frac{1}{2}\ln(\pi t)\ . \qquad (1.24)$$

Shepard (2001) proposed to fit the temperature decay curve for each pixel by a n-degree polynomial:

$$\ln(\Delta T) = a_0 + a_1\ln(t) + a_2\ln^2(t) + \cdots + a_p\ln^n(t). \qquad (1.25)$$

Typically, n is set equals to 4 or 5 to insure a good correspondence between experimental data and the fitted values, and to reduce noise content in the signal [Ibarra-Castanedo, 2006; Ibarra-Castanedo et al., 2007b].

In this way, synthetic data for a 5th degree polynomial can be, for example, obtained from [Shepard, 2001]:

$$\Delta T = exp[a_0 + a_1 \ln(t) + a_2 \ln^2(t) + a_3 \ln^3(t) + a_4 \ln^4(t) + a_5 \ln^5(t) \; . \quad (1.26)$$

The advantages of this procedure are the considerably reduction on data to process, the possibility to work with analytical solutions and the significant noise reduction as is shown in Fig. 1.10.

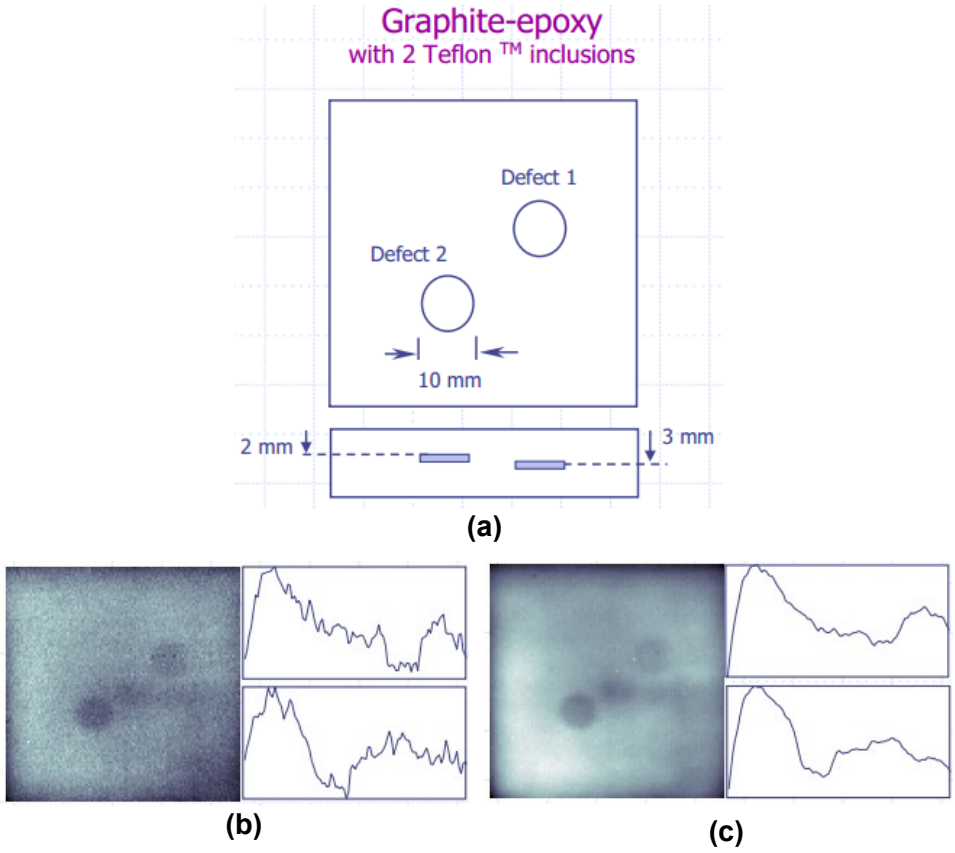

Figure 1.10: (a) Graphite-epoxy plate 4 mm thick with 2 artificial Teflon inclusions, 2 (top) and 3 (bottom) mm depth; (b) PPT, *f*=0.33 Hz and (c) synthetic PPT, *f*=0.33 Hz [modified from Ibarra-Castanedo et al., 2003].

1.3.4 Artificial Neural network

Artificial neural networks (ANN) are computational models inspired by biological neuron activity. An artificial neuron (Fig. 1.11), which is the constitutive unit of an artificial neural network, receives one or more inputs and sums them to produce an output. Usually the sums of each node are weighted, and the sum is passed through a non-linear function known as an *activation function* or *transfer function*. The combination of artificial neurons for information processing represents the artificial neural network.

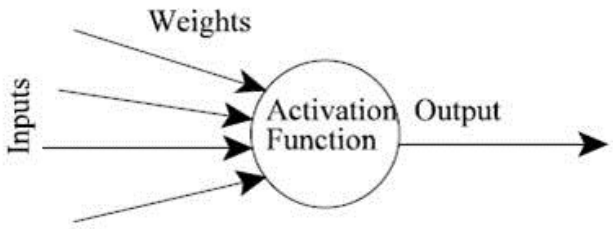

Figure 1.11: An artificial neuron.

An artificial neural network can be trained using mathematical modelling data to provide an accurate means of parameterizing defects imaged by transient thermography. In particular, through a finite element modelling the input parameters of the neural networks are determined. Some authors use as input parameter the maximum temperature of the defect, the temperature of the sound zone and the average temperature of the medium [Heriansyah and Abu-Bakar, 2007], other authors instead use the time at which the image contrast reaches half its maximum value, the time at which the image contrast falls to half its maximum value, the full width at half maximum (FWHM) at half rise time, the FWHM at half fall time, the maximum relative contrast attained by the image (Fig. 1.12) [Saintey and Almond, 1997].

However, in every case the trained neural network acts as an experimental data interpreter, which takes account of the full complexity of defect image variation

obtained by a range of finite difference modelling simulations [Manduchi et al., 1997; Saintey and Almond, 1997; Heriansyah and Abu-Bakar, 2007].

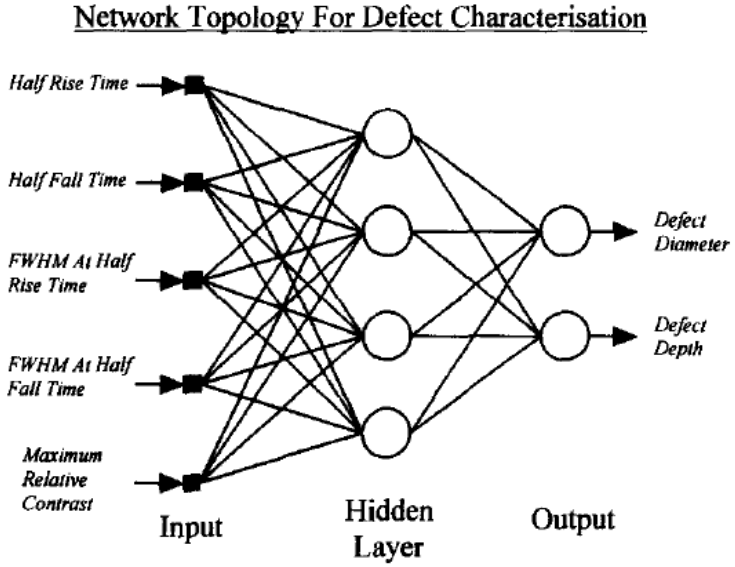

Figure 1.12: Artificial neural network used for defect characterization.

1.3.5 Inverse methods

Analytical inversion algorithms were developed to characterize thermal anomalies through transient thermographic imaging under 1D thermal flow conditions [Krapez and Cielo, 1991; Delpech et al., 1994]. In this approach, an iterative procedure based on the least squares method is used to minimize the deviation between experimental thermal transient data and the corresponding computed analytical transient calculated by the Green's functions. In order to solve the problem analytically for inhomogeneous media, boundary conditions have to be fixed; anyway the problem can be solved only for simple cases, i.e. a double-layer sheet with a defect situated at the interface between the two layers [Krapez and Cielo, 1991].

Due to the limits of the 1D assumption, numerical Finite Difference models were developed to study two-dimensional thermal flows [Krapez et al., 1991; Brink et al., 2002; Maierhofer et al., 2005]. Concurrently, numerical models based on the Finite

Element method were also developed for modelling complex structure specimens. Some authors highlighted the importance of a non-uniform heating, which represents one of the main problems for the comparison of experimental and numerical results, and for identifying the defect characteristics [Susa et al., 2007]. Other authors studied extensively initial and boundary conditions to evaluate all input parameters and functions required for the application of numerical modelling at landmine detection, in which the sun is the heating source and it is important to evaluate the influence of weather and soil conditions [Lopez et al., 2003; Thành, 2007].

More recently, a semi-analytic reformulation of the heat transport problem has been proposed for a quantitative detection of defects in test specimens [Weiser et al., 2010]. In this case, the authors capture the boundary layer with an analytically obtained approximation, and compute only numerically the remaining defect in order to increase reliability for quantitative prediction and simultaneously to decrease computational costs.

In the next sections, an algorithm based on conservative finite difference method is presented for the simulation of the thermal response of inhomogeneous materials for both 1D and 2D approximation. The numerical codes are first tested on IRT data acquired on two masonry laboratory specimens, and then applied to in-situ data coming from testing in architectural and environmental field. A non-iterative inversion method based on the Prony's theorem is also proposed and discussed.

Chapter II

Numerical codes for solving the Heat Equation

In this chapter, numerical codes developed to solve heat transfer problems in inhomogeneous media will be illustrated. The codes are implemented in MATLAB environment and provide approximated numerical solutions for the one-dimensional (1D) and two-dimensional (2D) cases. Since they are based on the Finite Difference approximations, some details about this method will be given before illustrating the algorithms.

2.1 Heat Equation

In presence of a temperature gradient in a medium or when two systems at different temperatures are in contact, exchange of energy starts in the form of heat transmission, which can occur in three ways: conduction, radiation and convection.

It is worth noting that in the most natural phenomena the propagation of heat occurs according multiple mechanisms simultaneously; thus to estimate previously what mechanism prevails, it is very important to obtain useful approximations for the solution of complex problems.

In particular, in the present work conduction phenomena will be only considered, while the contribution of convection and irradiation mechanisms, which are predominant in presence of fluids and high temperatures (i.e. temperatures much larger than atmospheric temperature) respectively, will be neglected.

Heat conduction is the flow of internal energy by the interaction of the adjacent particles (atoms, molecules, ions, electrons, etc.) in the intervening space due to a temperature gradient. The fundamental relationship of heat transfer by conduction has been proposed by Fourier [1822]. The Fourier's law states that the rate of flow of heat energy through a surface is proportional to the negative temperature gradient across the surface:

$$\vec{q} = -k \cdot \nabla T \ , \tag{2.1}$$

where k is the thermal conductivity and T is the temperature.

A body of volume V to which is provided an energy Q is considered. In the absence of work done on the system, a change in internal energy of the material, dQ, is proportional to the change in temperature, dT:

$$dQ = c_p dm dT \ , \tag{2.2}$$

where c_p [J/kgK] is the specific heat at constant pressure, $dm=\rho dV$ [kg] is the infinitesimal mass of the volume dV [m^3] with density ρ [kg/m^3] and dT [K] is the temperature variation.

Differentiating with respect to time, Eq. (2.2) reads:

$$dQ = c_p \rho dV \frac{\partial T}{\partial t} dt \ . \tag{2.3}$$

The thermal power across the surface dS in time is:

$$dP_q = k dS dt \frac{\partial T}{\partial n} = k dS dt \nabla T n \ , \tag{2.4}$$

where $\partial T/\partial n$ is the gradient of the temperature in the section, i.e. the variation of the temperature T with respect to the distance in the direction of flow, n.

Integrating on the surface of the volume *V*:

$$P_q = \iint kdt\nabla T n dS = \iiint kdt\nabla^2 T dV \tag{2.5}$$

and then, by conservation of energy,:

$$\iiint kdt\nabla^2 T dV = \iiint c_p \rho dt \frac{\partial T}{\partial t} dV \;\; \rightarrow \iiint (c_p \rho \frac{\partial T}{\partial t} - k\nabla^2 T) dV = 0 \tag{2.6}$$

This equation is valid for every volume, so the integral can be removed and then the heat equation becomes:

$$c_p \rho \frac{\partial T}{\partial t} = k\nabla^2 T \quad . \tag{2.7}$$

Introducing the thermal diffusivity $\alpha = k/\rho c_p$ [m^2/s], the above equation can be written as:

$$\frac{\partial T}{\partial t} = \alpha \nabla^2 T \tag{2.8}$$

The solution of such a partial differential equation provides the theoretical temperature decay of the homogeneous medium under investigation.

In most practical cases, analyses of thermal responses of non-homogeneous structures are required to assess the state of conservation of architectural structures of civil use or archaeological interest. To this aim, since analytical solutions of Eq. (2.8) with $\alpha = \alpha(x,y,z)$ are not possible, several methods for semi-analytical or numerical approximated solutions are developed.

In the next section, the heat equation is solved through the Finite Difference method in order to provide approximated numerical solutions in inhomogeneous media for both 1D and 2D cases.

2.2 Finite Difference approximation to the Heat Equation

The heat equation can be solved by either numerical or analytical methods. Analytical methods involve the solution of partial differential equations (PDE) using calculus based

on the initial and boundary value conditions. The advantages of an analytical solution are that it usually provides an exact solution to the governing equation and is often relatively simple and efficient to obtain. However, analytical methods are limited to simple geometry and require the medium to be homogeneous. Alternatively, for problems where the simplified analytical models are inadequate, the PDE can be approximated numerically. Numerical methods are more powerful than analytical solutions in the sense that any geometry of the medium can be analyzed and heterogeneous structures can be also investigated.

Two major classes of numerical methods are commonly used for solving the heat equation and, in general, for solving PDE. These are the finite-difference (FD) methods and the finite-element (FE) methods. Both of these numerical approaches require that the area (or volume) of interest be subdivided by a grid into a number of smaller subareas (cells or elements) that are associated with node points (either at the centres or peripheries of the subareas).

FD methods approximate the first derivatives in the partial differential equations as difference quotients (the differences between values of variables at adjacent nodes, both in space and time, with respect to the interval between those adjacent nodes). There are several advanced text books that focus primarily on finite-difference methods [Patankar, 1980; Fletcher, 1988; Ames, 1991; Morton and Mayers, 1994]. FE methods use assumed functions of the dependent variables and parameters to evaluate equivalent integral formulations of the partial differential equations. In both numerical approaches, the discretisation of the space and time dimensions allows the continuous boundary-value problem for the solution of the PDE to be reduced to the simultaneous solution of a set of algebraic equations. These equations can then be solved using either iterative or direct matrix methods.

In general, the FD methods are simpler conceptually and mathematically, and are easier to program for a computer. They typically use relatively simple, rectangular grids, which also make easier data entry tasks. For these reasons, in order to simulate the thermal response of inhomogeneous media and multi-layered structures, in this thesis work numerical codes based on FD methods are developed.

2.2.1 The discrete mesh

The mesh is the grid of points (nodes) where the discrete solution of the PDE equation is computed. The key parameters of the mesh are the local distance between adjacent points in space, Δr, and the local distance between adjacent time steps, Δt [Recktenwald, 2004].

For the codes developed in this work, the discrete time steps Δt are uniformly spaced and depend on the regular time interval at which thermal images are acquired. Thus, the time interval between adjacent time steps can be written as:

$$\Delta t = \frac{t_0 - t_f}{n_t - 1} \ , \tag{2.9}$$

where t_0 and t_f are, respectively, the start and the final time [s] of the cooling (or heating) phase process and n_t is the total number of time steps or, equivalently, of thermal images.

As regards the space discretization, for 1D modeling, the vertical distance z is discretized by subdividing the medium into $n=N-1$ layers with thickness Δz_i, where N is the number of basic nodes in z-direction (see below). For 2D modelling, variations in depth direction z and in lateral direction x have to be considered and, therefore, the total number of basic nodes is given by $N \times M$, where N is the number of basic nodes in z-direction and M is the number of basic nodes in x direction. In Fig. 2.1, two examples of grids are shown, respectively, with $N=4$ for 1D modelling and with $N=4$ and $M=3$ for 2D modelling.

As shown in Fig. 2.1, staggered grids are required to discretize the heat equation [Eq. (2.8)] in the case of variable thermal conductivity. In a staggered grid, basic nodes (squares) are distinguished by additional nodes (circles). In particular, in basic nodes density, specific heat and heat equation are defined, whereas in additional nodes thermal conductivity and heat fluxes are defined [Gerya, 2010]. The additional nodes are positioned at the centre of each layer, as shown in Fig. 2.1. Discretization by means of staggered grids is also named Conservative Finite Difference discretization, since it allows for conservation of heat fluxes between nodal points.

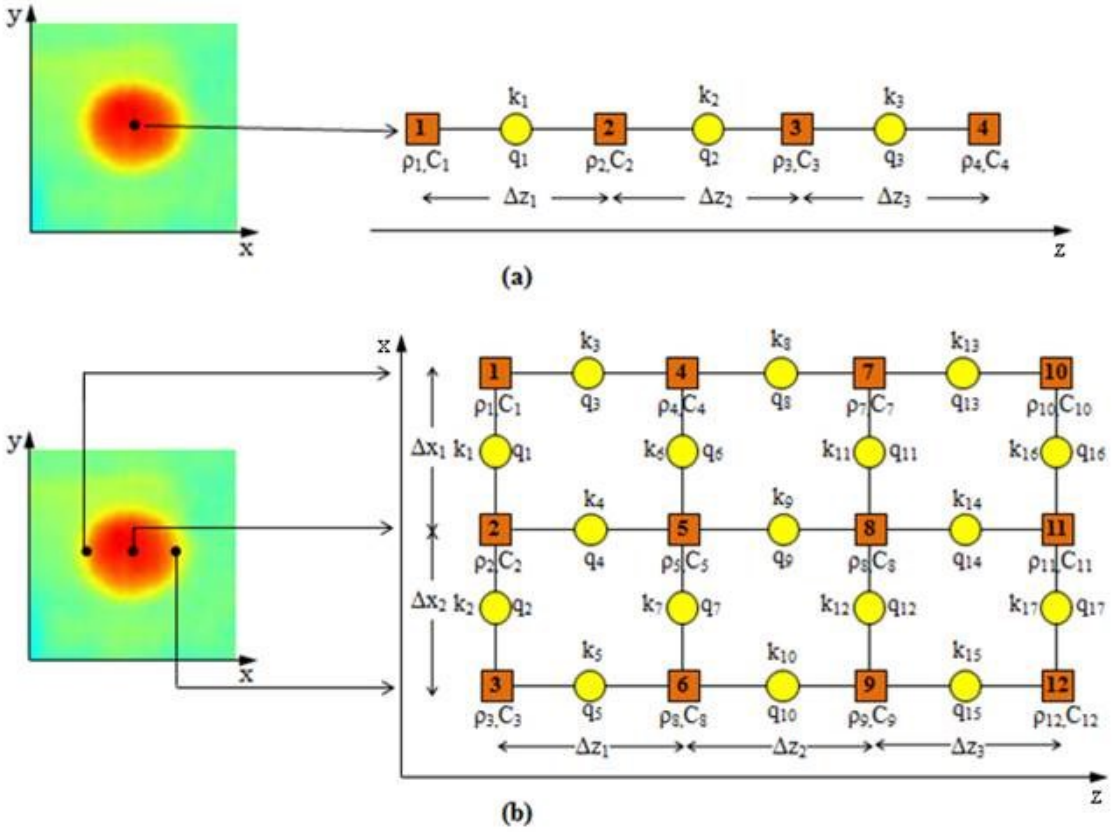

Figure 2.1: 1D (a) and 2D (b) staggered grids for in-depth modelling of temperature pixels indicated with black points on the thermograms. The orange squares are the basic nodes and the yellow circles are the additional nodes of the grid.

2.2.2 1D Approximation

Once the grid is fixed, the heat equation (2.8), which includes terms representing derivatives of the continuous variable *T*, can be discretized through FD method. FD discretization is based on the approximation of the derivatives by discrete linear changes over small discrete intervals of space or time. If the intervals are sufficiently small, then all of the linear increments will represent a good approximation of the true curvilinear surface. For the 1D case, the approximation for the second derivative $\frac{\partial^2 T}{\partial z^2}$ reads:

$$\frac{\partial^2 T}{\partial z^2} \approx \left(\frac{T_{i-1}^n - 2T_i^n + T_{i+1}^n}{\Delta z^2}\right) \quad , \tag{2.10}$$

where i is the spatial node index, n is the temporal node index, T_i^n is the temperature of the node i at time instant t_n (Fig. 2.2).

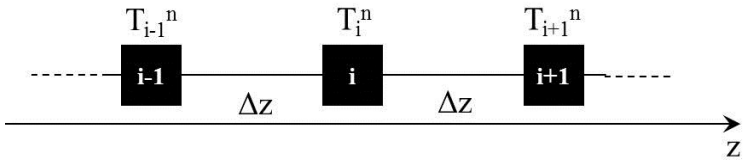

Figure 2.2: Stencil of the 1D grid used for the FD discretization of the heat equation with constant thermal conductivity.

When the time discretization is considered, two choices are possible for the approximated time derivative:

$$\frac{\partial T}{\partial t} \approx \left(\frac{T_i^{n+1} - T_i^n}{\Delta t}\right) \quad \text{or} \quad \frac{\partial T}{\partial t} \approx \left(\frac{T_i^n - T_i^{n-1}}{\Delta t}\right) , \tag{2.11}$$

which are named forward difference and backward difference, respectively.
If the forward difference is used, the heat equation reads:

$$\frac{T_i^{n+1} - T_i^n}{\Delta t} = \frac{k}{\rho \cdot c_p}\left(\frac{T_{i-1}^n - 2T_i^n + T_{i+1}^n}{\Delta z^2}\right) . \tag{2.12}$$

For every node of the grid i, by solving Eq. (2.12), a separate difference equation is obtained, which contains only one unknown variable that is the unknown temperature at the time step $n+1$:

$$T_i^{n+1} = T_i^n + \frac{k \cdot \Delta t}{\rho \cdot c_p \cdot \Delta z^2}\left(T_{i-1}^n - 2T_i^n + T_{i+1}^n\right) . \tag{2.13}$$

These equations refers to *Forward Time, Centered Space* (BTCS) scheme in which the temperature T_i^{n+1} at spatial node z and time instant $n+1$ is defined through the temperature at previous time instant n and at previous ($i-1$) and following ($i+1$) spatial node. Eq. (2.13) can be solved explicitly because all the terms in the second member are

known [Recktenwald, 2004]. The explicit formulation does not require solving a system of equations and is therefore very convenient to program. However, this formulation may have stability problems: if time increments are too large, small numerical errors or perturbations may propagate into larger errors at later stages of the computations. Thus, a strong limitation on the time step is usually required:

$$\Delta t < \frac{\Delta z^2}{3\alpha} \tag{2.14}$$

where $\alpha=k/\rho c_p$ is the thermal diffusivity and Δz is the minimum grid spacing. This requirement can be quite inconvenient for high-resolution thermal models as the greater is the grid spacing and the greater is the time step [Gerya, 2010].

If the time derivative is expressed as a backward difference from the temperatures at time step n, the heat equation reads:

$$\frac{T_i^n - T_i^{n-1}}{\Delta t} = \frac{k}{\rho \cdot c_p}\left(\frac{T_{i-1}^n - 2T_i^n + T_{i+1}^n}{\Delta z^2}\right) \quad . \tag{2.15}$$

This form is called implicit because the temperature (T_i^n) for the time instant t_n cannot be explicitly calculated from the temperatures (T^{n-1}) known from the previous time instant t_{n-1}, since the spatial derivatives of the temperatures are written at time step n, where all values are unknown. For every node of the grid, we have:

$$\frac{T_i^n}{\Delta t} - \frac{k}{\rho \cdot c_p}\left(\frac{T_{i-1}^n - 2T_i^n + T_{i+1}^n}{\Delta z^2}\right) = \frac{T_i^{n-1}}{\Delta t} \quad . \tag{2.16}$$

Thus, for the entire grid, which contains N nodes, a system of N equations containing a total of N unknowns is obtained. Such a system of simultaneous equations, together with specified boundary conditions, can be solved implicitly. Although implicit solutions are more complicated, they have the advantage of generally being unconditionally stable, therefore, in this thesis implicit formulation will be used in the implemented numerical codes.

Finally, it is important to note that the implicit formulation places no limitation on the size of the time step (in the absence of internal heat sources and advective terms), though very large time steps do not necessarily guarantee an accurate solution [Gerya, 2010].

In case the heat equation contains a variable thermal conductivity, as it will be considered in the next chapters, Conservative Finite Difference discretization is required. Such a kind of discretization (either explicit or implicit) is based on the following three steps [Gerya, 2010]. First, the temperature equation is discretized in terms of heat fluxes (q) at basic nodes of the grid (see Fig. 2.1):

$$\rho_i c_{p_i} \frac{T_i^n - T_i^{n-1}}{\Delta t} = \frac{q_l - q_{l-1}}{(\Delta z_{l-1} + \Delta z_l)/2} \ , \tag{2.17}$$

where i is the spatial basic node index and l is the spatial additional node index.

The heat fluxes are, then, formulated for additional nodes of the grid:

$$q_l = -k_l \frac{T_{i+1} - T_i}{\Delta z_l} \ . \tag{2.18}$$

If the values of thermal conductivity k_l are unknown, they can be calculated by arithmetic or harmonic averaging of known thermal conductivity values at basic nodes.

Finally, identical formulations of heat fluxes are used for the temperature equation at different basic nodes.

It is worth noticing that in the case of inhomogeneous media, Δz is not a constant, but depends on position and size of inhomogeneities in the medium. Thus, in the following, the conservative FD implicit formulation will be used with non-regular staggered grid.

2.2.3 2D Approximation

For a 2D modelling, i.e. if the in-depth and the lateral direction are considered, the implicit Finite Difference discretization becomes:

$$\frac{T_{i,j}^{n}-T_{i,j}^{n-1}}{\Delta t}=\frac{k}{\rho\cdot c_p}\left(\frac{T_{i-1,j}^{n}-2T_{i,j}^{n}+T_{i+1,j}^{n}}{\Delta x^2}+\frac{T_{i,j-1}^{n}-2T_{i,j}^{n}+T_{i,j+1}^{n}}{\Delta z^2}\right) \quad , \qquad (2.19)$$

where i and j are the spatial nodes for the depth direction x and the lateral direction z, respectively, and $T_{i,j}^{n}$ is the temperature of the node (i, j) at time instant t_n (Fig. 2.3).

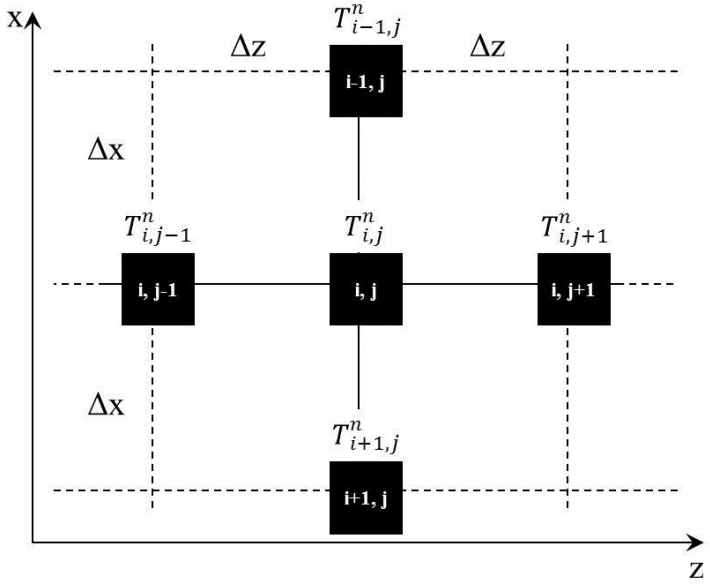

Figure 2.3: Stencil of the 2D grid used for the FD discretization of the heat equation with constant thermal conductivity.

Also in this case, for inhomogeneous media, Conservative FD discretization should be used and the temperature equation at the basic nodes reads:

$$\rho_{i,j}c_{p_{i,j}}\frac{T_{i,j}^{n}-T_{i,j}^{n-1}}{\Delta t}=\frac{q_l-q_{l-1}}{(\Delta z_{j-1}+\Delta z_j)/2}+\frac{q_m-q_{m-1}}{(\Delta x_{i-1}+\Delta x_i)/2} \quad , \qquad (2.20)$$

where l and m are the spatial additional nodes index for the depth direction z and the lateral direction x, respectively (Fig.2.3), and the heat fluxes for the additional nodes of the grid are:

$$q_l=-k_l\frac{T_{i,j+1}-T_{i,j}}{\Delta z_j};\ q_m=-k_m\frac{T_{i+1,j}-T_{i,j}}{\Delta x_i} \quad . \qquad (2.21)$$

2.2.4 Thermal boundary conditions

In order to solve the temperature equation numerically, boundary conditions have to be specified. It is possible to impose different boundary conditions depending on the type of numerical problem; the most commonly used are the following:

- *Constant temperature condition*: a given temperature value is assigned at a boundary (such a value may change both along the boundary and in time), i.e.:

$$T = const(z,t) \ . \tag{2.22}$$

  This condition is typically applied at the lower and upper boundaries of the model.

- *Insulating boundary condition*: heat does not flow through a boundary, which implies [from Eq. (2.1)] that no temperature gradient exists across this boundary, i.e.:

$$q_z = -k\frac{\partial T}{\partial z} = \frac{\partial T}{\partial z} = 0 \ . \tag{2.23}$$

- *Constant heat flux condition*: the heat flux across the boundary can be time and coordinate dependent:

$$q_z = -k\frac{\partial T}{\partial Z} = const(z,t) \ . \tag{2.24}$$

- *Infinity-like conditions*: there is not a thermal boundary or this boundary is located very far away. For example, the external constant temperature condition implies that: *i)* the condition (2.16) is satisfied at a parallel boundary located at the distance ΔL from the actual boundary of the model, and *ii)* the temperature gradient between these two boundaries is constant:

$$\frac{\partial T}{\partial z} = \frac{T - T_{external}}{\Delta L} \ . \tag{2.25}$$

In the numerical simulations illustrated in the next chapters, the constant temperature condition will be used only for the bottom of the samples, in the attempt to reproduce the decay response of PT investigations starting from a non-equilibrium thermal state.

2.3 Numerical implementation

The numerical codes developed in this thesis work are aimed at solving the heat equation through the Conservative Finite Difference method, both in the 1D and 2D cases, in order to model inhomogeneous media and/or multi-layered structures.
In this section a description of the algorithms, which are implemented in MATLAB environment, is given.

2.3.1 1D code

In the 1D case, the physical thermal properties vary only along the depth direction, *z*. Consequently, the medium can be studied considering a straight line passing through a point that goes from the medium surface down to its bottom.

After the application of implicit conservative FD formulation, a system of equations for all basic nodes of the model has to be solved. In matrix form, it is expressed as:

$$\begin{bmatrix} b_1 & c_1 & 0 & 0 & 0 & 0 \\ a_2 & b_2 & c_2 & 0 & 0 & 0 \\ 0 & a_3 & b_3 & c_3 & 0 & 0 \\ 0 & 0 & \ddots & \ddots & \ddots & 0 \\ 0 & 0 & 0 & a_{N-1} & b_{N-1} & c_{N-1} \\ 0 & 0 & 0 & 0 & a_N & b_N \end{bmatrix} \begin{bmatrix} T_1^n \\ T_2^n \\ T_3^n \\ \vdots \\ T_{N-1}^n \\ T_N^n \end{bmatrix} = \begin{bmatrix} d_1 \\ d_2 \\ d_3 \\ \vdots \\ d_{N-1} \\ d_N \end{bmatrix} , \tag{2.26}$$

where the coefficients of the internal nodes *i* (*i*=2,....,N-1) are:

$$a_i = -\frac{2k_{i-1}}{\Delta z_{i-1}(\Delta z_{i-1}+\Delta z_i)} \tag{2.27}$$

$$b_i = \frac{\rho_i c_{p_i}}{\Delta t} + \frac{2k_i}{\Delta z_i(\Delta z_{i-1}+\Delta z_i)} + \frac{2k_{i-1}}{\Delta z_{i-1}(\Delta z_{i-1}+\Delta z_i)} \tag{2.28}$$

$$c_i = -\frac{2k_i}{\Delta z_i(\Delta z_{i-1}+\Delta z_i)} \tag{2.29}$$

$$d_i = T_i^{n-1}\frac{\rho_i c_{p_i}}{\Delta t} \quad , \tag{2.30}$$

whereas for the external nodes, i.e. the surface nodes and the bottom nodes of the model, the coefficients are expressed as:

$$a_1 = 0;\ b_1 = \frac{\rho_1 c_{p_1}}{\Delta t} + \frac{k_1}{\Delta z_1^2};\ c_1 = -\frac{k_1}{\Delta z_1^2};\ d_1 = T_1^{n-1}\frac{\rho_1 c_{p_1}}{\Delta t} \quad (2.31)$$

$$a_N = 0;\ b_N = 1;\ c_N = 0;\ d_N = T_{env} \quad . \quad (2.32)$$

Thus, the coefficients on the upper diagonal depend on the parameters of the underlying layer, instead the coefficients on the lower diagonal depend on the parameters of the overlying layer.

The previous mathematical steps were implemented in a MATLAB code that requires in input the number of nodes, the in-depth sampling steps, the time step, the physical properties (i.e. thermal conductivity, density and specific heat) of the medium for every node and the initial temperatures of the internal nodes.

As concerns the boundary conditions, constant temperature conditions are applied at the first and the last nodes of the grid, while initial temperature values of internal nodes are variable. In detail, the temperature of the last node is set equal to the environmental temperature, since in our cases thermal equilibrium of the specimens during the heating phase was not reached. The initial temperature of the first node is set equal to the maximum temperature value of the heating phase, since thermal decays are analyzed and the heating turn-off time coincides with the cooling start time. For the internal nodes, the initial temperatures usually vary in the range between the initial temperatures of the first node and the last node, and they are varied until the best matching between experimental and numerical curve is reached. It is worth noting that initial internal temperatures less than the environmental temperature are possible depending on the thickness of the structure, the materials and/or defects thermal properties and the room temperature.

Once the input parameters and the boundary conditions are defined, the algorithm calculates the matrix coefficients in order to solve the system of equations (2.26) at each time step *i* using LU factorization with backward substitution (see appendix A.1).

2.3.2 2D code

For the 2D case, the thermal properties vary in two directions and the tridiagonal matrix in Eq. (2.23) is replaced with a square matrix (N×M)(N×M) with only six nonzero diagonals, whose matrix coefficients are defined by the heat equations formulated at the basic nodes:

$$\begin{bmatrix} b_{1,1} & c_{1,1} & 0 & e_{1,1} & 0 & 0 \\ a_{1,2} & b_{2,2} & c_{1,2} & 0 & \ddots & 0 \\ 0 & a_{1,3} & b_{3,3} & c_{1,3} & 0 & e_{M,N-1} \\ d_{1,2} & 0 & \ddots & \ddots & \ddots & 0 \\ 0 & \ddots & 0 & \ddots & \ddots & c_{M-1,N} \\ 0 & 0 & d_{M,N} & 0 & a_{M,N} & b_{M,N} \end{bmatrix} \begin{bmatrix} T_{1,1}^n \\ T_{1,2}^n \\ T_{1,3}^n \\ \vdots \\ T_{NM-1,,N}^n \\ T_{NM,N}^n \end{bmatrix} = \begin{bmatrix} f_{1,1} \\ f_{1,2} \\ f_{1,3} \\ \vdots \\ f_{NM-1,N} \\ f_{NM,N} \end{bmatrix}, \quad (2.33)$$

where the coefficients of the internal nodes are:

$$a_{i,j} = -\frac{2k_{(i-1)+\mu(j)}}{\Delta x_{i-1}(\Delta x_{i-1}+\Delta x_i)} \quad i=2,\ldots, M; j=1,\ldots, N \quad (2.34)$$

$$b_{i,j} = \frac{\rho_{i,j}c_{p_{i,j}}}{\Delta t} + \frac{2k_{(i-1)+M+\nu(j)}}{\Delta z_{j-1}(\Delta z_{j-1}+\Delta z_j)} + \frac{2k_{(i-2)+3M+\nu(j)}}{\Delta z_j(\Delta z_{j-1}+\Delta z_j)} + \frac{2k_{(i-1)+\mu(j)}}{\Delta x_{i-1}(\Delta x_{i-1}+\Delta x_i)} + \\ + \frac{2k_{i+\mu(j)}}{\Delta x_i(\Delta x_{i-1}+\Delta x_i)} \quad (2.35)$$

$$c_{i,j} = -\frac{2k_{i+\mu(j)}}{\Delta x_i(\Delta x_{i-1}+\Delta x_i)} \quad i=2,\ldots, M; j=1,\ldots, N \quad (2.36)$$

$$d_{i,j} = -\frac{2k_{(i-1)+M+\nu(j)}}{\Delta z_{j-1}(\Delta z_{j-1}+\Delta z_j)} \quad i=2,\ldots, M; j=1,\ldots, N \quad (2.37)$$

$$e_{i,j} = -\frac{2k_{(i-2)+3M+\nu(j)}}{\Delta z_j(\Delta z_{j-1}+\Delta z_j)} \quad i=2,\ldots, M; j=1,\ldots, N \quad (2.38)$$

$$f_{i,j} = T_{i,j}^{n-1}\frac{\rho_{i,j}c_{p_{i,j}}}{\Delta t}, \quad (2.39)$$

with $\mu(j)=(M+3)(j-1)$ and $\nu(j)=(2M-1)(j-2)$.

Whereas, for the external nodes the coefficients are expressed as:

$$a_{1,1,\dots,N} = 0; \;\; d_{1,\dots,M,1} = 0 \tag{2.40}$$

$$c_{M,1,\dots,N} = 0; \;\; e_{1,\dots,M,N} = 0 \;\; . \tag{2.41}$$

Also in this case, the implemented code solves the equation system for each time step using LU factorization of the coefficient matrix, after the implementation of the initial boundary conditions.

As concerns the boundary conditions, the temperature of the last column of nodes is set equal to the environmental temperature, since in the presented experimental tests thermal equilibrium of the specimens during the heating phase was not reached. The initial temperature of the first column of nodes is set equal to the maximum temperature value of the heating phase, since thermal decays were analyzed and the heating turn-off time coincides with the cooling start time. As regards the internal nodes, the initial temperatures vary in the range between the initial temperatures of the first node and the last node; these values depend on the materials and/or defects thermal properties and are varied until the best matching between experimental and numerical curve is reached.

Finally, it is worth noticing that common commercial softwares (like for instance COMSOL), which solve heat transport problems, do not allow for 2D solutions as described above. Indeed, these softwares consider three-dimensional models for analyzing lateral and in depth heat propagation and, thus, surface boundary conditions have to be specified, which require a really huge number of input temperature data if internal non-equilibrium thermal states are considered.

Chapter III

Analysis of laboratory and *in-situ* IRT data

The implemented numerical codes were tested on two specimens made of different types of masonry structures with enclosed anomaly sources (defects). The nature of the defects (i.e., cork, plastic and tuff) simulates common building degradation causes such as voids, detachments, variation in porosity.

Then, the possibility of using the developed numerical codes for a quantitative interpretation of *in-situ* thermographic data was studied. To this aim, the codes were applied to analyze pulse-thermography data acquired in the Marcus Fabius Rufus' House (Pompeii, Italy) and the Dome of Magdeburg (Magdeburg, Germany). In particular, modelling of temperature transients allowed to define both nature and depth of the thermal anomaly sources, whose knowledge provides a significant contribution to the planning of future restorations.

3.1 Laboratory data analysis

We first validated the developed numerical codes on the thermal response of two specimens. For each specimen, experimental temperature curves of selected pixels were

compared with numerical solutions for surface nodes. To find the best agreement between experimental, T^e, and synthetic, T^s, curves, iterative cycles were implemented by varying depth, diameter and nature of the defects. Differences between synthetic and experimental curves were calculated by estimation of the mean percentage error according to the following formula:

$$e = \frac{1}{n_t}\sum_{i=1}^{n_t}\frac{|T_i^e - T_i^s|}{T_i^e}\cdot 100, \tag{3.1}$$

where n_t is the number of acquired images and T_i is the chosen pixel temperature of the i-th thermogram [K].

3.1.1 Specimen I

The specimen I (Fig. 3.1) is a one-layer structure made of a mixture of cement, sand and water, which encloses air-filled plexiglass cilinder and pieces of tuff simulating, respectively, voids and local variations of material characteristics (i.e. porosity).
A sketch of the specimen, whose size is 80×80×20 cm³, is shown in Fig. 3.2a: dark and light shapes indicate, respectively, tuff and plexiglass inserts. Geometry and depth of the defects are reported in Tab. 3.1.

Figure 3.1: View of the concrete specimen I; photo also shows the lodging support.

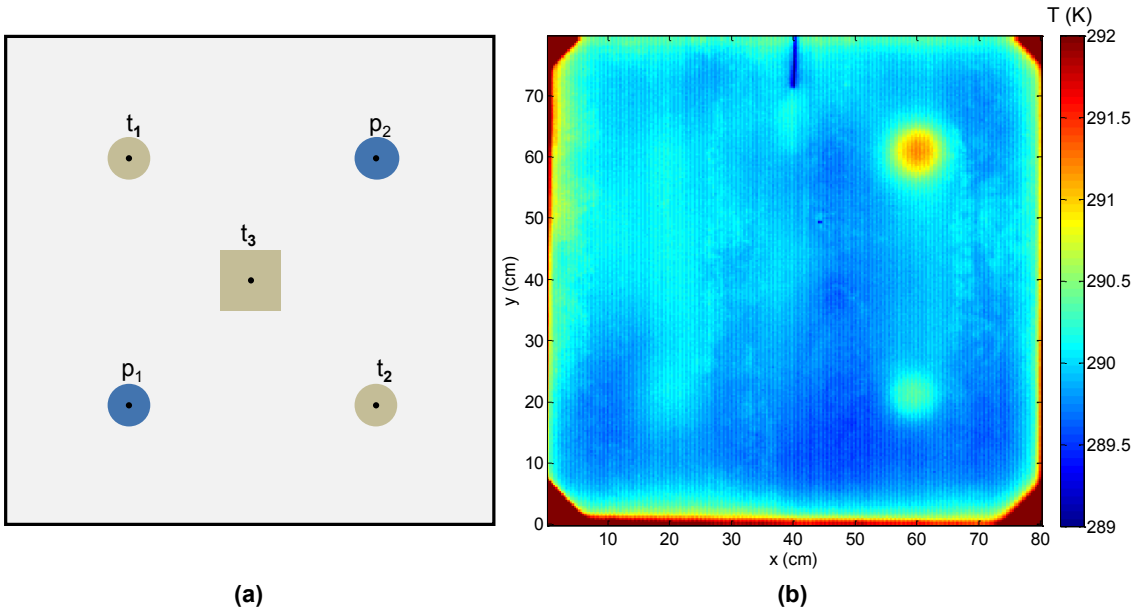

Figure 3.2: (a) Sketch of the one-layer specimen I. Dark and light shapes indicate, respectively, tuff and plexiglass inserts. (b) Thermal image acquired on the front surface of the specimen 700 s after the start of the cooling phase.

Table 3.1: Nominal diameter, thickness and depth of the plastic (p_1, p_2) and tuff (t_1, t_2, t_3) defects of the specimen I in Fig. 3.1.

Defect	Diameter (cm)	Thickness (cm)	Depth (cm)
p_1	7	3	7
p_2	7	3	2
t_1	7	3	7
t_2	7	3	2
t_3	10	3	12

The measurements were performed with a FPA ThermaCam SC3000 by using the pulse step heating technique in reflection mode. The specimen surface was heated by two halogen lamps (1.5 kW) for about 42 min. Thermal images were acquired at intervals of 10 s during both the heating (2500 s) and the cooling (2500 s) processes. The thermogram in Fig. 3.2b shows that the shallowest defects p_2 and t_2 appear well outlined, while only shadows of the other ones can be recognized. The blue line on the top is due to the presence of a metallic insert, which appears darker during the cooling phase.

3.1.1.1 Numerical simulations and experimental validation

1D and 2D simulations were performed by using the proposed numerical codes (see Chapter 2), and the obtained synthetic temperature distributions were compared with the experimental thermal transients acquired during the cooling phase. In particular, the validation of numerical models was performed by comparing the results of numerical simulations with temperature decay curves of specific anomalous thermal pixels coinciding with the midpoint of visible anomalies on the thermal maps. As regards the sound zone (i.e. the single layer made of cement), the mean temperature amongst different pixels of defect-free areas was calculated and the corresponding decay curve was compared with the synthetic decay curve of the numerical model.

Figure 3.3 shows the comparison between experimental and 1D theoretical curves for defect-free (Fig. 3.3a) and defective areas (Figs. 3.3 b-f) during the cooling phase of the experimental test.

Numerical curves were obtained by using a time step equals to the acquisition time interval, Δt=10 s, and by fixing the spatial steps according to the depth and geometry of the defects and to the thickness of the specimen. The used values for the physical properties (i.e. thermal conductivity, density and specific heat) of the investigated materials are listed in Tab. 3.2.

As discussed in the previous chapter, the boundary conditions were chosen by fixing the temperature of the first nodes equals to the highest temperature reached during the heating phase (293-294 K), the temperature of the last nodes equals to the temperature of the environment (287 K), and the temperature of the internal nodes varying in the range 291-286 K. From the matching between the experimental curves and the results of the numerical analyses, it was possible to found that the temperature of the internal nodes decreases with increasing depth and small variations of the chosen initial values produce few changes in numerical results. It is worth noting that a good agreement between experimental and theoretical curves for every investigated pixel was found with a percentage error e [Eq. (3.1)] lower than 0.02% for both 1D and 2D simulations.

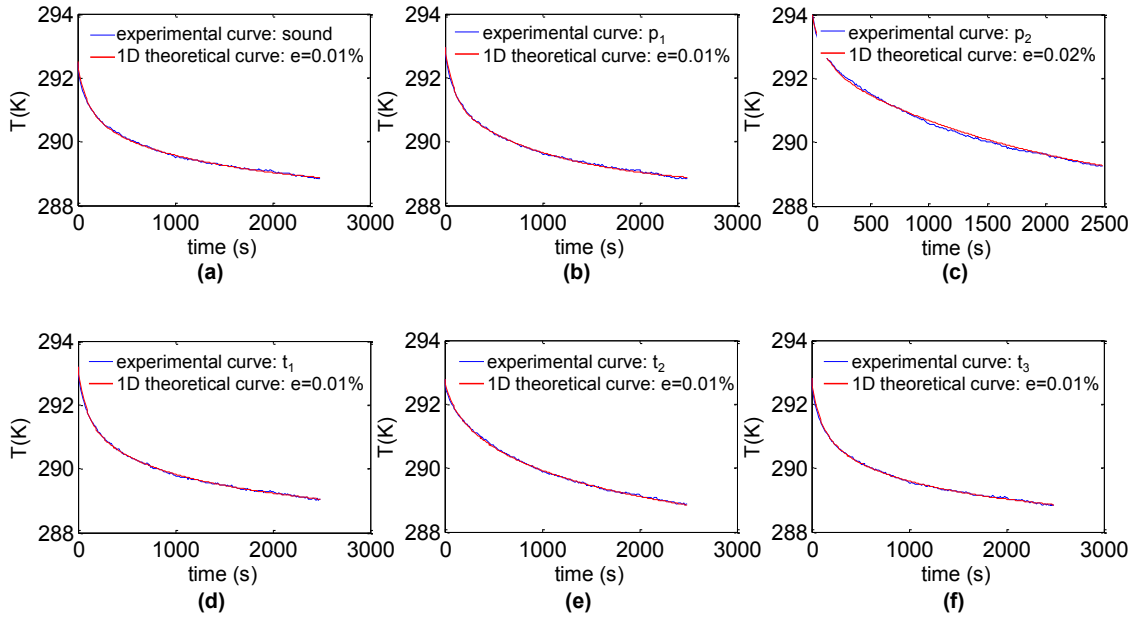

Figure 3.3: Comparison between experimental and numerical temperature curves corresponding to the investigated pixels: (a) sound, (b) p_1, (c) p_2, (d) t_1, (e) t_2, (f) t_3.
The legend also indicates the percentage error (e).

Table 3.2: Values of the material physical properties used for numerical simulations of the specimen I: ρ is the mass density, k is the thermal conductivity, c_p is the specific heat and α is the thermal diffusivity.

Material	**ρ (kg/m³)**	**k (W/mK)**	**c_p (J/kgK)**	**α (m²/s)**
Cement	2200	1.4	837	$7.6\text{x}10^{-7}$
Plexiglass	1190	0.2	1470	$1.1\text{x}10^{-7}$
Tuff	1500	0.6	900	$4.4\text{x}10^{-7}$

To estimate the resolution of the codes, iterative cycles were implemented by varying depth, radius and nature of defects. As an example, Fig. 3.4 shows the comparison between the experimental temperature decay curve of the tuff defect t_2 (see Fig. 3.2a) and the 2D theoretical curves obtained by varying, respectively, the depth (Fig. 3.4a), the radius (Fig. 3.4b) and the nature (Fig. 3.4c) of the defect.

In an iterative cycle, the numerical study is performed by varying the value of one parameter (for instance the defect depth), while the values of the others (radius and physical properties of the defect) are kept fixed to the nominal values. From the

performed 1D and 2D analyses, it is found that the codes are more sensitive to variations of the physical properties of the defects, while they are less sensitive to their lateral extension. As regards the investigations about the defect depth estimation, whose knowledge is fundamental in architectonic restoration planning, more accurate iterative cycles were performed, whose results are discussed in the paragraph 3.1.3.

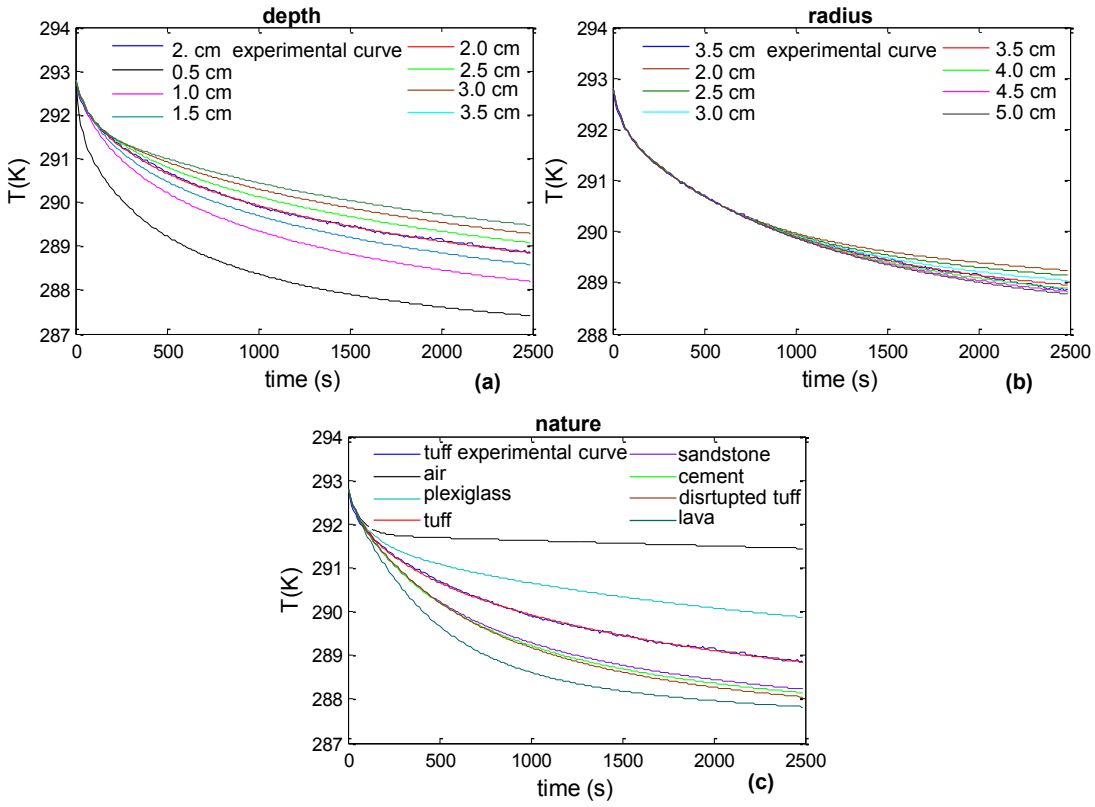

Figure 3.4: Results of numerical simulations by varying the depth (a), the radius (b) and the nature (c) of the defect t_2 of Fig. 3.2a.

3.1.2 Specimen II

The second sample is a two-layer structure, which consists of a marble support of dimension 90×90×3 cm^3 covered with plaster (Fig. 3.5). The thickness of the plaster layer is 1 cm on one half-side (A) and 2 cm on the other half-side (B), as shown in Fig. 3.6. Defects were positioned between the support and the plaster layer to simulate detachments of the plaster from the support. The defects, manufactured of three different

diameters (4, 6 and 10 cm), consist of cork disks with 0.15 cm thick (orange circles in Fig. 3.6a) and air-filled plastic bags with 0.2 cm thick (grey circles in Fig. 3.6a). Geometry and depth of the defects are summarized in Tab. 3.3. In particular, the cork disks simulate break-up of the material by virtue of their natural porous structure. Conversely, the air-filled bags, which consist of two heat welded circles with trapped air, simulate the presence of voids or micro-cavities.

Figure 3.5: View of the specimen II; photo shows the lodging support.

The inspection was carried out with a FLIR SC6000 infrared camera by using the pulse step heating technique in reflection mode. The face with plaster was thermally stimulated by a halogen lamp of 1.5 kW and thermal images were acquired at a time interval of 10 s during both heating (1850 s) and cooling (4200 s) processes.

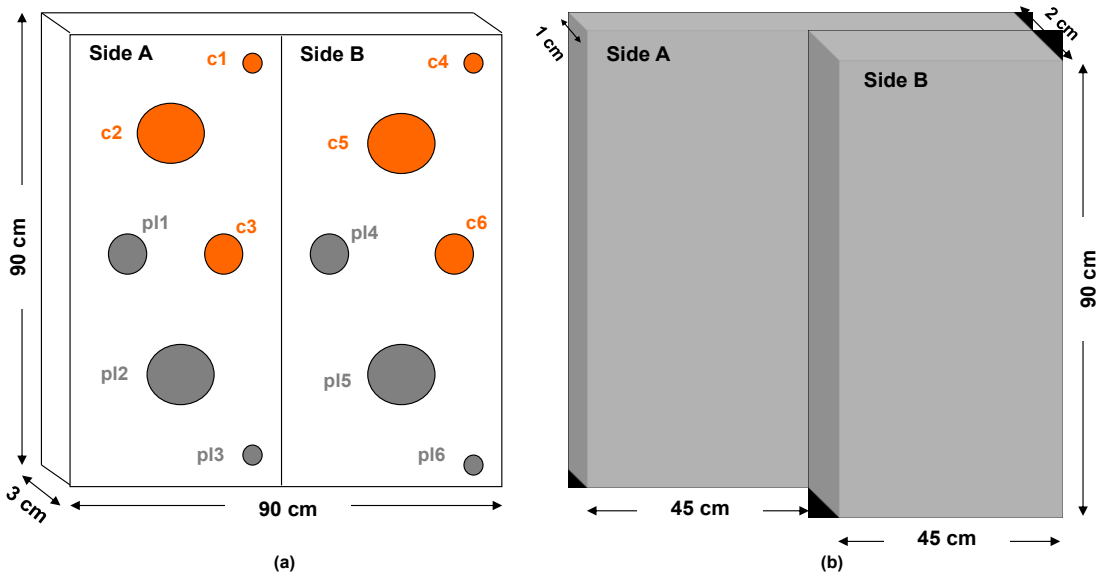

Figure 3.6: Sketch of the two-layer specimen II: defects on marble support (a) and plaster layer on the defects (b).

Table 3.3: Nominal diameter, thickness and depth of the cork ($c_1 \div c_6$) and plastic ($pl_1 \div pl_6$) defects of the specimen II in Fig. 3.6a.

Defect Side A	Diameter (cm)	Thickness (cm)	Depth (cm)	Defect Side B	Diameter (cm)	Thickness (cm)	Depth (cm)
c_1	4	0.15	0.85	c_4	4	0.15	1.85
c_2	10	0.15	0.85	c_5	10	0.15	1.85
c_3	6	0.15	0.85	c_6	6	0.15	1.85
pl_1	6	0.20	0.80	pl_4	6	0.20	1.80
pl_2	10	0.20	0.80	pl_5	10	0.20	1.80
pl_3	4	0.20	0.80	pl_6	4	0.20	1.80

Figure 3.7 illustrates two thermal images taken during the cooling phase: the first one (Fig. 3.7a) is taken 140 s after the start of the cooling process and shows that the six defects on the side A are visible, while only four defects are distinguishable on the side B, with contours not easily discernible; vice versa, in the thermogram of Fig. 3.7b, which is obtained 660 s after the beginning of the cooling process, the visibility is increased for defects under the thicker plaster layer (side B), while defects under the thinner plaster layer (side A) appear defocused. This feature is explained by considering

the longer times that heat takes to reach the top of the defects on the side B, while thermal diffusion processes on the side A provide uniform heating that prevents defects to be discernible. For both the thermograms, the plastic defects are better distinguishable than the cork ones because the air volume entrapped by cork disks is smaller than that included in the plastic bags. The thermograms also show, in the middle portion of the specimen, a vertical line due to reflections on the border of the thicker plaster layer.

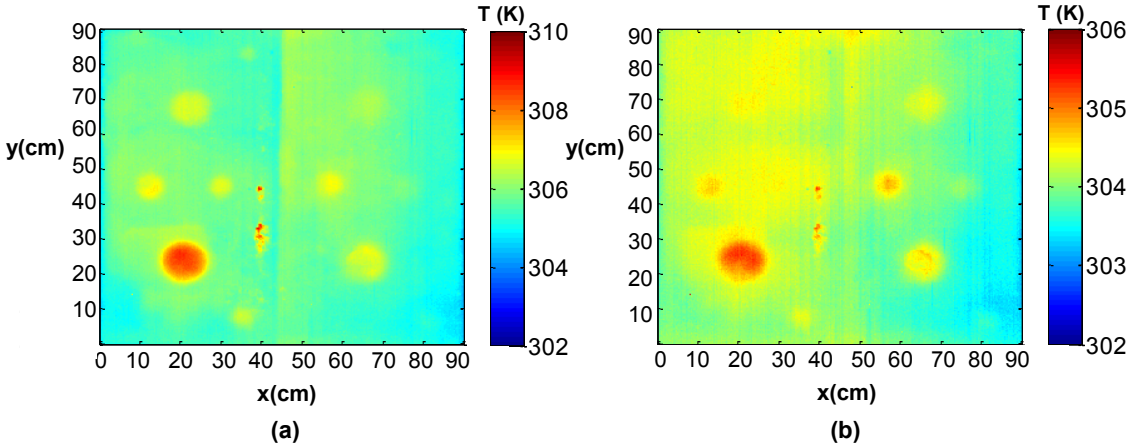

Figure 3.7: Thermal images acquired on the front surface of the specimen II (Fig. 3.6b) at 140 s (a) and 660 s (b) after the start of the cooling process.

3.1.2.1 Numerical simulations and experimental validation

As for the specimen I, 1D and 2D simulations were performed and compared with the thermal images acquired during the cooling process. The used values for the physical properties of the investigated materials are listed in Tab. 3.4.

For defective zones, the results obtained from numerical simulations were compared with the experimental thermal decays of selected anomalous pixels coinciding with the midpoint of visible anomalies, while for defect-free areas it was calculated, on both the sides of the specimen, the mean temperature along different pixels, the decay curve obtained for such a mean temperature was compared with numerical solution results.

Table 3.4: Values of the material physical properties used for numerical simulations of the specimen II: ρ is the mass density, k is the thermal conductivity, c is the specific heat and α is the thermal diffusivity.

Material	**ρ (kg/m³)**	**k (W/mK)**	**c_p (J/kgK)**	**α (m²/s)**
Plaster	1600	0.25	860	$1.82\text{x}10^{-7}$
Plexiglass	1350	0.16	1480	$8.01\text{x}10^{-8}$
Cork	480	0.08	1760	$9.47\text{x}10^{-8}$
Marble	2750	2.30	800	$1.04\text{x}10^{-6}$

Figure 3.8 shows the comparison between experimental and 1D theoretical curves for defect-free areas on side A (Fig. 3.8a) and B (Fig. 3.8b) of the specimen II. Figs. 3.9 and 3.10 show the comparison between experimental and 1D theoretical curves for defects on the side A and B, respectively.

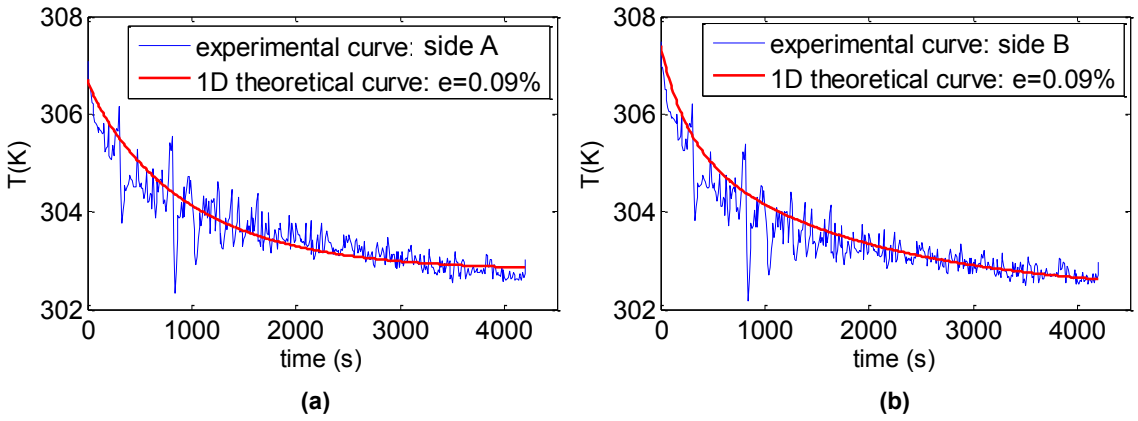

Figure 3.8: Comparison between experimental and 1D theoretical temperature curves corresponding to sound zone on side A (a) and on side B (b) of the specimen II of Fig. 3.6. The legend also indicates the percentage error (e).

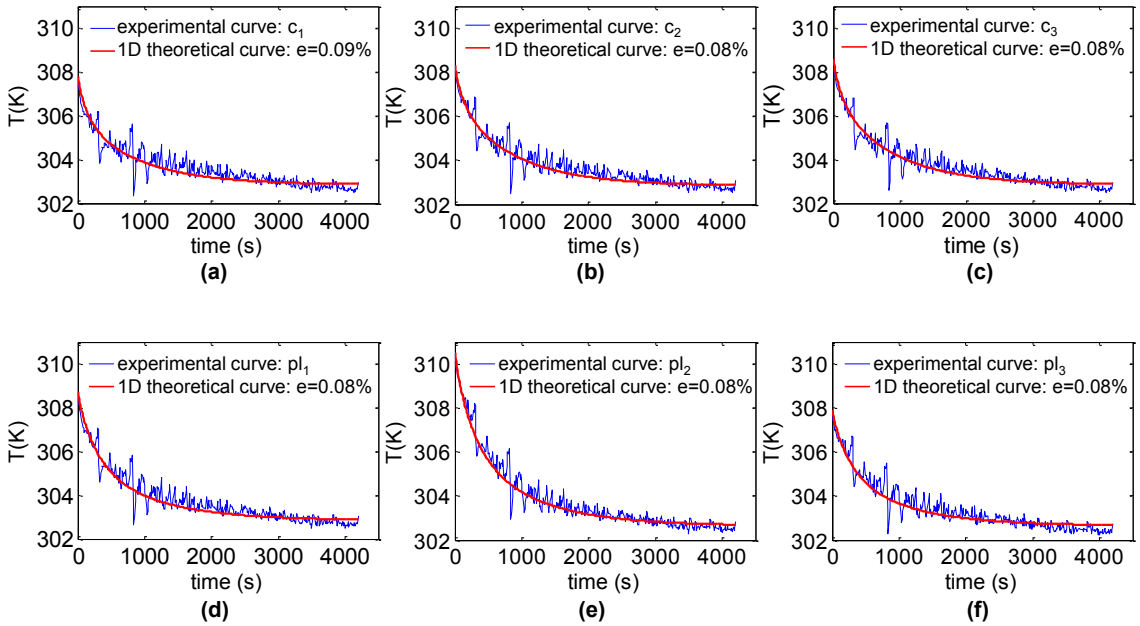

Figure 3.9: Comparison between experimental and 1D theoretical temperature curves for defects on side A of the specimen II of Fig. 3.6: (a) c_1, (b) c_2, (c) c_3, (d) pl_1, (e) pl_2, (f) pl_3. The legend also indicates the percentage error (e).

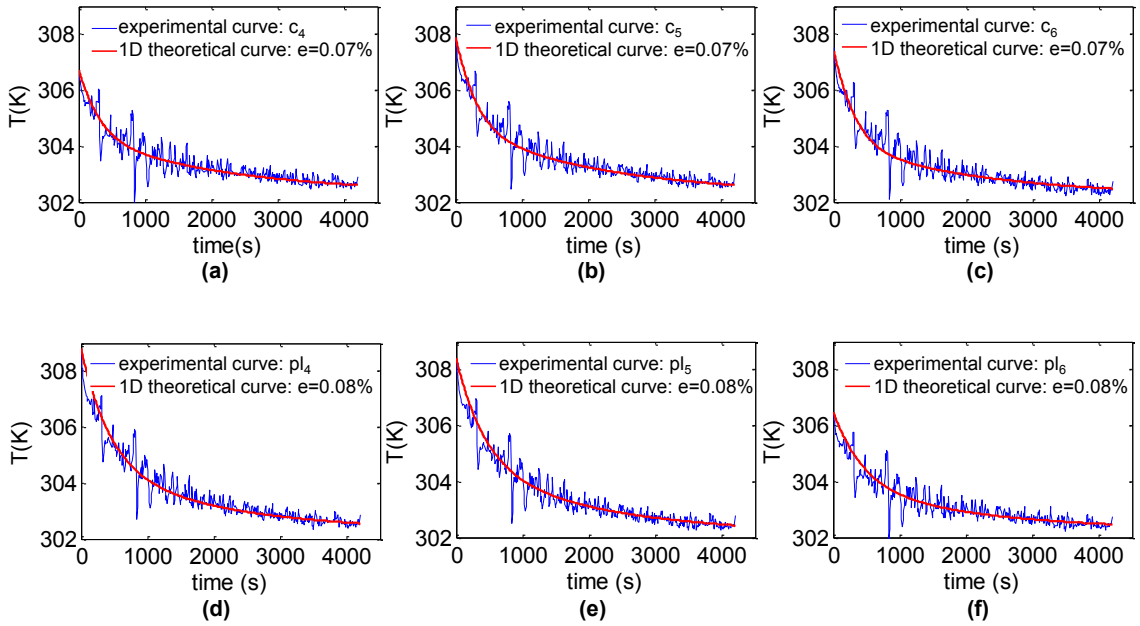

Figure 3.10: Comparison between experimental and 1D theoretical temperature curves for defects on side B of the specimen II of Fig. 3.6: (a) c_4, (b) c_5, (c) c_6, (d) pl_4, (e) pl_5, (f) pl_6. The legend also indicates the percentage error (e).

The boundary conditions were chosen by fixing the temperature of the first nodes equals to the highest temperature reached during the heating phase (308-309 K), the temperature of the last nodes equals to the temperature of the environment (302.5 K), and the temperature of the internal nodes varying in the range between 300-303 K. From the matching between the experimental curves and the results of the numerical analyses, it is found that the deeper is the defect, the larger is the number of basic nodes to be used for an appropriate modeling. In particular, for the side A, 1D synthetic decays do not significantly change for a number of nodes larger than 4 (Fig. 3.11a), while for the side B they do not change for a number of nodes larger than 5 (Fig. 3.11b). In fact, it is found that one node has to be fixed in the middle of the plaster layer to obtain a good match (Fig. 3.12).

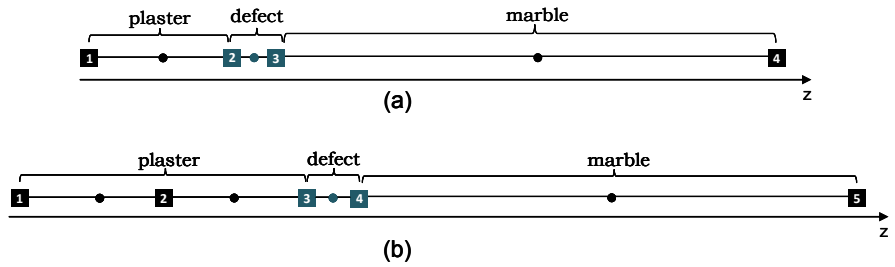

Figure 3.11: Model used for defects on side A (a) and on side B (b) of the specimen II of Fig. 3.6.

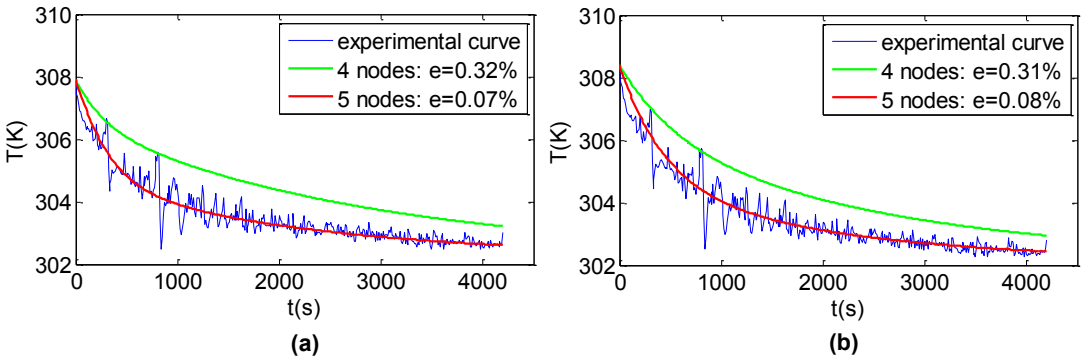

Figure 3.12: Comparison between experimental and 1D theoretical curves for defects c_5 (a) and pl_5 (b) on side B of the specimen II (see Fig. 3.6a) by using a model with 4 nodes and 5 nodes.

For 2D modeling, the best matching between experimental and synthetic decays is obtained for 3 basic nodes in the lateral direction x, and, therefore, for a number of total nodes equals to 12 for the side A and 15 for the side B.

It is worth noting that for every investigated pixel a good agreement between experimental data and numerical results is found with a percentage error, Eq. (3.1), lower than 0.1% for both 1D and 2D simulations.

To estimate the resolution of the codes, iterative cycles were implemented also for the specimen II by varying depth, radius and nature of the defects. The results of such an analysis confirm that the best agreement between experimental and numerical curves is obtained when the values of the model parameters (i.e. depth, thickness, diameter and nature) are those of the real investigated materials.

3.1.3 Discussion

The developed numerical codes were tested on thermal inspections by infrared thermography of two specimens consisting of one- and two-layer structures with several defects of different geometry and materials. Simulation results provide, with a good level of accuracy, joint information about both the nature (density, thermal conductivity and specific heat) and the geometry (width, depth) of anomaly sources in both homogeneous or multi-layer masonry structures.

It is worth noting that initial boundary conditions, which require the assignment of temperatures for each node of the grid, were used in order to calculate thermal decays starting from a non-uniform distribution of the internal temperature. If on the one hand this requirement increases the number of input data, on the other hand it allows to study non-equilibrium thermal states and to characterize thermal anomaly sources with a good resolution.

The proposed codes can be applied to different contexts, even if they may be mainly useful for architectonic restoration works, which require accurate characterization of possible defects and in particular of their depth. For this reason, iterative cycles were performed to study the code resolution. In Tab. 3.5, the results of the investigations on the two laboratory specimens are summarized. By calculating the difference, Δ, between

the estimated depth (E_{depth}) and the nominal depth (N_{depth}) of the top of the defects, regardless their nature, geometry and support, it is found a percentage error, Δ/N_{depth}, lower than 6%. It is important to note that the largest percentage errors are obtained for the shallowest defects and the accuracy increases with the defect depth, even if for larger depths the simultaneous identification of nature, thickness and diameter is less accurate.

Table 3.5: Nominal depths, N_{depth}, of the top of defects of the two investigated specimens, difference, Δ, between nominal and estimated depth, and percentage error, Δ/N_{depth}.

N_{depth} (mm)	Δ (mm)	Δ/N_{depth} (%)
8.0	0.5	~ 6.0
8.5	0.5	~ 6.0
18.0	0.5	~ 3.0
18.5	0.5	~ 3.0
20.0	0.2	~ 1.0
70.0	0.5	~ 0.7
120.0	0.5	~ 0.5

3.2 In-situ data analysis

The numerical codes were applied to pulse-thermography data acquired *in-situ* on archaeological buildings with the aim to provide a quantitative interpretation of anomaly sources very likely correlated to degradation of wall structures. In particular, the PT measurements were carried out on some inner walls of the Marcus Fabius Rufus' House, located in the archaeological area of Pompeii (Naples, Italy), with the aim to evaluate the conservation state of the walls, and on the east wing of the cloister of the Dome of Magdeburg (Magdeburg, Germany) in order to characterize its plaster score.

It is worth noting that in the case of *in-situ* measurements the model was not known *a priori*, so assumptions based on the knowledge of masonry materials were made.

3.2.1 Marcus Fabius Rufus' House

The complex of the House of Marcus Fabius Rufus is one of the most famous architectural examples in the archaeological area of Pompeii (Fig. 3.13). It is organized on four levels, gradually descending toward the sea and is a typical example of a city villa, equipped with central gardens for each housing level [Grimaldi, 2006].
The typical problems of this complex are: water infiltration, degradation of the building materials and inner inhomogeneities [Di Maio et al., 2010].

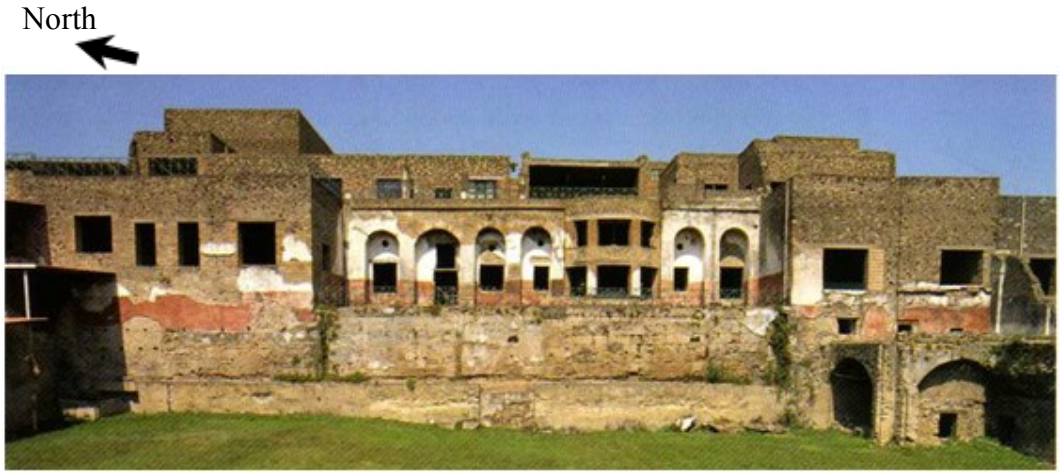

Figure 3.13: Marcus Fabius Rufus' House (Pompeii, Italy).

The inspection with infrared thermography was carried out in rooms 80 and 82, located in the second floor below (Fig. 3.14). Specifically, the south-west wall of the room 80 (Fig. 3.14b) and the north-east wall of the room 82 (Fig. 3.14c) were investigated.
The room 82 is decorated with dark painting in III Pompeian style and most likely hides an opening, which, in the past, allowed access to the environment 80. The latter has a rectangular section with a window on the west wall and a floor in tessellatum with white background and a black band.
The long-pulse thermography inspection was carried out in reflection mode by using a halogen lamp of 1.5 kW positioned in front of the selected walls. A sequence of thermal

images was acquired during both heating (1200 s) and cooling (1800 s) transient phases at time intervals of 20 s.

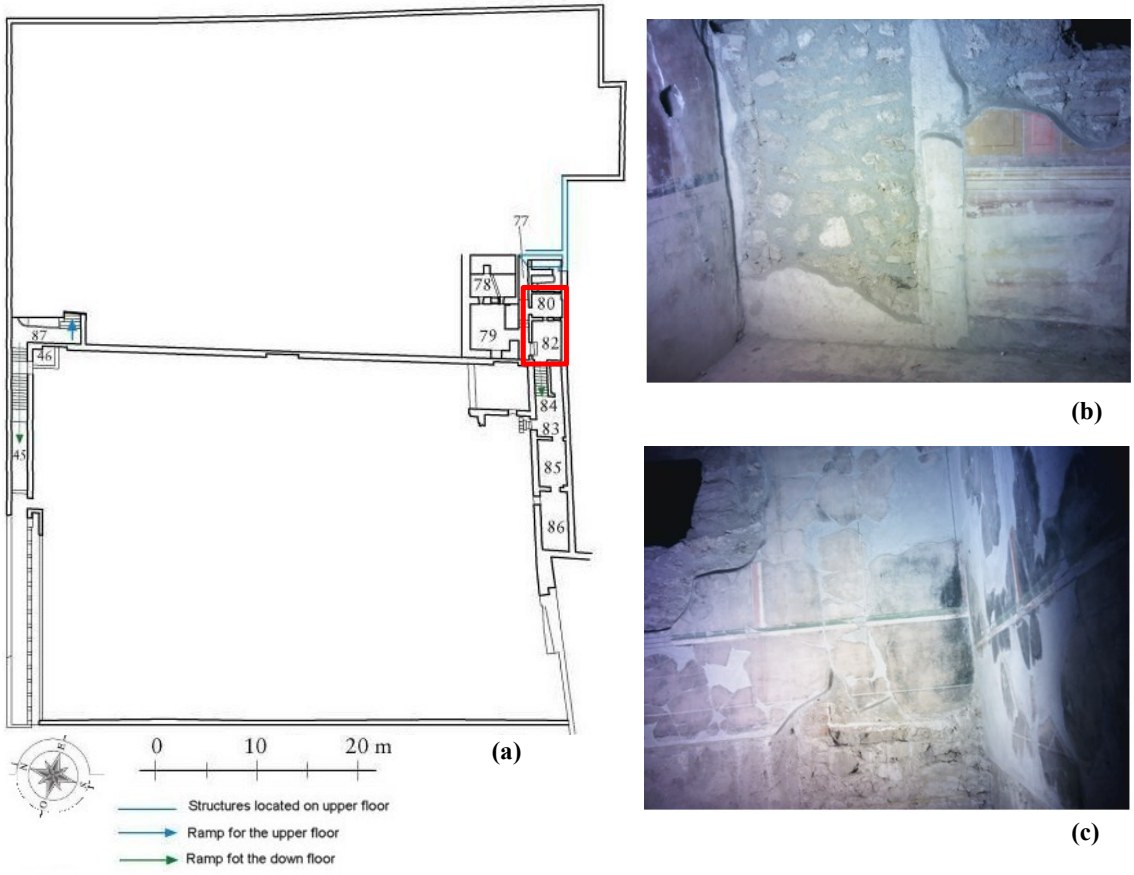

Figure 3.14: (a) Plant of second floor below of Marcus Fabius Rufus' House. The red rectangle indicates the investigated rooms: (b) south-east wall of room 80 and (c) north-east wall of room 82.

Figure 3.15 shows two thermal images acquired at the start of the cooling phase on the two investigated walls. The map shown in Fig. 3.15a, which refers to the north-east wall of the room 82, exhibits hot anomalies that are due to presence of voids, i.e. to disaggregation of the masonry structure. Conversely, the relatively low temperature anomaly, which is pointed out with an ellipse on the right side of Fig. 3.15a, indicates presence of moisture in the disaggregated masonry. Instead, the thermal contrasts that characterize the thermal image in Fig. 3.15b and which refers to the left side of the

south-west wall of the room 80, well describe the contrast between the different building materials, i.e. tuff bricks (yellow areas) and mortar (red areas). Interestingly, no thermal anomalies are evident along the doorjamb (black rectangle in Fig. 3.15b), which, as observed *in-situ*, is constituted by marble (M in Fig. 3.15b) with a plaster cover (P in Fig. 3.15b) of about 4 cm of thickness.

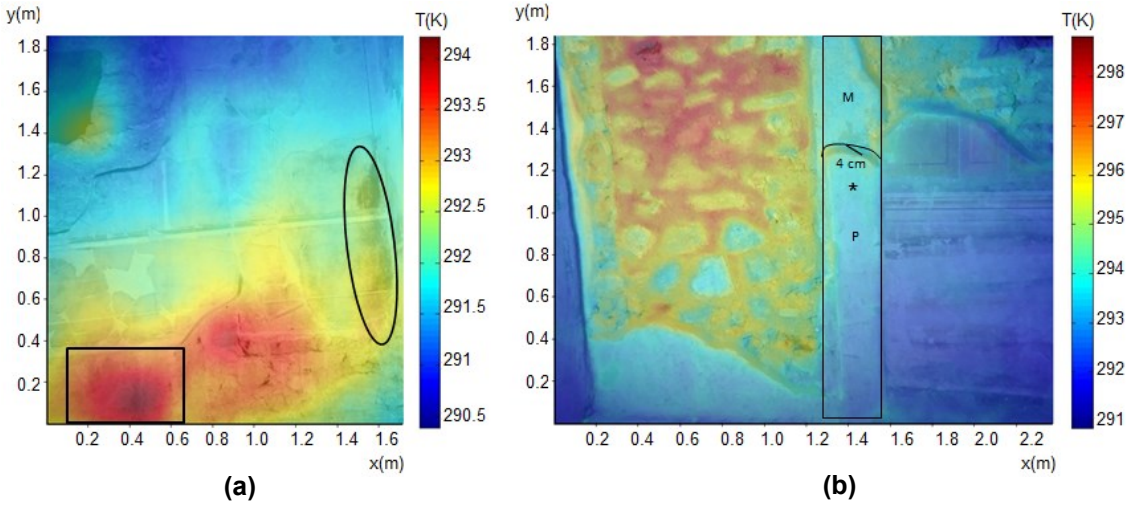

Fig. 3.15: Thermal images acquired on the north-east wall of the room 82 (a) and on the south-west wall of the room 80 (b) (see Fig. 3.14).

3.2.1.1 Numerical results

The developed numerical codes were applied to model the thermal anomalies shown in the maps of Fig. 3.15. The theoretical models have been formulated on the basis of the knowledge of masonry materials typical of Pompeian buildings [Di Maio et al., 2012a]. The physical properties used for the numerical simulations are listed in Tab. 3.6. The numerical study has been performed by using both 1D and 2D codes [Di Maio et al., 2012b]. However, here only the 1D results of the thermal anomalies marked in Fig. 3.15a are presented, since they are located near the edges of the IRT image and an estimation of their extension was not possible.

Table 3.6: Material physical parameters used for the numerical simulations.

Material	ρ [kg/m³]	k [W/(m·K)]	c_p [J/(kg·K)]	α (m²/s)
Mortar	1600	0.7	840	5.21×10^{-7}
Disrupted Mortar	1000	0.5	900	5.56×10^{-7}
Tuff	2270	1.7	1000	7.49×10^{-7}
Disrupted Tuff	2000	1.5	1300	5.77×10^{-7}
Sarno limestone	1500	0.7	900	5.18×10^{-7}
Lava	2480	3.3	780	1.71×10^{-6}
Plaster	1900	1.1	837	6.92×10^{-7}
Wet plaster	2270	0.7	900	3.42×10^{-7}
Marble	2750	2.3	800	1.04×10^{-6}

As previously said, the yellow anomaly indicated with an ellipse in Fig. 3.15a is due to the presence of moisture visible to the naked eye, so the thickness of the water infiltration was studied. The best fitting curve was obtained for a model made of 4 cm of plaster of which the first two made of wet plaster (Fig. 3.16).

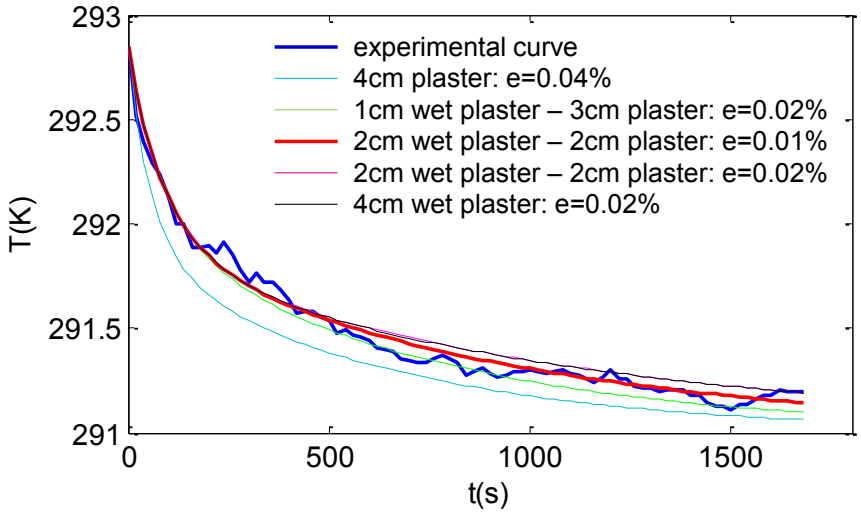

Figure 3.16: Results of numerical simulations for the yellow zone delineated by an ellipse in Fig. 3.15a by considering different thicknesses of the wet plaster layer.
The legend also indicates the percentage error (e).

Figure 3.17, instead, shows the results of the comparison between experimental and theoretical curves for the red area pointed with a box in Fig. 3.15a. As can be seen from the photo in Fig. 3.14c, in the lower part of the wall the plaster is missing, so the model has been built considering mortar in the surface layer. Several possible anomaly sources were considered with different depth and thickness; the best comparison between theoretical and experimental curves was obtained for a model consisting of: 1 cm of mortar, 1 cm of disrupted mortar and 4 cm of tuff (red line in Fig. 3.17).

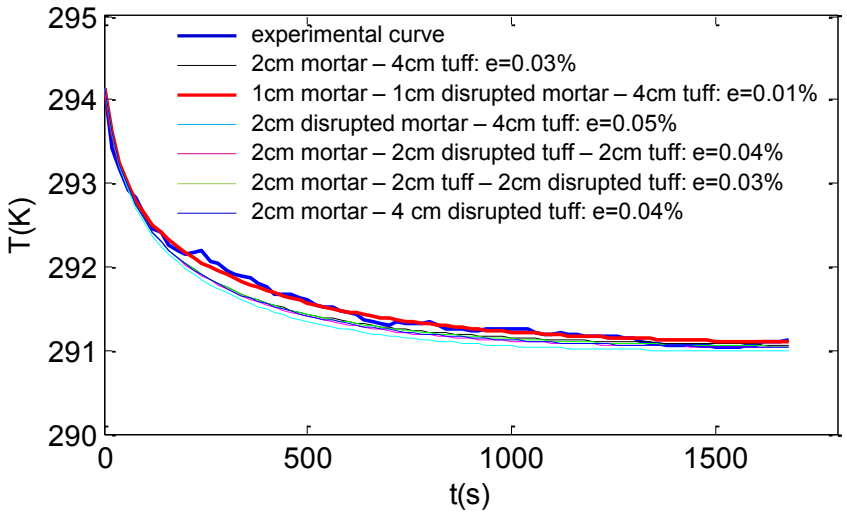

Figure 3.17: Results of numerical simulations for the red area delineated by a box in Fig. 3.15a by considering different nature, thickness and depth of the anomaly source. The legend also indicates the percentage error (e).

It is also interesting to note that the fit worsen if a different background (i.e. no tuff) is used, as shown in Fig. 3.18.

A good agreement between experimental and theoretical curves for both investigated thermal anomalies of Fig. 3.15a was found with a percentage error *e* [Eq. (3.1)] lower than 0.01%. However, an estimate of the radius of the anomaly sources was not possible as they are located near the edges of the IRT image (see Fig. 3.15a), thus not allowing to properly appreciate the temperature variations indicative of the anomaly limits.

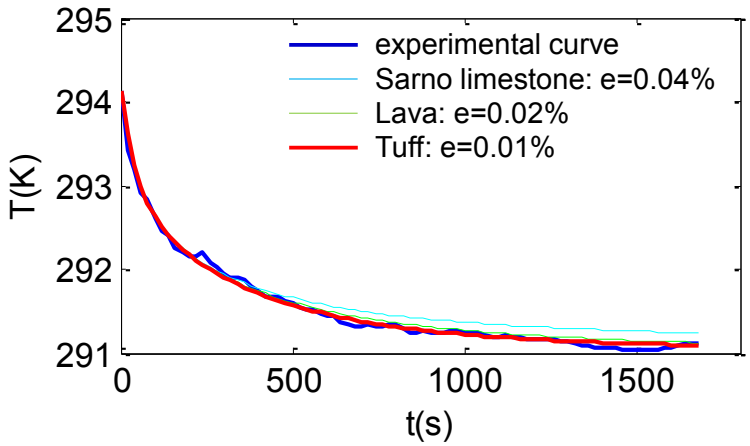

Figure 3.18: Results of numerical simulations for the red area of Fig. 3.15a by considering different nature of the background. The legend also indicates the percentage error (e).

About the south-west wall of the room 80 (Fig. 3.14b), the thermal response of the lower sector of the jamb was modelled. This area apparently does not show thermal contrast with respect to the upper part, where the marble was brought to light by the fall of the plaster. Fig. 3.19 shows the comparison between the experimental thermal curve related to the pixel indicated with an asterisk in Fig. 3.15b and the theoretical temperature decay curve obtained for a two-layer model consisting of plaster (4 cm) and marble (3 cm). It is worth noting that even if the marble is not visible, the numerical analysis predicts its presence under the plaster layer.

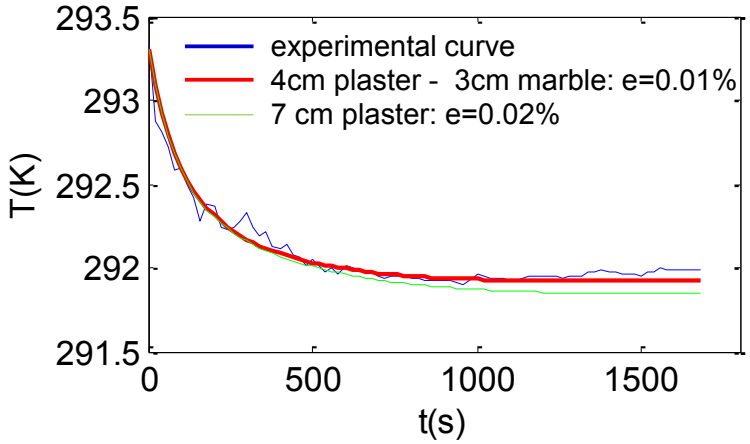

Figure 3.19: Comparison between experimental and theoretical temperature curves for the pixel indicated with an asterisk in Fig. 3.15b by considering the different nature of the bottom layer. The legend also indicates the percentage error (e).

3.2.2 Dome of Magdeburg

The Dome of Magdeburg, built in 937 by Emperor Otto I, is the oldest Gothic cathedral in Germany (Fig. 3.20). In 955, the church building was transformed into a basilica in Romanesque style. In 1207, the imperial cathedral was burned and suffered extensive damage. Two years later, reconstruction work began on the site of the original building and it took more than 300 years to build the current cathedral.

One of the most significant artworks of the Cathedral of Magdeburg is the plaster score located at the east wing of the cloister from the 13th century. It shows decorative drawings at the edges, while in the central part displays Emperor Otto I and his two wives: Eadgyth and Adelaide (Fig. 3.21). The surface of the original plaster is very hard and dense. It consists of three plaster layers and a sandstone background [Große Ophoff et al., 2011]. Into the ductile plaster, the scores have been scratched (by material removal) and pressed [Maierhofer, personal communication].

Figure 3.20: Dome of Magdeburg (Magdeburg, Germany).

At the upper border, most of the sectors have been repaired by using the fell old plaster or new plaster. Since only some parts of the scores are resumed with new plastering, the surface appears very inhomogeneous. Additionally, deformations of the plaster, cracks, flaws, different paintings and dirt prevent the visibility of the scores [Maierhofer, personal communication].

In order to plan future restoration works, thermography tests were carried out to obtain information about the state of conservation of the plaster scores.

Figure 3.21: Plaster scores at the Cathedral of Magdeburg
[recording from E.H. von Flottwell, 1891].

3.2.2.1 Test procedure

After the mounting of the scaffold, the plastering has been investigated with active thermography by using an artificial heating source, i.e. an infrared radiator. The structure was divided into four sectors of area equal to about 1 m^2 (Fig. 3.22) and each was heated at a distance of 10 cm for about 5 min by moving the radiator. Thermal images were acquired in both heating and cooling phases for 15 min with a time step of 0.2 s.

Fig. 3.22: The east wing of the Magdeburg Dome cloister. The yellow boxes show the investigated sectors.

Figure 3.23 shows the thermal images acquired during the cooling phase, which overlap the investigated structure. All the maps exhibit the high level of degradation of the wall (yellow areas), and, in particular, high-amplitude thermal anomalies (red areas in Fig. 3.23) are indicative of the occurrence of voids, i.e. disaggregation of the masonry structure or old restorations.

In order to provide useful information for future restoration of the cathedral, in terms of nature and depth of the anomaly sources, the implemented numerical codes have been applied.

Fig. 3.23: Thermal images that overlap the investigated structure. The numbers indicate the modeled anomalies.

3.2.2.2 Quantitative data analysis

The building typology of the Dome is known in more detail than the one of Pompei's house. The wall structure of the Dome is made of a layer of limewash, particle size 0.3-1.6 mm, and two layers of lime mortar, with a thickness between 1 and 4 mm, which overlap a sandstone background [Große Ophoff et al., 2011]. On the basis of this information, a model of the structure was hypothesized for each defective zone, and then the corresponding theoretical thermal response was calculated and compared with the experimental transient. Different theoretical curves were obtained by varying physical properties, number of nodes, distance between nodes and initial temperature of the internal nodes until the best comparison was reached.

It is worth noting that the study was performed by using the 1D code, since 1D and 2D analysis tests provided percentage errors of the same order of magnitude (see sections 3.1.1.1 and 3.1.2.1), and the purpose of the quantitative data interpretation was aimed at defining nature, depth and thickness of the anomaly sources.

The study allowed to define thermal anomaly sources attributable to the degradation of the lime mortar layer at different depths, and only in one case to identify an anomaly due to renovation of the lime mortar layer [Di Maio et al., 2013]. The used values for the physical properties (i.e. thermal conductivity, density and specific heat) of the investigated materials are listed in Tab. 3.7.

Table 3.7: Material physical parameters used for numerical simulations.

Material	ρ **[kg/m³]**	k **[W/(m·K)]**	c_p **[J/(kg·K)]**	**α (m²/s)**
Lime wash	2180	1.5	720	9.5×10^{-7}
Lime mortar	1600	0.7	1000	4.4×10^{-7}
Mortar	1600	0.2	860	1.4×10^{-7}
Disrupted Mortar	200	0.2	800	1.2×10^{-6}
Air	1.29	0.026	1010	2.0×10^{-5}
Sandstone	2150	1.3	840	7.2×10^{-7}

As illustrative cases, the modelling of three anomalies is here presented: in the first case, the thermal anomaly (1 in Fig. 3.23) is due to restoration, in the second and third cases (respectively, 4 and 5 in Fig. 3.23), the anomalies are ascribable to degradation of lime mortar.

In more detail, in the first case the best fit is obtained for a model with a layer of mortar with different physical properties of original lime mortar located at 2.1 mm (Fig. 3.24a). In fact, as Fig. 3.24b shows, a good match is obtained only for the model with mortar instead of lime mortar layer (Fig. 3.24a), so we hypothesized a renovation of this part of wall.

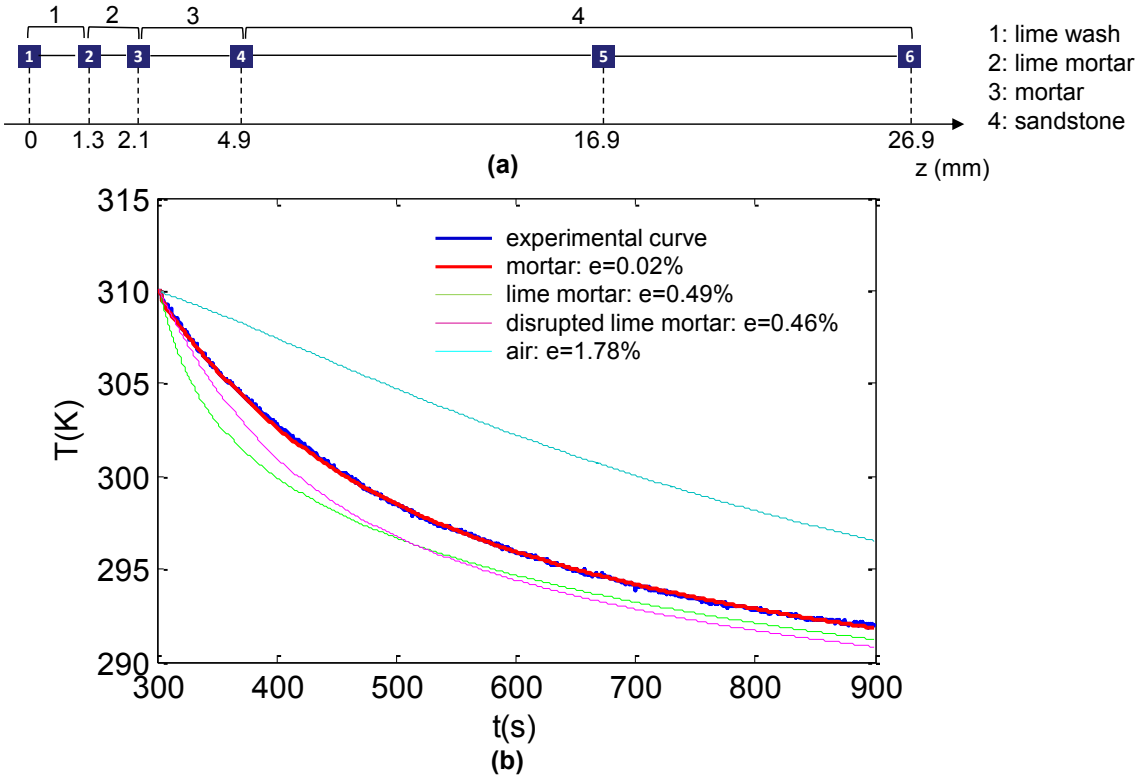

Figure 3.24: a) Model with 6 nodes in depth direction *z*. b) Numerical simulations by varing the nature of the anomaly source 1.

About the degradation of lime mortar, two cases will be discussed: thermal anomaly 4 and 5 in Fig. 3.23. For the anomaly 4, the best fit was attained for a model with disrupted lime mortar at 2.2 mm of depth (Fig. 3.25). Moreover, to illustrate the

sensitivity of the numerical code, in Tabs. 3.8 and 3.9 the results obtained for the numerical simulations are shown by varying, respectively, depth and thickness of the thermal anomaly source.

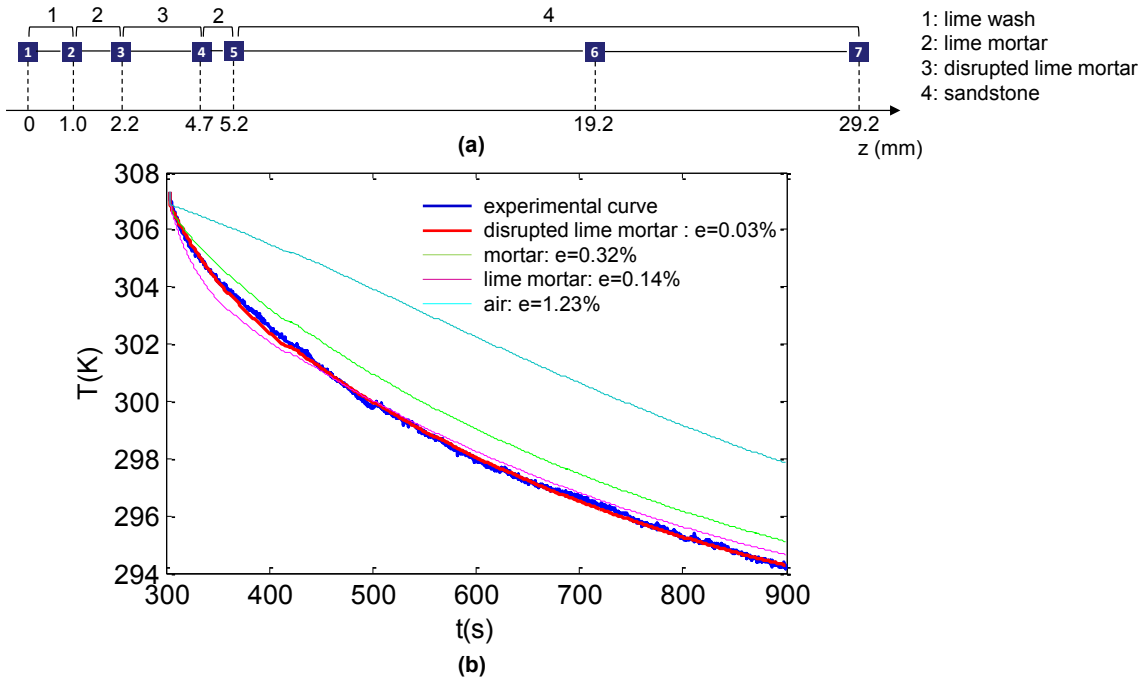

Figure 3.25: a) Model with 7 nodes in depth direction *z*. b) Numerical simulations by varing the nature of the anomaly source 4 in Fig 3.23.

Table 3.8: Results of numerical simulations by varying the depth of the thermal anomaly source 4 in Fig. 3.23.

dp (mm)	1.4	1.6	1.8	2.0	**2.2**	2.4	2.6	2.8	3.0
e (%)	0.14	0.11	0.07	0.04	**0.03**	0.04	0.06	0.10	0.13

Table 3.9: Results of numerical simulations by varying the thickness of the thermal anomaly source 4 in Fig. 3.23.

th (mm)	0.5	1.0	1.5	2.0	**2.5**	3.0	3.5	4.0	4.5
e (%)	0.36	0.27	0.18	0.09	**0.03**	0.08	0.16	0.25	0.33

The anomaly 5 in Fig. 3.23, instead, was modelled with a disrupted lime mortar layer at 0.7 mm of depth (Fig. 3.26a), but, in this case, the surface layer is lime mortar because the lime wash was fall. It is worth noting that a good match between experimental and theoretical curves (Fig. 3.26b) was obtained only by assuming a model with a surface layer made of lime mortar and not lime wash as that used for the analysis of other thermal anomalies. This result is very interesting because it shows the high sensitivity of the numerical codes with respect to the nature of the materials even when the layers are very thin.

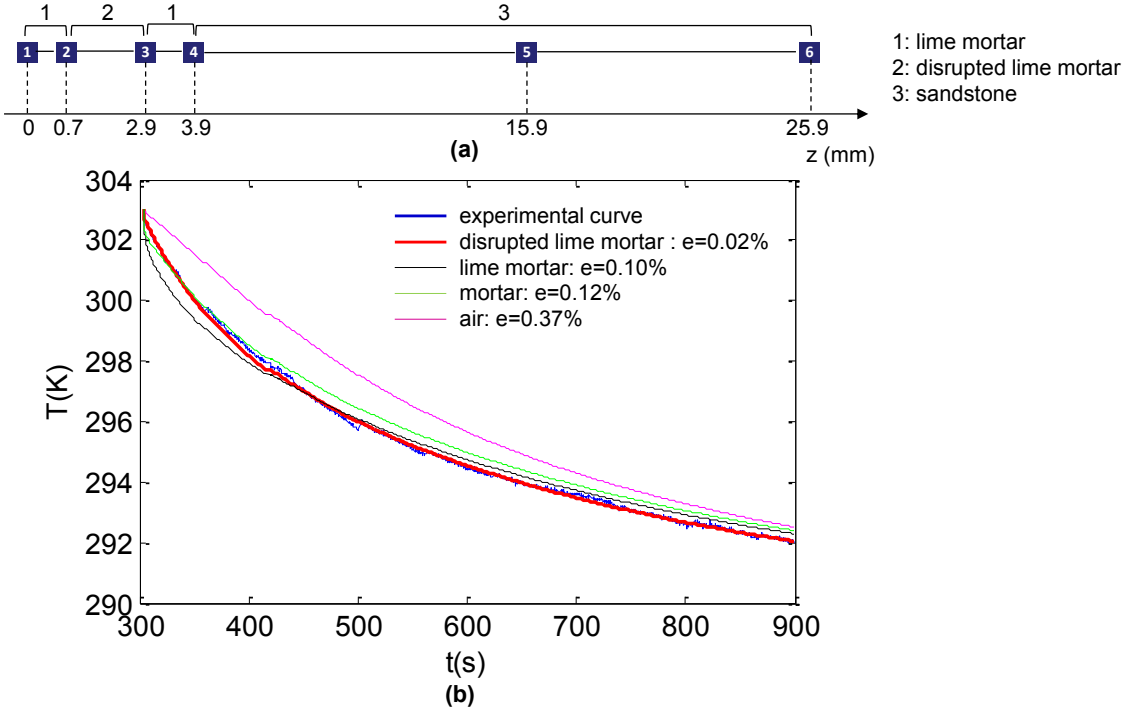

Figure 3.26: a) Model with 6 nodes in depth direction *z*. b) Numerical simulations by varing the nature of the thermal anomaly source 5 in Fig. 3.23.

Interestingly, the large number of simulations performed has shown that the numerical codes are sensitive to small changes also in the thermal conductivity values. Indeed, in the case of the anomaly 5 of Fig. 3.23, the best agreement between synthetic and experimental curves was obtained with a value of 0.1 W/mK and not with 0.2 W/mK

(Fig. 3.27); this means that a strong degradation of the mortar characterizes that sector of the wall.

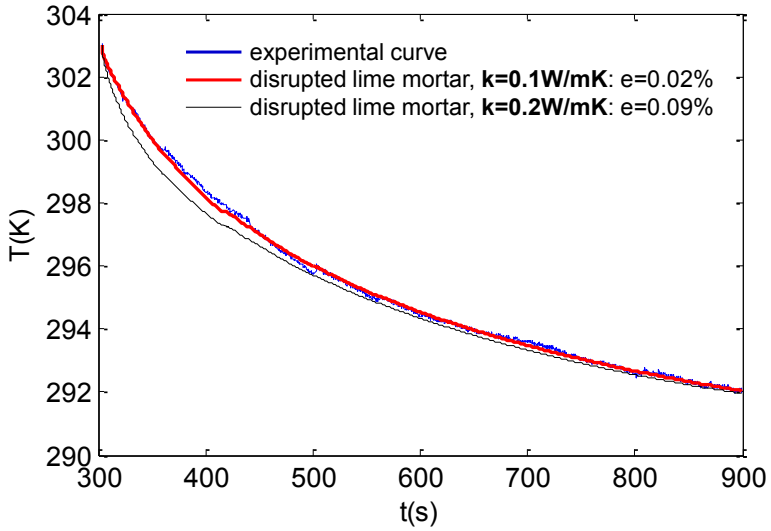

Figure 3.27: Comparison between the numerical result for k=0.1 W/mK and for k=0.2 W/mK.

3.2.3 Discussion

The developed numerical codes have been used for quantitative interpretation of long pulse thermography data acquired *in-situ*.

Both in the case of the Pompei's house and of the Magdeburg Dome, numerical models are found that well reproduce experimental thermal decays.

In particular, in the case of the Pompei's house it has been possible to reveal layered structures also in absence of evident thermal anomalies on the thermograms, and to identify the state of conservation of the constituent materials. In the case of the Magdeburg Dome, the numerical study allowed to define thickness, depth and nature (i.e. density, thermal conductivity and specific heat) of the thermal anomaly sources, attributable mainly to the degradation of the lime mortar layer at different depths. Table 3.10 summarizes the results of the investigations on the cloister of the Dome of Magdeburg.

Table 3.10: Results of numerical simulations for IRT measurements at the Dome of Magdeburg.

	Anomaly source	**dp [mm]**	**th [mm)]**	***e* [%]**
1	Mortar	2.1	2.8	0.02
2	Disrupted Mortar	0.7	1.7	0.02
3	Disrupted Mortar	1.0	1.2	0.02
4	Disrupted Mortar	2.2	2.5	0.03
5	Disrupted Mortar	0.7	2.2	0.02
6	Disrupted Mortar	2.7	1.5	0.03
7	Disrupted Mortar	1.0	2.2	0.03
8	Disrupted Mortar	3.1	1.7	0.03

In conclusion, the implemented numerical codes allowed us to characterize *in-situ* thermal anomaly observations, providing helpful indications for the planning of restoration work.

Chapter IV

Analysis of thermal conductivity models and thermographic data for hazard assessment at Campi Flegrei

In this chapter, the results of two different studies will be summarized. First, the results of numerical simulations aimed at reproducing the last 40,000 years of the Campi Flegrei volcanic history are reported. In particular, the purpose of this study is to verify if the high temperatures measured in the geothermal wells drilled inside the caldera can reasonably be reproduced under the assumption of heat loss from a magma chamber through conduction. Then, long-term time series of thermographic data acquired at the Campi Flegrei monitoring station of Pisciarelli are analyzed in order to develop numerical methods for quantifying information from continuous IR data. As both analyses concern the Campi Flegrei volcanic field, a brief summary of the eruptive history of Campi Flegrei is initially given.

4.1 Geological and volcanological outline of Campi Flegrei caldera

The Campi Flegrei (CF) is a quaternary caldera located west of the city of Naples and includes the islands of Procida and Ischia, as well as submarine vents in the north-western Gulf of Naples (Fig. 4.1).

The interpretation of stratigraphic data and the analysis of geological, geochronological and geophysical data allowed to establish that its structure was mainly formed during two major caldera collapses related to the eruptions of the Campanian Ignimbrite (CI, 39 ky BP, 200 km^3 DRE - dense-rock equivalent) [Barberi et al., 1978; Fisher et al., 1993; Rosi et al., 1996; Civetta et al., 1997; Fedele et al., 2002; Pappalardo et al., 2002], and the Neapolitan Yellow Tuff (NYT, 15 ka BP, 50 km^3 DRE) [Scarpati et al., 1993; Wohletz et al., 1995; Orsi et al., 1996; Deino et al., 2004]. In particular, Orsi et al. [1996, 2004], using such major eruptions as two important stratigraphic markers, have divided the volcanic history of the CF caldera into three periods (see Fig. 4.2):

- Volcanism older than 39 ky;
- Volcanism between 39 ky and 15 ky;
- Volcanism younger than 15 ky

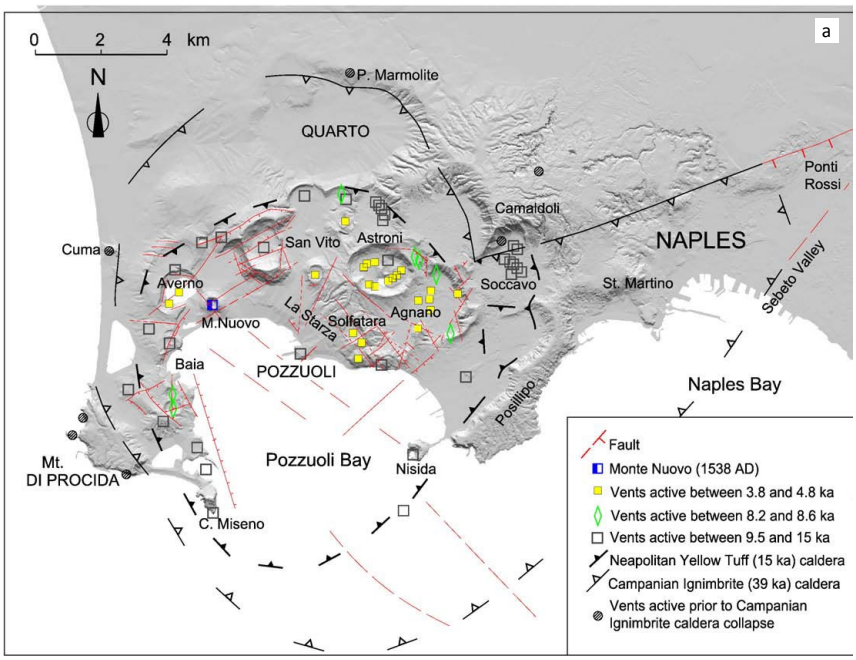

Figure 4.1: Geological map of the Campi Flegrei caldera [from Arienzo et al., 2010].

The evidence of at least 300,000 years of volcanic activity prior to CI has been demonstrated by surface/subsurface geology and radiometric data [Cassignol and Gillot, 1982; De Vivo et al., 2001; Rolandi et al., 2003]. Furthermore, recent age determinations have documented activity as early as 70 ky [Pappalardo et al., 1999; Scarpati et al., 2013] related to volcanism extending outside the limits of the present caldera [Di Renzo et al., 2011].

The Campanian Ignimbrite, which has been often thought to be associated with the early caldera depression [e.g. Rosi and Sbrana, 1987], was erupted about 39 ky BP [De Vivo et al. 2001] and is considered the main volcanic-tectonic event in the area (Volcanic Explosivity Index - VEI=6).

The subsequent high size event (VEI=5), the Neapolitan Yellow Tuff phreatoplinian eruption, occurred c. 15 ky BP [Deino et al., 2004] and its pyroclastic deposits cover an area of more than 1,000 km^2. After each caldera collapse, volcanism was restricted within the collapsed area.

After the NYT eruption, both volcanism and deformation were very intense within the caldera, with at least 72 eruptions (the last of which is the Monte Nuovo eruption, occurred in A.D. 1538) grouped in 3 epochs of activity separated by variable long periods of quiescence (Fig. 4.2). The eruptions were mainly low to medium magnitude events, except one event in the I epoch and another in the III epoch.

The I epoch lasted from 15 to 9.5 ky and was mainly characterized by a monogenetic explosive eruptions, among which only the Pomici Principali eruption (12 ka; Lirer et al., 1987; Di Vito et al., 1999; Smith et al., 2011) was a high magnitude eruption. After a quiescence of about 1 ky, the II epoch began and lasted from 8.6 to 8.2 ky, giving rise to low magnitude eruptions, mainly occurring along the NYT caldera borders (Fig. 4.1). The III epoch lasted from 4.8 to 3.8 ky after a 3.5 ky quiescence period and was characterized by the La Starza block uplift [Orsi et al., 1996; Di Vito et al., 1999]. During this epoch, vents migrated toward the inner part of the caldera and eruption activity was both explosive and effusive, although on the whole less intense than the previous; the only high-magnitude eruption was the Agnano-Monte Spina eruption (4.1 ky; De Vita et al., 1999; Dellino et al., 2001, 2004) accompanied by a volcano-tectonic

collapse centered in the present Agnano plain. The last eruptive event is the VEI=3 Monte Nuovo eruption occurred in 1538 A.D. [Di Vito et al., 1987; D'Oriano et al., 2005].

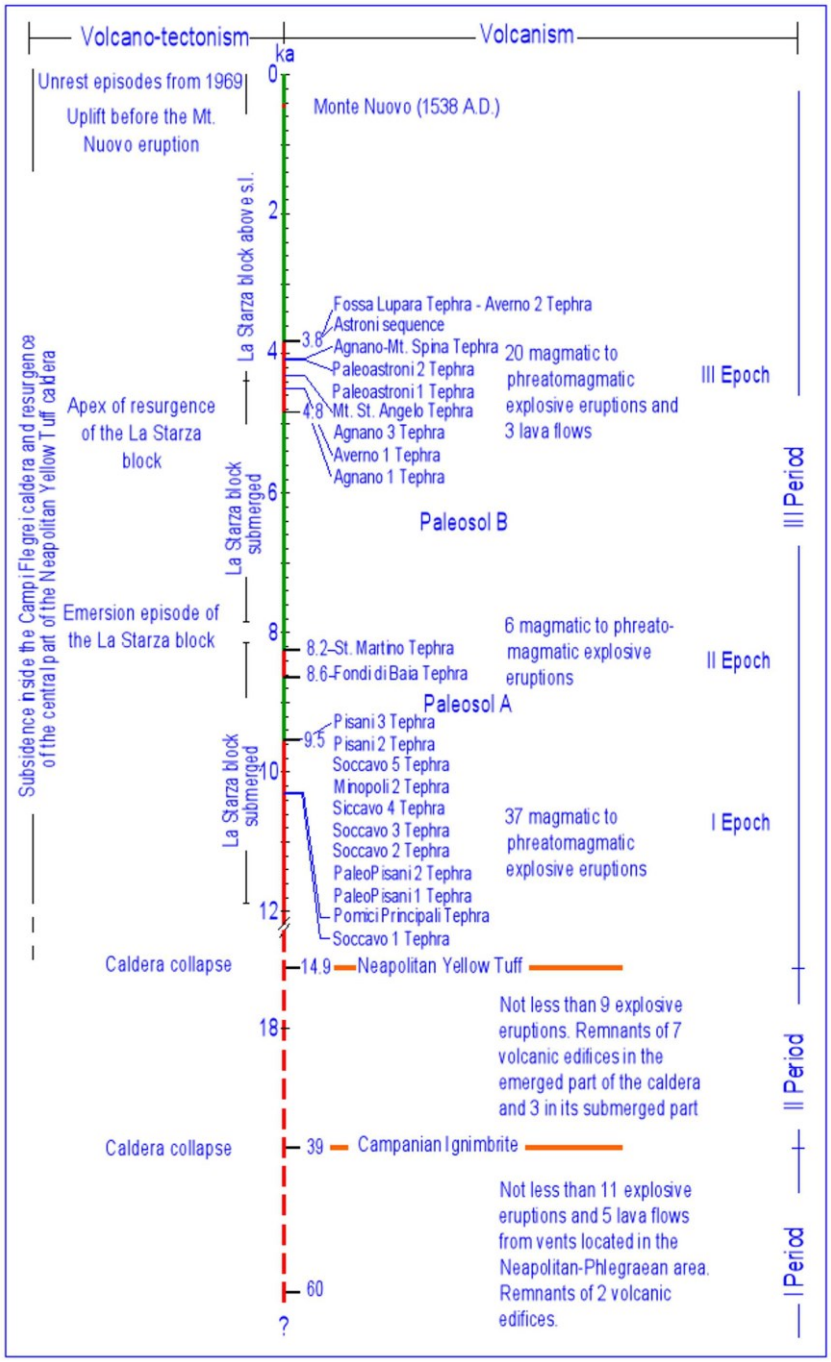

Figure 4.2: Chronostratigraphy of the volcanic and deformational history of the Campi Flegrei caldera [from Orsi et al., 2004].

The volcanic system is still active, as it is proven by intense degassing mainly from fumaroles, ground deformation, seismic activity and thermal anomalies [De Vivo et al., 2010 and references therein].

The first records of slow movements at Campi Flegrei are testified by sea-level markers on Roman coastal ruins, which are sensitive to large, secular deformation. The first – and most studied – archaeological site is the Roman market-place (Macellum, or Serapeum) in Pozzuoli. It has been the object of intensive research, starting shortly after its excavation in 1750 [Breislak, 1792; Forbes, 1829; Niccolini, 1839, 1845; Babbage, 1847; Lyell, 1872; Gunther, 1903; Parascandola, 1947]. Remains of shells of a marine mollusc, Lithodomus lithophagus, have been found into three 13-m standing marble columns, recording the vertical movement of the ground with respect to sea-level. Parascandola [1947] presented the first reconstruction of historical ground movements, later modified by Dvorak and Mastrolorenzo [1991], and, in the last years, by Morhange et al. [1999] (Fig. 4.3).

During the 1984 crisis, a meaningful ground uplift, on the order of several metres, was accompanied by more than 16,000 eartquakes [Barberi et al., 1984; Caliro et al., 2007] of which the most energetic ones ($3<M<4$) with epicenters in the Solfatara[1] of Pozzuoli [Vilardo et al., 1991]. Subsequently there was a slow subsidence trend [Troise et al., 2007] periodically interrupted by small uplift in 1989, 1994, 2000 [Bianco et al., 2004; Lanari et al., 2004], 2004-2006 [Saccorotti et al., 2007; Trasatti et al., 2008] and the last, still in progress [Del Gaudio et al., 2010]. The recent episodes of ground deformation and seismicity are considered the result of the interaction between the hydrothermal system and the deeper magmatic gases [Bonafede and Mazzanti, 1998; Chiodini et al., 2003, 2010] of which the fumarolic field of Solfatara is another testimony [Chiodini et al., 2010].

After a brief period of no movement between 2004 and 2005, from the end of 2005 a new phase of uplift has started and is still in progress, proceeding with a variable speed and with a total displacement of about 20 cm (Fig. 4.4). In conjunction with the ground

[1] The Solfatara is a volcanic crater generated about 4 ky BP.

uplift, the local seismicity reappraised, still with low energy (M <2.0) and shallow epicentres (h <4.0 km) [Martini, 2013].

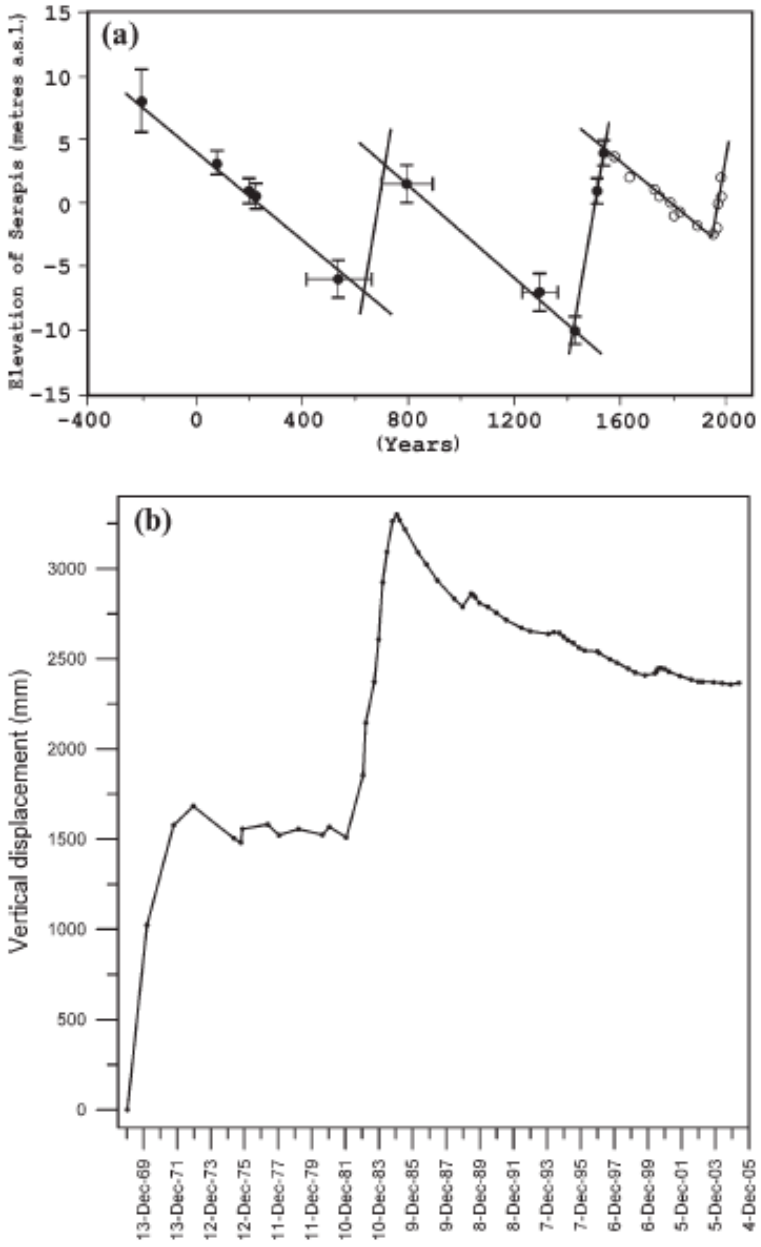

Figure 4.3: (a) Schematic history of vertical movements at Macellum in Pozzuoli, known as Serapis Temple. Black circles represent the constraints found from radiocarbon and achaeological measurements by Morhange et al. [1999]; white circles (post-1538) represent inferences by Dvorak and Mastrolorenzo [1991]; (b) Vertical ground displacements as recorded at Pozzuoli harbour by levelling data in the period 1969–2005 [Del Gaudio et al., 2005; Macedonio and Tammaro, 2005] [from De Natale et al., 2006].

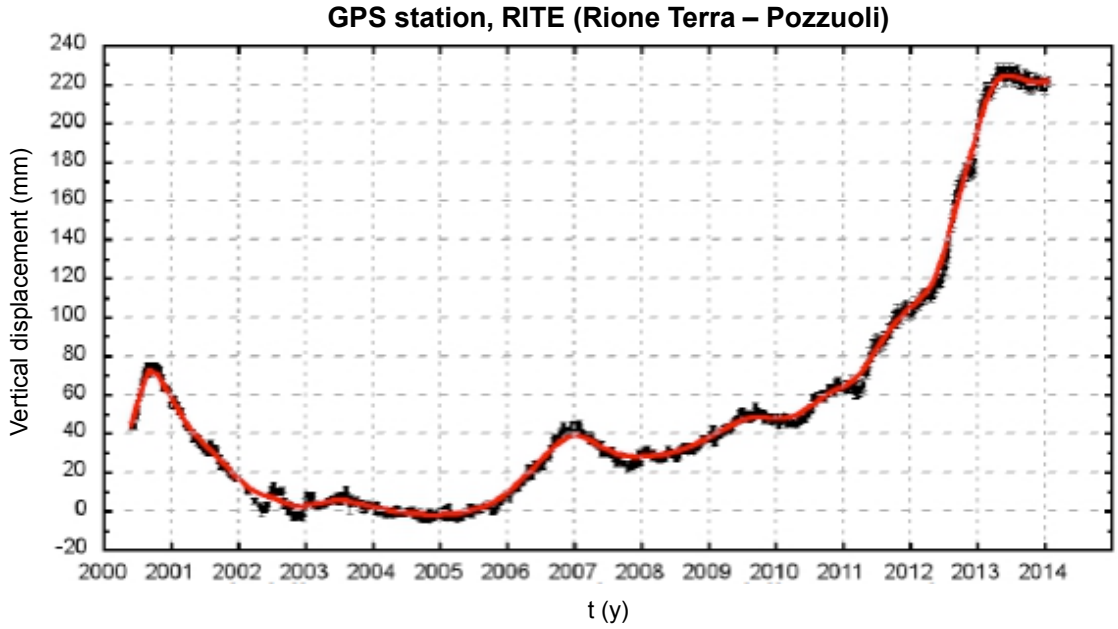

Figure 4.4: GPS elevation data from RITE station [from www.ov.ingv.it].

Generally the present process of uplift differs from that recorded in the last century due to the rate of displacement, significantly lower than that of bradyseismic crisis of the Eighties, and to the low frequency of occurrence of seismic activity, generally in sequences of small swarms [Martini, 2013]. Furthermore, geochemical monitoring has detected a variation in the fluids emitted from fumaroles and ground in both internal and external area of Solfatara.

According to Caliro et al. [2007], the fumaroles of Solfatara are fed by a mixture of magmatic and hydrothermal fluids, the latter with a high CO_2 content (65-70% in weight). The peaks of the CO_2/H_2O ratio, which have systematically followed the bradyseismic events, were interpreted, by numerical simulations, as the surface manifestation of the injection of magmatic gas into the hydrothermal system that feeds the fumaroles (Fig. 4.5) [Caliro et al., 2007].

After the last minor episode of ground uplitf in 2000, the fraction of magmatic fluids of the fumaroles of Solfatara has progressively increased (Fig. 4.5), anticipating the equally slow uplift process started at the end of 2005.

The present phenomenology has recently been interpreted as caused by recurrent episodes of injection of magmatic fluids in the hydrothermal system, with a rate of injection increasing over time [Chiodini et al., 2012]. This process would also lead to a significant pressure increase beneath the ground surface, with the resulting seismic and deformation observed phenomena.

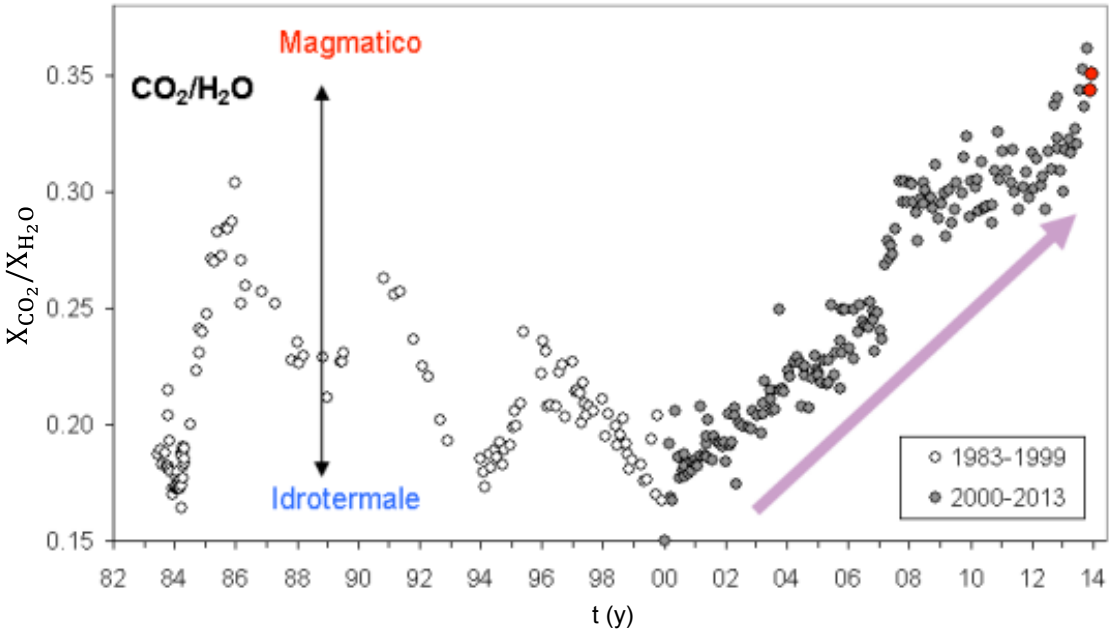

Figure 4.5: Chronogram of compositions of Bocca Grande fumarole expressed as X_{CO_2}/X_{H_2O} and the computed fraction of magmatic fluids [from www.ov.ingv.it].

4.2 Conductive numerical models for thermal evolution of the Phlegraean magmatic system

In the following, the results of numerical simulations aimed at reproducing the last 40,000 years of the Campi Flegrei (CF) volcanic history are reported. The hypothesized model bases on the occurrence of a magma chamber whose bottom temperature is maintained at constant temperature. Specifically, the main purpose is to verify if the high temperatures measured in the geothermal wells drilled inside the caldera (see Fig. 4.6) can reasonably be reproduced under the assumption of heat loss from a magma chamber through conduction. Since the aim of our study is to verify the plausibility of such an

assumption, attention is focused only on the major volcanic events (i.e. the Campanian Ignimbrite and the Neapolitan Yellow Tuff eruption), and a rather basic model is adopted.

In the last decades, several conductive models have been proposed to study the thermal evolution of the Phlegraean magmatic system. Giberti et al. [1984] studied the CF thermal hystory in terms of a magma chamber that cools progressively without refillings from depth and with volume progressively reduced by magma extraction to the surface. Bonafede et al. [1984] derived an analytical solution for size reduction of a spherical magma chamber cooling by conduction. A series of 2D conductive/convective numerical models, with different magma chamber configurations, were analyzed by Wohletz et al. [1999]. Their modeling of the Phlegraean magmatic system has shown that conduction heat transport is not able to reproduce the measured geothermal gradients, even those measured in boreholes at Licola situated outside the caldera rim, where convection is expected not to play a predominant role.

Since the analysis of Wohletz et al. [1999] was performed by using a not detailed discretization of the physical properties values, in the following a numerical analysis of 1D and 2D conductive models is performed to verify if a better characterization of rock physical properties can improve the results obtained by Wohletz et al. [1999]. The results of such analysis, which are illustrated in the next sections, are the subject of a scientific article currently under review at Bulletin of Volcanology [Di Maio et al., 2014].

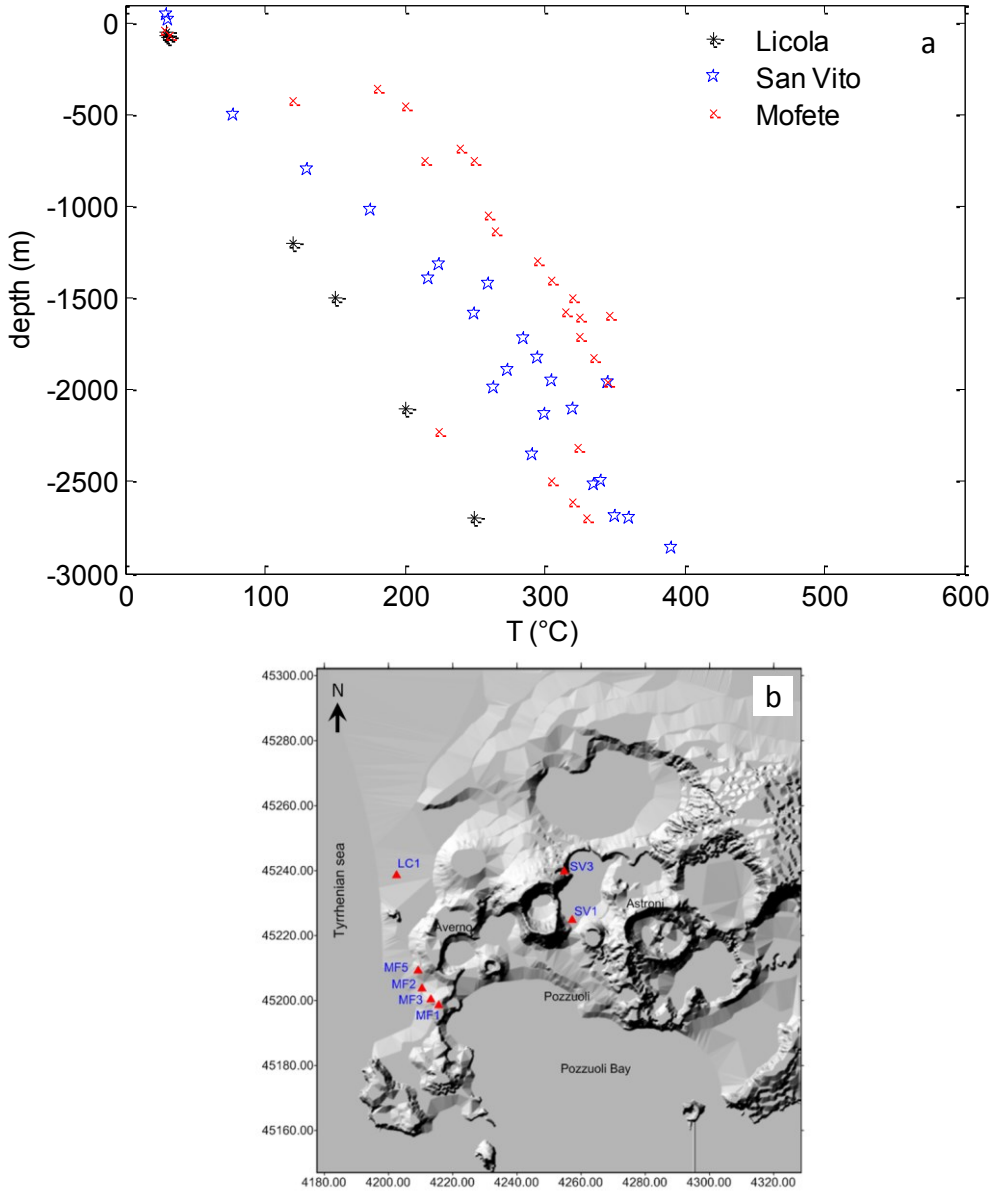

Figure 4.6: a) Geothermal gradients measured at Licola (black asterisk), San Vito (blu star) and Mofete (red cross) (see Fig. 4.1b) [AGIP, 1987; Corrado et al., 1998; Piochi et al., 2014]. (b) DTMM of the Phlegraean Fields area. Red triangles indicate the Licola (LC1), San Vito (SV1 and SV3) and Mofete (MF1-5) drilling wells [Agip, 1987].

4.2.1 Model constraints

To develop the thermal model, data from geological, geochemical and geophysical studies are taken into account. As concerns the rock density profile, a common model of the deep stratigraphy is considered, consisting of volcanic and marine sediments (density

2000 g/cm^3, up to a depth of about 0.5 km), NYT (density 2200 kg/m^3 from 0.5 to 0.9 km), volcanic and marine sediments between the products of the CI and NYT eruptions (density 2400 g/cm^3 from 0.9 to 2 km), CI (density 2600 g/cm^3 from 2 to 2.5 km) and tuffs and tuffites youger than 39 ky (density 2600 g/cm^3 deeper than 2.5 km) (Fig. 4.7a) [AGIP, 1987; Orsi et al., 1996; Di Vito et al., 1999; Di Maio et al., 2000; Zollo et al., 2008].

The emplacement of the magmatic body (t=0 for simulations) is fixed in correspondence of the CI eruption (39 ky B.P.). Thus, to take into account the main collapse occurred 15 ky ago, related to the NYT eruption and located in the central part of the CI eruption, the rock density profile used for our modelling was modified as follows: density of 2000 kg/m^3, up to a depth of about 0.9 km; 2200 kg/m^3, from 0.9 km to 2.3 km; 2400 kg/m^3, from 2.3 km to 2.9 km, and 2600 kg/m^3 deeper than 2.9 km (Fig. 4.7b).

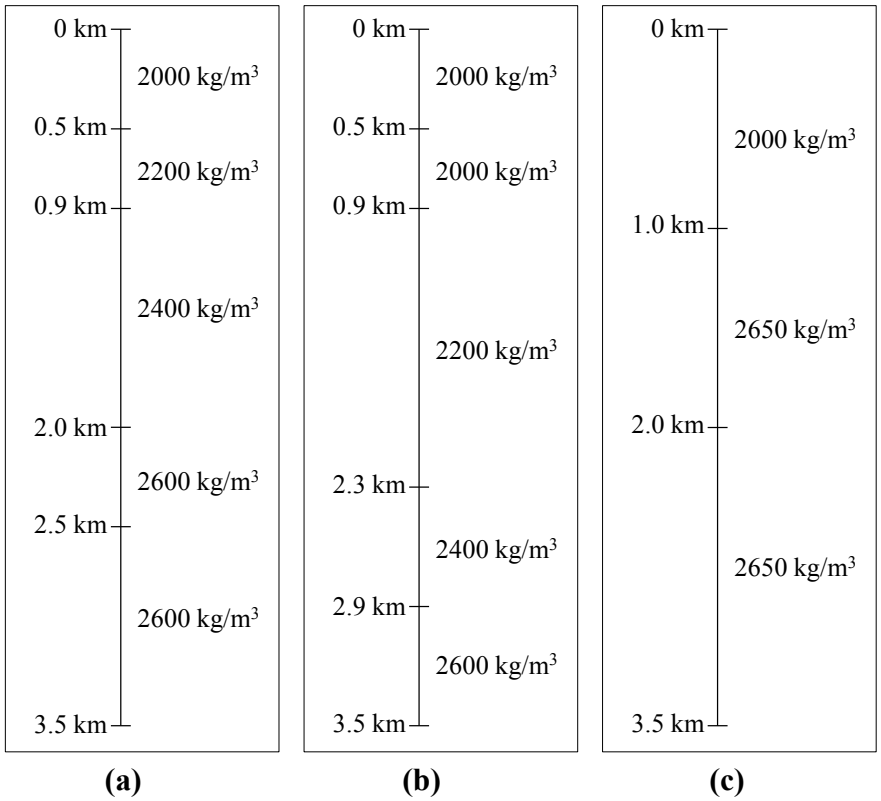

Figure 4.7: Density profile values for the stratified model of the CF volcanic district before (a) and after (b) the collapse in the central part of the CI caldera used for the simulations; (c) density values used by Wohletz et al. [1999].

It is worth noticing that numerical simulations were performed by slightly varying the density values, ρ, of rocks in Fig. 4.7b. Specifically, the density values were varied by adding up to a maximum of ±200 kg/m^3 from 0.5 km to 3 km of depth. Even if an increase (decrease) of the temperatures is found for an increase (decrease) of the ρ values, likely correlated to greater fluid intakes within the fracture network, the temperature changes produce variations in the thermal equation solution of the order of 10 °C, thus limiting the effects of density changes on the evolution of the temperature profile in the Phlaegrean caldera.

As concerns the rock specific heat capacities, a value of 1000 J/kg°C is used for the whole model [Todesco et al., 2003; Rinaldi et al., 2010]. As it occurs for density changes, an increase (decrease) of temperature is found if c_p increases (decreases), but the effects of c_p changes on temperature values are limited: indeed changes in the solutions are found of 10 °C at most for variations of about 100 J/kg°C in c_p values. Contrary to what happens for the density and the specific heat, numerical solutions of the heat equation are very sensitive to changes in the thermal conductivity. Specifically, it was found that if k of the node i is increased (or decreased), the temperatures of nodes shallower than i increase (or decrease), while those of deeper nodes decrease (or increase). Thus, accurate estimates of thermal conductivities, k, are crucial for an appropriate modeling of the investigated system. In the models proposed by Wohletz et al. [1999], a poor detailed profile of k values with depth is used (shown in Fig. 4.8 as dashed line). Unlike Wohletz et al. [1999], different profiles of k values are used for the proposed 1D modelling, which reproduce the geothermal gradients observed at Licola, San Vito and Mofete drilling wells (Fig. 4.6).

The thermal conductivities were varied in a range of values according to intervals reported in literature for the considered materials [Giberti, 1984; Clauser and Huenges, 1995; Vosteen and Schellschmidt, 2003]. Fig. 4.8 shows the k profiles that are able to describe the measured thermal gradients in the proposed 1D modelling (see next section). Interestingly, the sharp changes in k values, which were found exclusively from the numerical analysis, agree well with discontinuities in the stratigraphic succession proposed by Zollo et al. [2008], shown in Fig. 4.9. Specifically, the first sharp change in

k values at depths from 500 to 1000 m would characterize the passage from water saturated volcanic sediments to pre- and post-caldera volcanic and marine deposits (-500 m ÷ -1000 m), while the second less sharp change in *k* values would characterize the passage from such deposits to metamorphic rocks (-2500 m ÷ -2900 m).

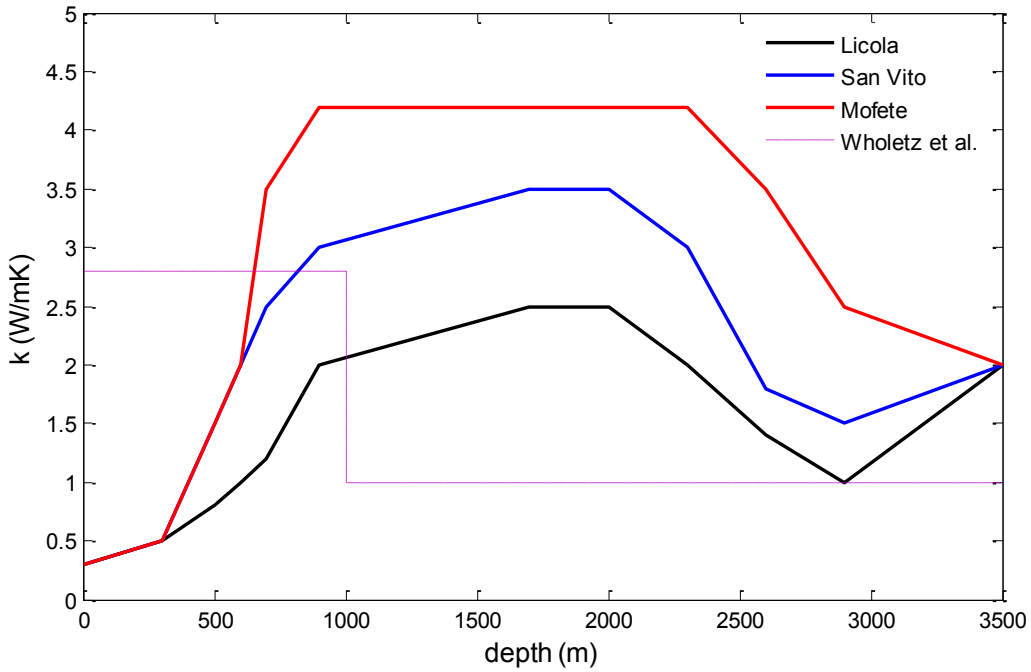

Figure 4.8: Distribution of the thermal conductivity values as a function of depth for reproducing thermal gradients observed at Licola (black line), San Vito (blu line) and Mofete (red line) drilling wells. The dashed line is the thermal conductivity profile extrapolated by the 2D model of Woheltz et al. [1999].

Finally, to solve the heat flow equation and simulate the thermal evolution of the considered geothermal system, the initial thermal gradient for the Phlegrean area has to be fixed. In this regard, two choices were made. According to the first choice (case 1), a thermal gradient of 30°C/km was considered consistent with the regional gradient of this area [Della Vedova et al., 1991]. According to the second choice (case 2), a thermal gradient of 30°C/km was considered for all the basic nodes (see Chapter 2) except for those at the bottom of the system, for which initial temperatures were set to higher values to simulate the presence of fractured rocks filled of hot gases, presumably

originated by volcanic events preceding the CI eruption. In both cases, the initial temperatures of nodes simulating the magma chamber was set to 1000 ^{o}C and only the temperatures of the bottom (i.e. the last nodes of the model at a depth of 8500 m) were maintained constant during the evolution.

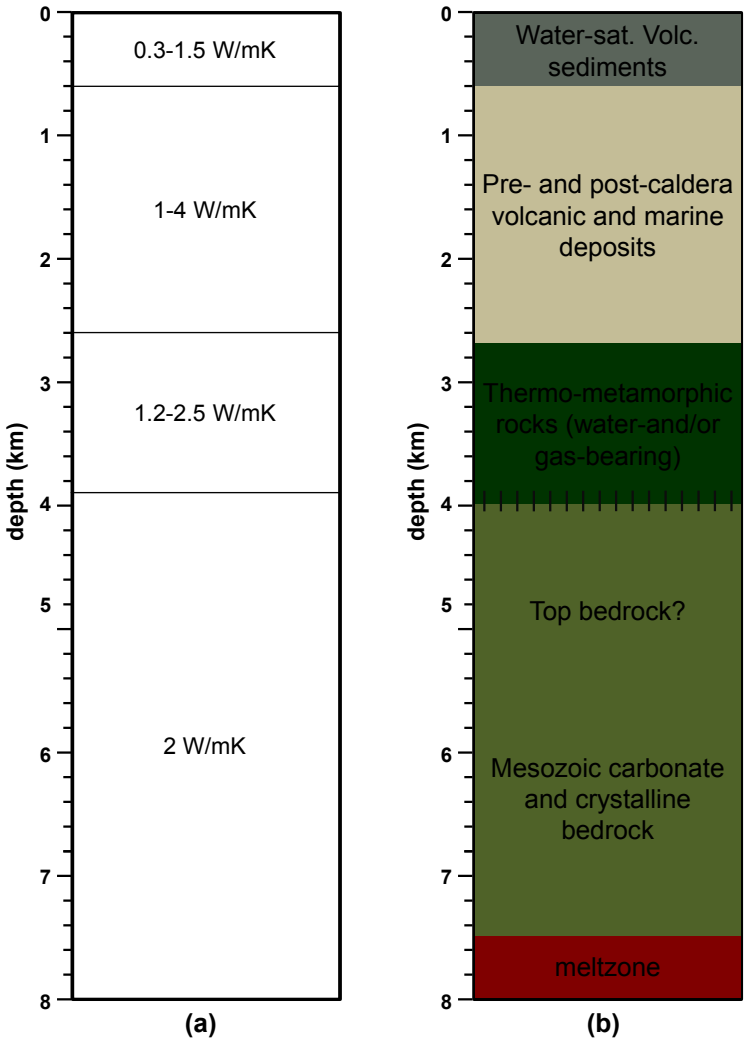

Figure 4.9 (a) Thermal conductivity ranges for 1D modelling (b) Stratigraphic model of the Phlegraean Fields caldera from Zollo et al. [2008].

4.2.2 Model results

First, a 2D numerical simulation was performed by using the developed code (see Chapter 2) to reproduce the results of the conductive model of Wohletz et al. [1999]. In

other words, by using the modeling of the Phlegraean magmatic system, geological constraints and boundary conditions of Woheltz et al. [1999], the implemented numerical algorithm was tested. The magma chamber was assumed with cylindrical shapes of 16 and 10 km diameter, each emplaced instantaneously at 39 and 15 ky, respectively. The top of the magma chamber is located at 3.5 km and the bottom at 8.5 km of depth and its temperature is set at 1000 °C. Numerical simulations were performed with and without the presence of a conduit between 8.5 and 30 km and, since the obtained temperature profiles did not vary significantly, the conduit was not taken into account for next analyses.

Fig. 4.10 shows the comparison between the thermal gradient by Wohletz et al. [1999] and that obtained through the implemented numerical algorithm. The numerical code reproduces quite well the curve obtained by Wohletz et al. [1999]: small differences are of the order of 10 °C and are essentially due to different discretization steps.

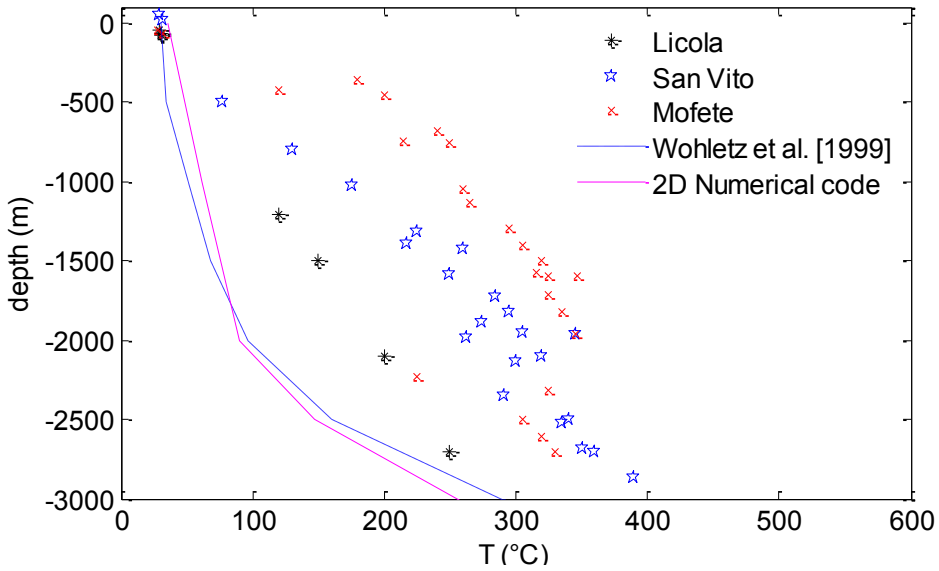

Figure 4.10: Conductive thermal gradients obtained by Wohletz et al. [1999] (blu dashed line) and by the implemented numerical code (magenta solid line) derived from the same geological constraints and boundary conditions. Symbols represent the measured geothermal gradients.

Once the code on the model of Woheltz et al. [1999] was tested, 1D and 2D numerical simulations were performed for finding conductive thermal gradients by using the

detailed characterization of rocks discussed in the previous section. It is noted that the number of nodes of the staggered grid (see Chapter 2) was varied for both 1D and 2D analyses until numerical results did not change significantly.

Fig. 4.11 shows the results of the 1D numerical analysis performed by using the geological constraints discussed in the previous section (thick solid lines) and by using the geological constraints by Woheltz et al. [1999] (dashed lines). As it can be seen, the proposed conductive 1D model is able to reproduce the measured thermal gradients and, in this case, the choice of the parameter values (density, specific heat and themal conductivity) seems to be crucial to reproduce the experimental data.

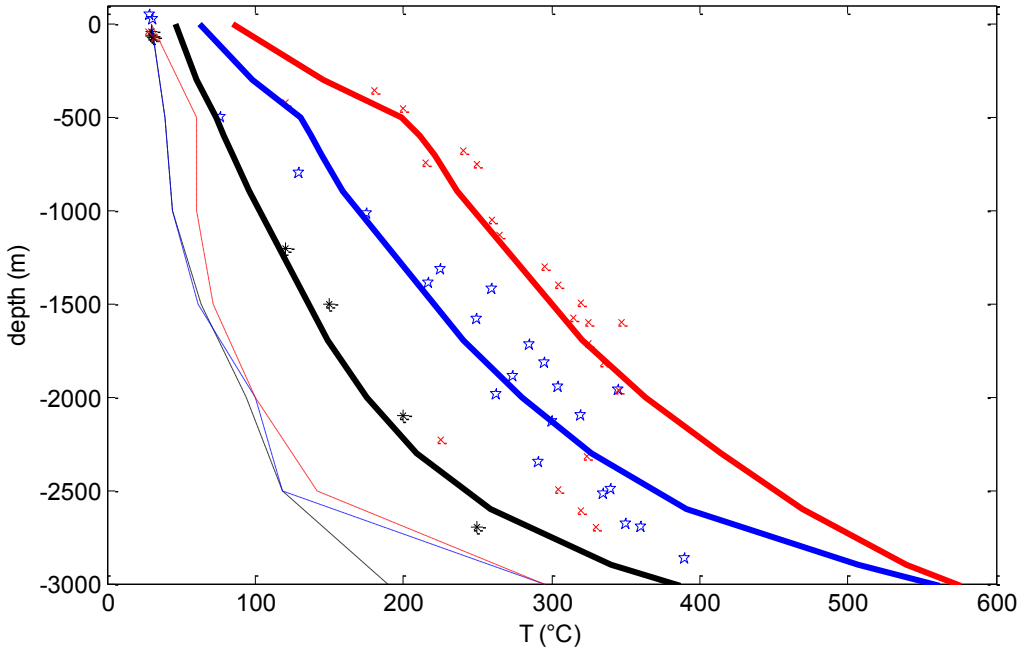

Figure 4.11: 1D conductive thermal gradients obtained by using the geological constraints discussed in the previous section (thick solid lines) and by using the geological constraints by Woheltz et al. [1999] (dashed lines). Symbols represent the measured geothermal gradients.

However, doubts may arise about the appropriateness of the one-dimensional modeling, since in this case heat from magma chamber can propagate in a single direction due to the supposed infinite extension of the reservoir. Thus, a study of 2D modeling was started. Anyway, it is worth mentioning that the one-dimensional approximation gives good results if variations of relevant properties (for instance, thermal conductivity) are

negligible in the other two directions and the source of the thermal anomaly can be considered infinitely extended with respect to the observation point. Finally, for the 1D modeling it is necessary to specify that the synthetic thermal gradient in correspondence of the borehole at Licola (situated outside the caldera rim) has been obtained by considering a thermal source at a constant temperature of 700 ^{o}C, instead of 1000 ^{o}C. This assumption seems to be quite reasonable, if it is considered that this site is situated outside the caldera rim.

For the 2D modeling of the system, the values of the density and the specific heat used for the 1D case were simply homogeneously extended to the 2D grid. Instead, simulations with many different distributions of the *k* values were performed to analyze the dependence of the synthetic thermal gradients on *k* and to obtain the best agreement with the measured thermal gradients.

Fig. 4.12 shows a schematic representation of the grid, where one of the best choices for the distributions of the *k* values is reported. As it can be observed, numerical simulations were performed by using mesh with non-regular steps to optimize computation times.

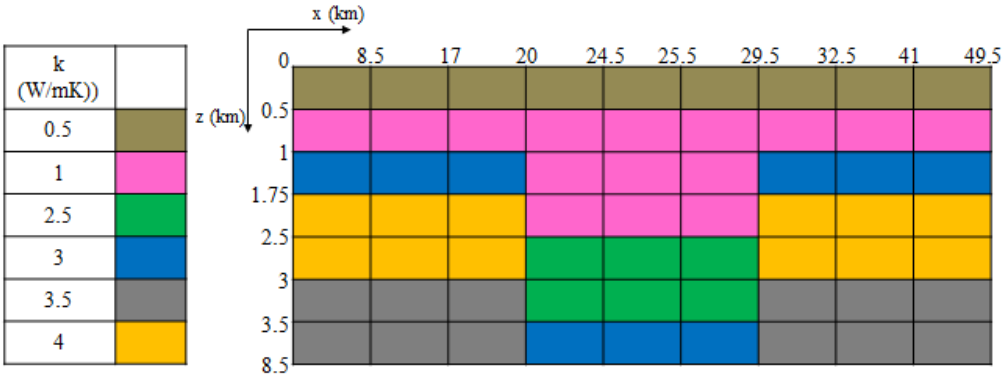

Figure 4.12: Thermal conductivities distribution used for the simulation results shown in Fig. 4.13.

It is noted that for 2D modeling the synthetic thermal gradients are much sensitive to the initial configuration of temperature distribution. In this regard, as discussed in the previous section, two choices were made. In particular, it has been found that if the thermal evolution starts from lithospheric temperatures (thermal gradient of 30 ^{o}C/km)

for all the nodes except for those representing the magma chamber, the obtained synthetic thermal gradients are much lower than those measured (green line in Fig. 4.13, boundary condition case 1), for many different distributions of *k* values. Conversely, if a thermal gradient of 30 °C/km is considered for all nodes except for those at the bottom of the system, for which initial temperatures gradually decrease near the magma chamber and are of about 700 °C, the synthetic curve is able to reproduce the measured thermal gradients below 2500 m (magenta line in Fig. 4.13, boundary condition case 2).

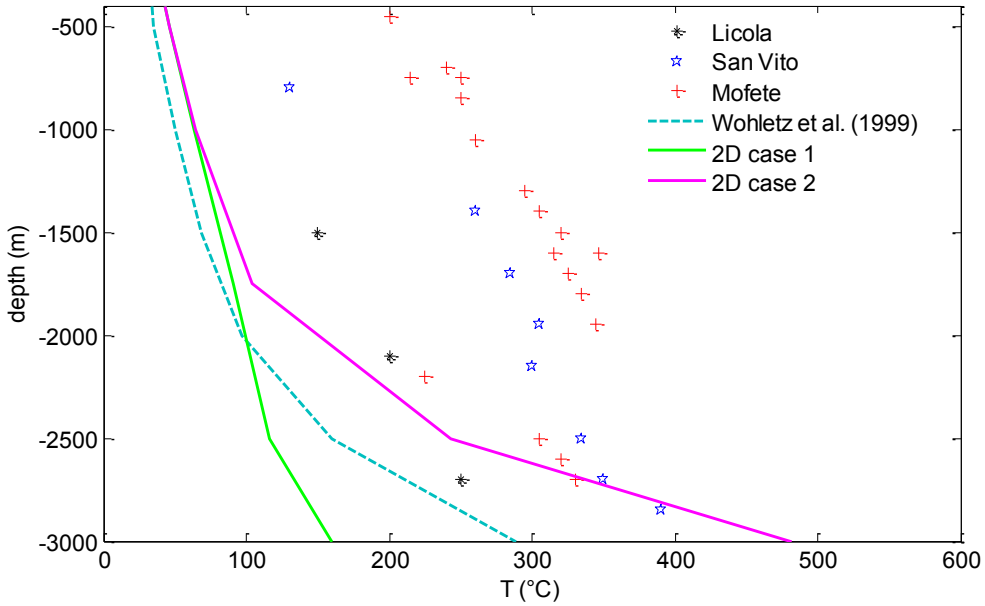

Figure 4.13: 2D conductive synthetic thermal gradient for the node on the top of the grid (i.e. on the surface) corresponding approximatively to the position of San Vito borehole. Dashed line shows the result of the conductive model of Wohletz et al. [1999], green and magenta lines are the synthetic thermal gradients obtained by using boundary conditions of case 1 and case 2, respectively.

A tentative explanation for the initial boundary condition of case 2 is the presence of a highly fractured zone, where hot gases (and/or magma) are trapped and, therefore, can cause an increase of the rock temperature. It is worth noticing that in this case the conductive thermal evolution predicts temperatures of the order of 700 °C at depths of about 3500 m, which could describe the widespread high attenuation zone proposed by

De Siena et al. [2010] on the basis of high-resolution passive seismic tomography (Fig. 4.14).

Finally, so far from the 2D numerical analysis, which is still in progress, it turns out that if conductive heat transfer could maybe explain high thermal gradients below 2500 m, above such a depth hydrothermal convection is certainly a crucial ingredient to appropriately describe heat propagation in the investigated system.

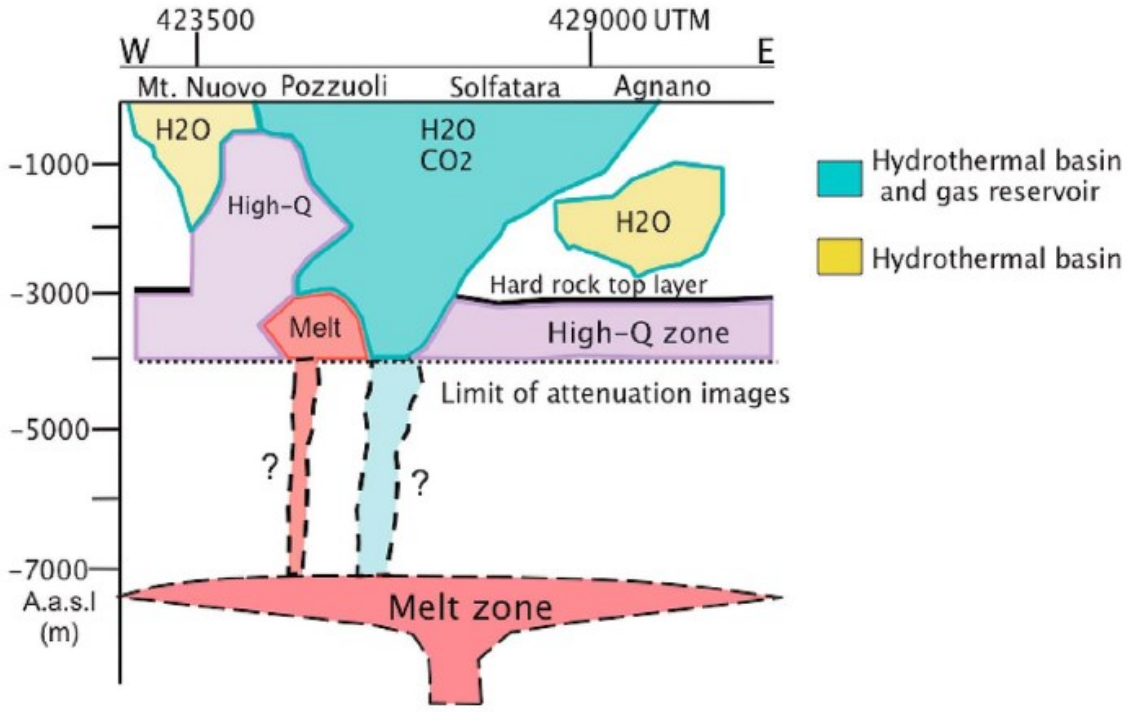

Figure 4.14: Schematic illustration of the uppermost crust crossing the CF district from West to East [from De Siena et al., 2010].

4.3 IRT continuous monitoring analysis

In many cases in volcanic areas temperature variation of fumaroles, open-conduit vents, lava domes and groundwater were followed by eruptions [Spampinato et al., 2011]. Therefore, studying temperature variations can help to understand the volcanic processes [Calvari et al., 1994; Pinkerton and Wilson, 1994; Harris and Maciejewski, 2000; Crisci et al., 2003; Del Negro et al., 2008]. In particular, ground-based thermal image data collection are particularly useful to survey quick processes associated to volcanic

eruptions [Matsushima et al., 2003; Chiodini et al., 2007; Harris et al., 2009; Spampinato et al., 2011], especially in combination with geophysical and geochemical signals. In these cases, the thermal camera can be used to examine spatial and temporal changes in fumarole distribution, temperature and heat flux.

For the monitoring of volcanic areas, the estimation of a global heat flux is attempted to estimate [Pieri and Abrams, 2004]. It is principally valued by estimating the heat flow transported into the soil [Aubert, 1999; Aubert et al., 2008; Peltier et al., 2012] from temperature gradient and soil conductivity measurements [Friedman et al., 1982; Frank, 1985; Aubert, 1999; Aubert et al., 2008]. However, this method does not provide a synoptic view of heat flow variations [Gaudin et al., 2013].

Some authors, instead, are trying to estimate the geothermal flux through measurements of surface temperature anomalies by thermal infrared cameras [Sekioky and Yuhara, 1974; Yuhara et al., 1978, 1981]. Indeed, this temperature excess is related to an additional surface heat flux corresponding to the geothermal flux. The relationship between the temperature anomaly and the excess surface heat flux has been widely studied for quick processes like lava flows, active domes, fumaroles, hot springs [Oppenheimer et al., 1993; Wright et al., 2001; Harris et al., 2004; Bailey et al., 2006].

On the other hand, also detecting and quantifying slow temperatures changes of the shallow thermal structure of quiescent volcanoes over long periods can help to define the level of activity of the volcano [Chiodini et al., 2007; Vilardo et al., 2008]. For this reason, the best method to quantify temperature changes and heat fluxes from thermal imaging data is still searched [Sansivero et al., 2012; Gaudin et al., 2013]. In this section, a new technique to analyze continuous IR image data recording by permanent stations at Campi Flegrei Caldera is described.

4.3.1 TIIMnet stations

The researchers of the National Institute of Geophysics and Volcanology-Vesuvius Observatory (INGV-OV) set up a surveillance network, called Thermal Infrared Imagery Monitoring Network (TIIMNet) to detect and quantify over long-periods slow temperature changes of the shallow thermal structure of quiescent volcanoes [Vilardo et

al., 2008]. The IR stations at Campi Flegrei are located inside the Solfatara crater and at Pisciarelli area (Fig. 4.15) to monitoring the fumaroles [Vilardo et al., 2008]. In fact, when new fluids are ejected by a volcano system, the temperatures of rocks hosting the fumarolic vents, or the size of the fumarolically heated areas, increase [Oppenheimer et al., 1993; Kaneko and Wooster, 1999].

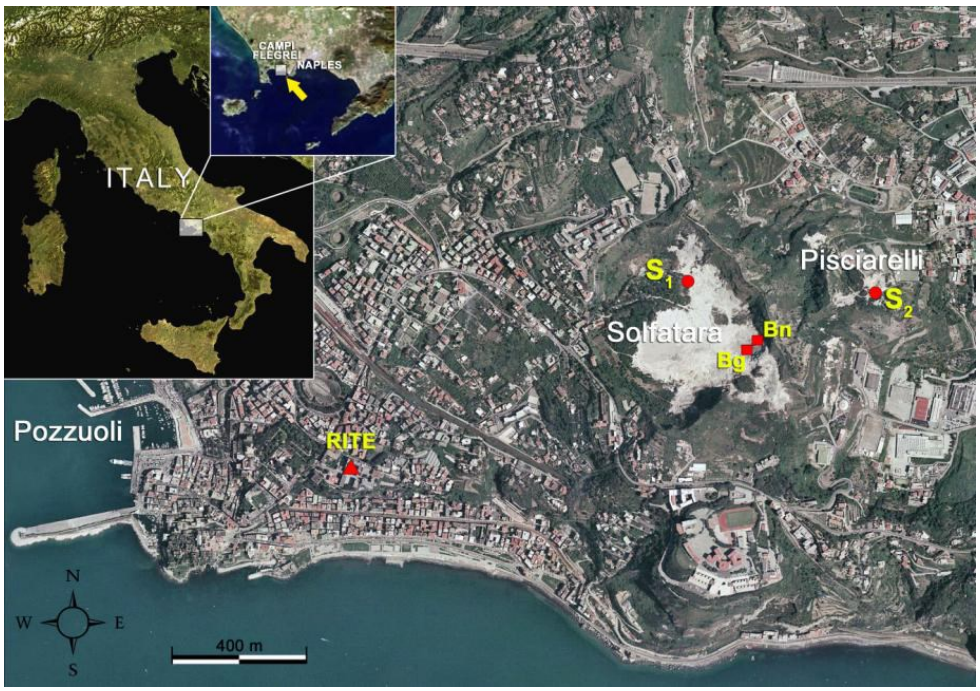

Figure 4.15: Locations of Solfatara (S_1) and Pisciarelli (S_2) IR stations. RITE = GPS station at Rione Terra; Bg = Bocca Grande fumarole; Bn = Bocca Nuova fumarole [from Sansivero et al., 2012].

The IR cameras are the NEC Thermo Tracer TS7302, with focal plane array (FPA) uncooled microbolometer (320x240 pixels) and acquire infrared images at three different times during the night.

At Solfatara, the IR station is operative since July 2004 [Chiodini et al., 2007; Vilardo et al., 2008], and acquires scenes of the SE inner slope of Solfatara caldera at the intersection of two active SW-NE and NW-SE main faults, where the main fumaroles are located at an average distance of about 300 m from the IR camera [Sansivero et al., 2012].

The station at Pisciarelli, operative since October 2006, acquires scenes of the outer eastern flank of the Solfatara tuff-cone (average distance of fumaroles is about 130 m), corresponding to an area characterized by heavy water vapor and CO_2 emissions [Sansivero et al., 2012].

Both IR cameras are inside a protective stainless steel housing, resistant to corrosive elements and with a shooting window of germanium glass, transparent to the thermal wavelengths (Fig. 4.16). The cameras are connected to the Remote Monitoring Stations (RMS), which controls the shooting functionalities of IR sensors and the connection to the surveillance Centre [Chodini et al., 2007; Sansivero et al., 2012].

Figure 4.16: Solfatara thermal monitoring station [from Chiodini et al., 2007].

4.3.2 Temperature changes versus time analysis at Pisciarelli station

The researches of the INGV-OV developed a software to extract information from the time series of the acquired thermal images. In particular, they determine the maximum temperature values of the scene for every acquisition (Fig. 4.17) after a daily and seasonal correction performed in order to remove the effect of environmental parameters (i.e. humidity, air mean temperature and wind speed) and periodicities [Chiodini et al., 2007; Sansivero et al., 2012].

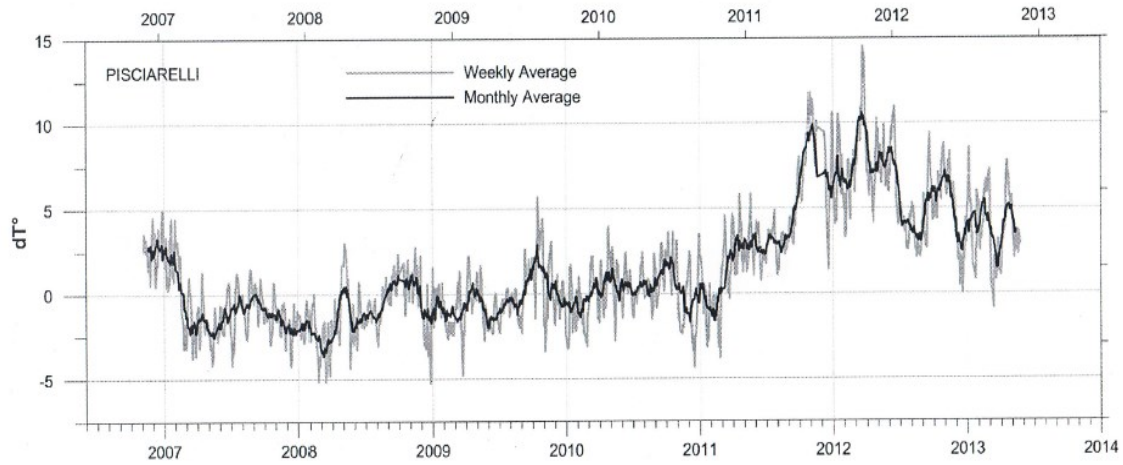

Figure 4.17: Time series of temperature residuals from Pisciarelli station [Vilardo, personal communication].

During the PhD period, a collaboration with the INGV-OV is started in the attempt to develop a comparative analysis to better quantify information from thermal data and possibly find correlations with ground deformation data. To overcome the limit of local information related to the choice to follow only the behaviour over time of the maximum temperature of the scene, an anomaly area, representative of the highest geothermal activity, and a reference area (background) were fixed. After that the temperature changes in time related to the anomaly area are calculated as follows:

$$\Delta T(t) = \left(\sum_{i=1}^{N} T_i^{anomaly}(t) - \sum_{i=1}^{N} T_i^{background}(t) \right) \quad , \tag{4.1}$$

where i is the pixel index and N is the total number of pixels in the selected area.

It is noted that temperature changes in the background area are subtracted to temperature changes in the anomaly area in the attempt to remove periodic components, due to seasonal variations, in order to find some indication of any underlying trend that may be caused by geothermal activity of the anomaly area.

The data consist of thermograms acquired in the night from 31 October 2006 to 22 June 2013 at the Pisciarelli station, which frames the outer eastern flank of the Solfatara tuff-

cone (Fig. 4.18). The thermal images were not acquired every day because environmental or mechanical problems; overall, a series of 2192 data is available.

Figure 4.18: photo of the thermocamera (left) and the Pisciarelli fumarole field (right). The black box indicates a sector of the thermocamera field of view.

The scene of Pisciarelli station (Fig. 4.19) shows two thermal anomalies: the first one, in the lower part on the left, is an enclosure that does not represent an interesting feature, the second one, marked with a black box in Fig. 4.19, is the fumarole field and it represents the analyzed zone of the thermal image.

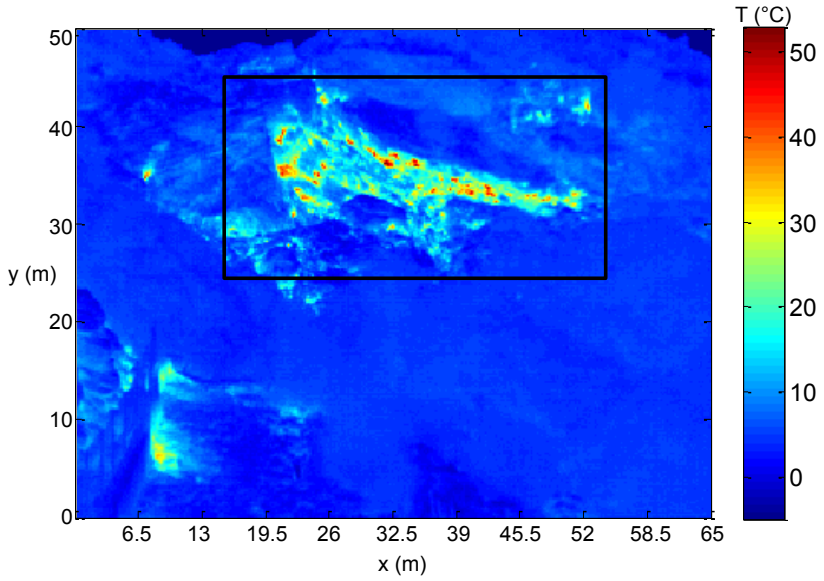

Figure 4.19: Thermal infrared image acquired on 30 October 2006 at Pisciarelli station. The black box indicates the fumarole field.

During the search of the anomaly area that included the highest number of pixels with higher temperature, it was noticed that the whole scene was undergone at a considerable shift of about 22 pixels along the *x* axis first to the west (3 April 2008) and, then, at a shift of about equal size in the opposite direction (27 February 2013) (Fig.4.20) due to the maintenance of the IR camera. Actually, small shifts (2 pixels equal to 0.4 m) along the vertical direction also were registered and they are error sources in data analysis.

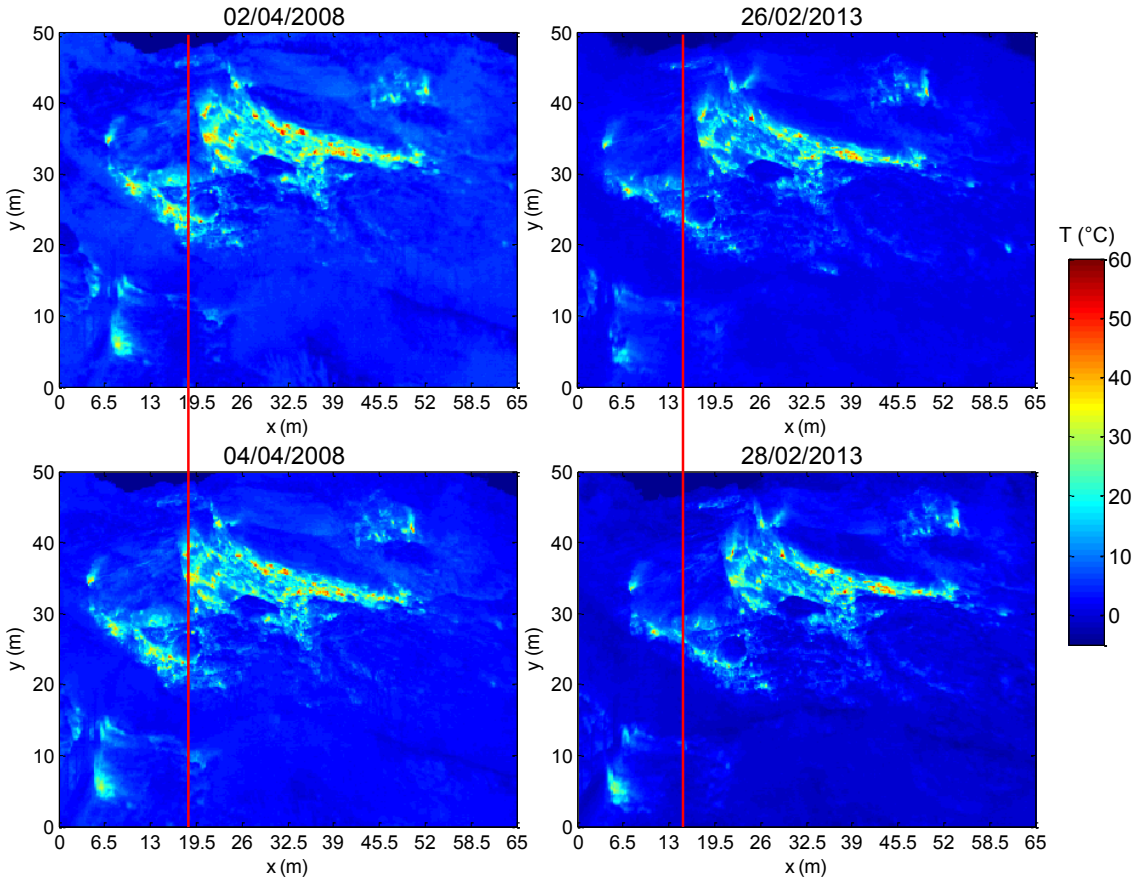

Figure 4.20: Shifts of the IR scene at Pisciarelli station occurred on 3 April 2008 (left) and 27 February 2013 (right).

Once major shifts of the IR images acquired at the Pisciarelli station were corrected, the temperature changes $\Delta T(t)$ were calculated for three backgrounds (black boxes in Fig. 4.21) to verify that $\Delta T(t)$ does not significantly depend on the choice of the background area (Fig 4.22).

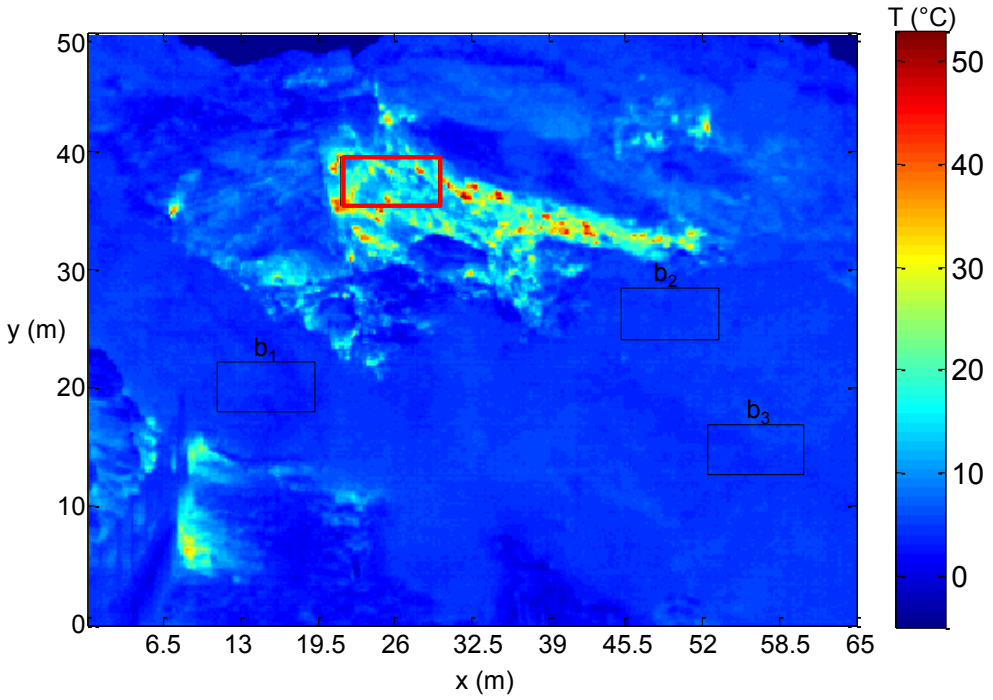

Figure 4.21: Thermal map of the scene of the Pisciarelli station. The red box indicates the considered anomaly area, the black boxes indicate the background areas.

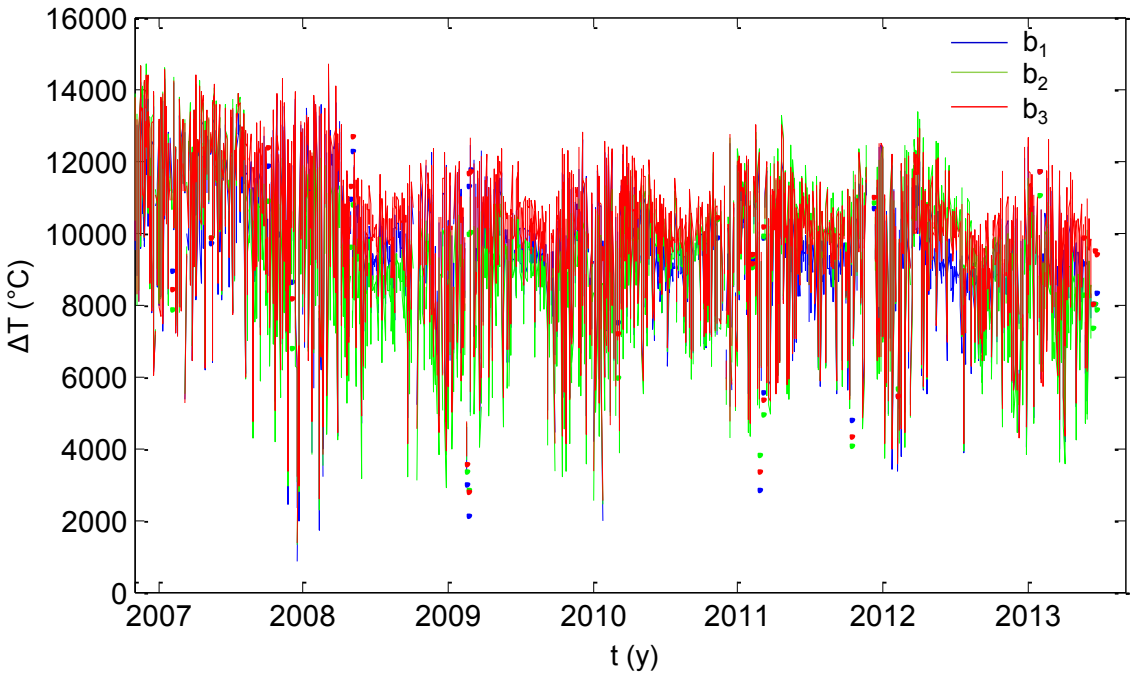

Figure 4.22: Temperature changes obtained by considering the three different background of Fig. 4.21.

After this preliminary analysis, the best anomaly area was searched. Initially, temperature changes, ΔT, were calculated for different single areas (Fig. 4.23): it turns out that the behaviour of ΔT as a function of the time is the same even if the amplitudes of the variations depend on the chosen anomaly area (Fig. 4.24). In particular, the temperature variation patterns shown in Figs. 4.24a and c exhibit a step between the end of 2006 and the first half of 2008, which is missing, or at least much less evident, in Fig. 4.24b. The reason of such differences could be ascribed to errors related to shifts of the images, which are bigger the smaller is the size of the considered anomaly area. However, interestingly, for all three selected anomaly areas (red boxes in Fig. 4.23), a downward trend is apparent during the whole year of acquisition 2012.

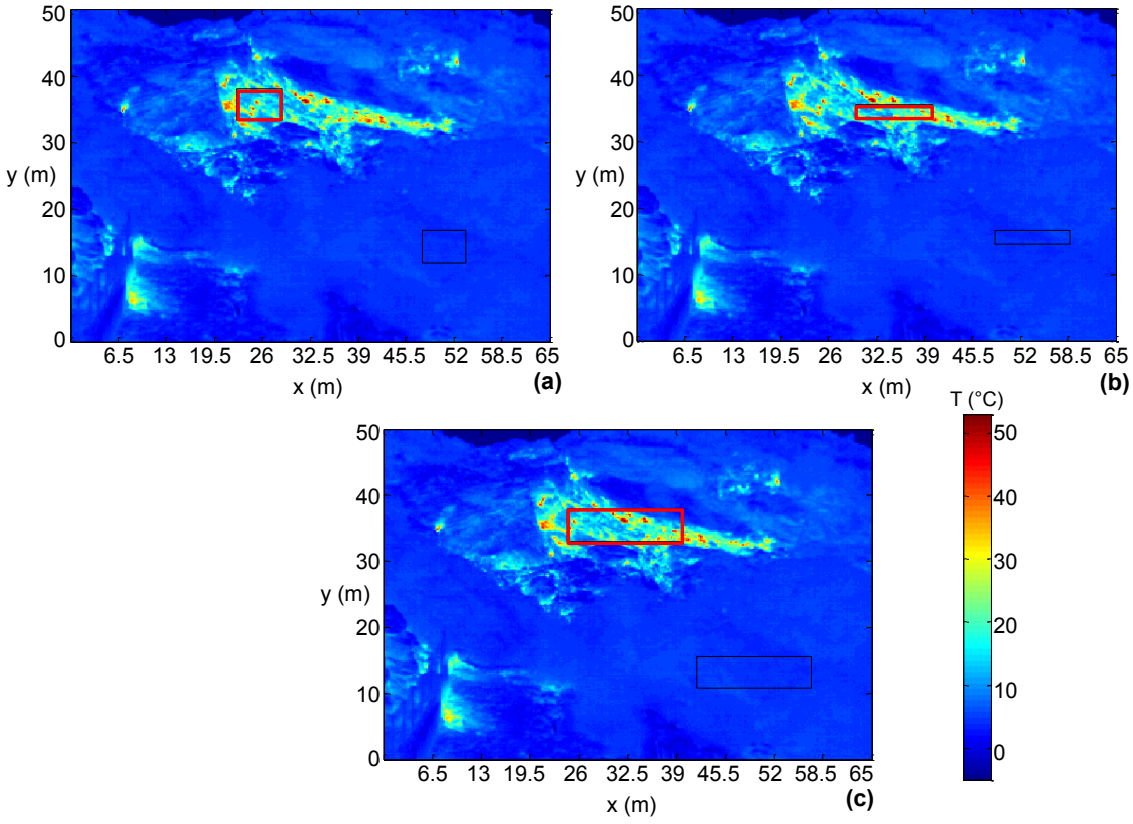

Figure 4.23: Anomaly (red boxes) and background areas (black boxes) chosen for the calculation of the thermal energy changes at Pisciarelli station. The dimentions of the selected areas are 23x25 px (4.7x5.2 m^2) (a), 55x9 px (11.2x19 m^2) (b) and 55x25 px (11.2x5.2 m^2) (c).

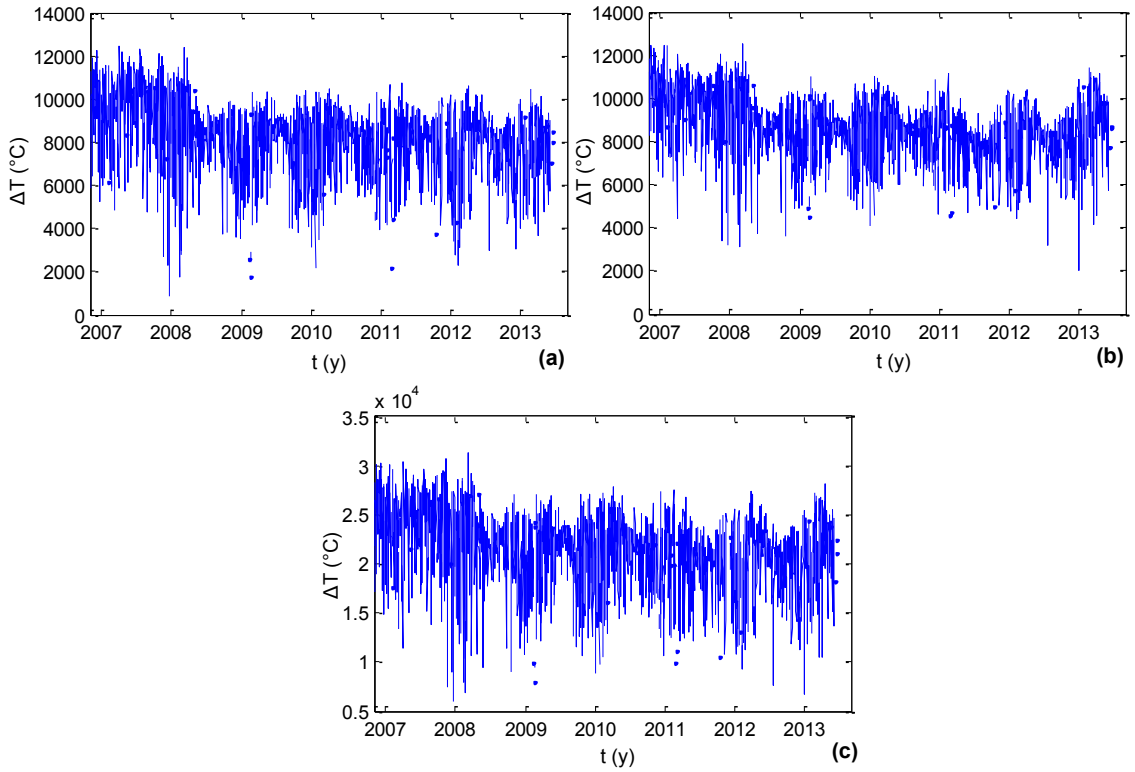

Figure 4.24: Temperature variation vs time for the three thermal anomaly areas shown in Fig 4.23.

In the previously cases, the selected anomaly areas are small and, therefore, the related temporal series $\Delta T(t)$ could be affected by small shifts of the scene due to possible camera movements. In order to take into account the largest anomaly area of Fig. 4.19 excluding cold zones (which are attributed to background), the temperature variations $\Delta T(t)$ were calculated by adding the contribution of five areas (Fig. 4.25). In practise:

$$\Delta T(t) = \sum_{i=1}^{5} \Delta T_i(t) \ , \tag{4.2}$$

where i is the index for the considered area.

Observing the temperature changes over time, $\Delta T(t)$, shown in Fig. 4.26, it is possible recognize a strong sharp downward trend at the end of 2007, an absence of clear trends during from the start of 2009 to the end of 2011, a clear downward trend during the entire year 2012 and a slight rise in 2013.

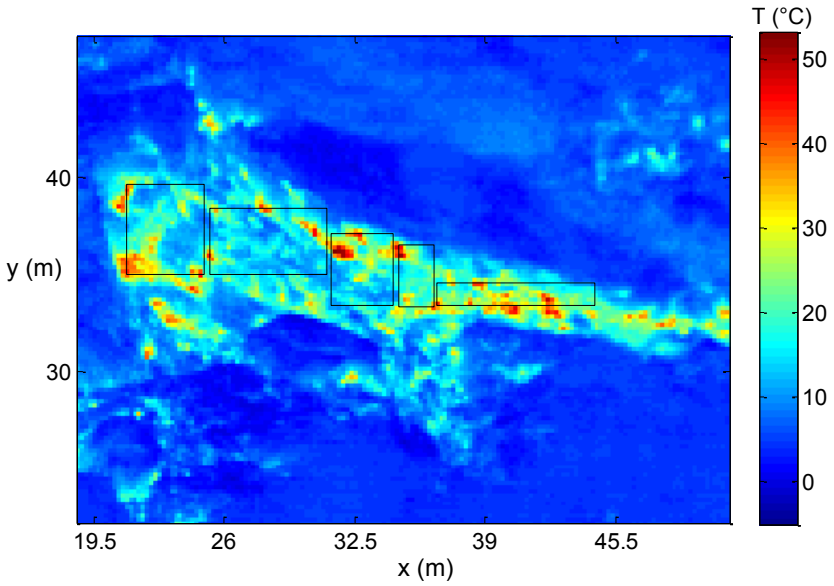

Figure 4.25: Zoom of the scene of Fig. 4.19 that shows the considered five anomaly areas (black boxes).

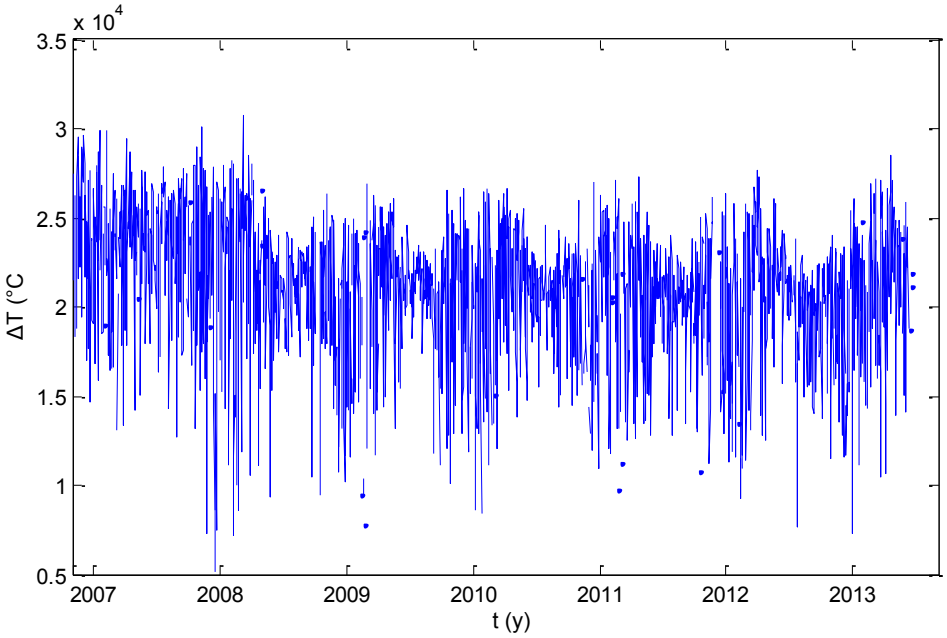

Figure 4.26: Temperature changes obtained by adding the contributions of the five anomaly areas of Fig. 4.25.

Finally, in order to remove noise and periodical components and to highlight temporal trends, two types of smoothing were performed: each group of seven (weekly) or thirty

(monthly) data were replaced with their average (Fig. 4.27) or median (Fig. 4.28). In both cases, downward trends at the end of 2007 and during the entire year 2012, and an upward trend in 2013 are found.

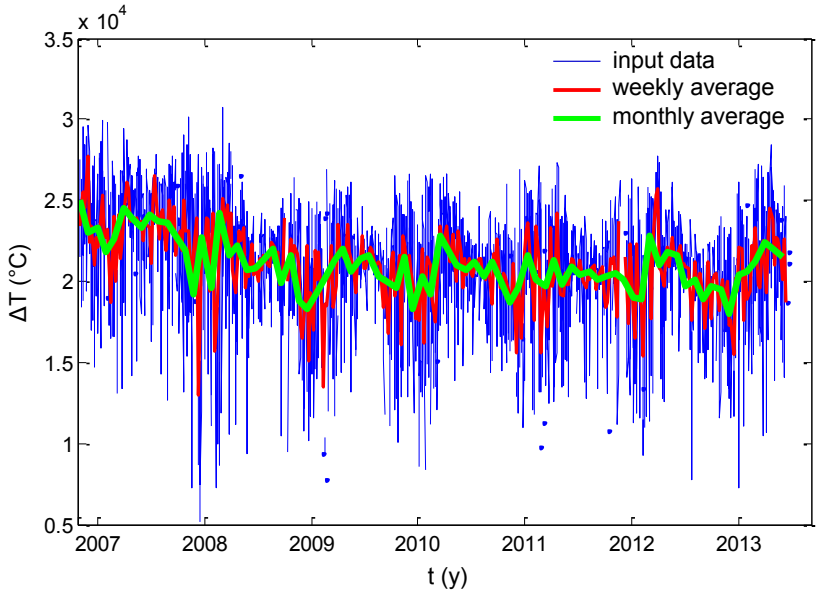

Figure 4.27: Temperatire changes vs time (black line), weekly (red line) and monthly (green line) average of the energy changes.

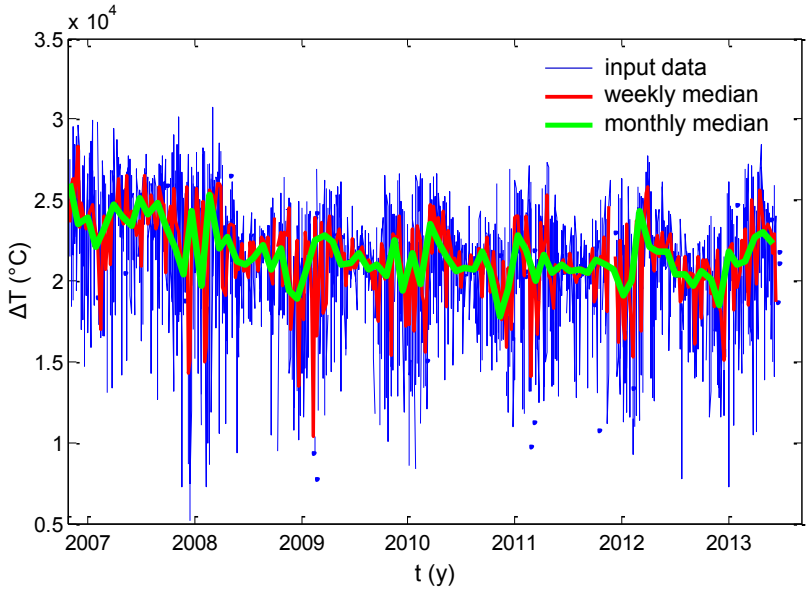

Figure 4.28: Temperature changes vs time (black line), weekly (red line) and monthly (green line) median of the energy changes.

At present, analyses of the temporal series $\Delta T(t)$ and search for possible correlations of our results with those found by Sansivero et al. (2012) and GPS elevation data are work in progress. So far, the study has been focused in more detail over the 2010-2012 period, from which an interesting result is emerged. As shown in Fig. 4.29, which is a zoom of the green curves of Figs. 4.27 and 4.28 for the period 2009-2013 analogous patterns (i.e. an upward trend followed by a downward trend) are repeated at the beginning and at the end of years 2010, 2011 and 2012. However, the amplitude of the visible peaks changes; in particular, the peaks related to the thermal activity of 2012 have full width at half maximum (FWHM) of about 114 days, while the FWHM calculated for the peaks of 2010 and 2011 are of about 53 and 60 days, respectively. Such a feature might be probably related to an injection of fluids, which, in addition to those already present, would cause longer ascent and descent times (almost double).

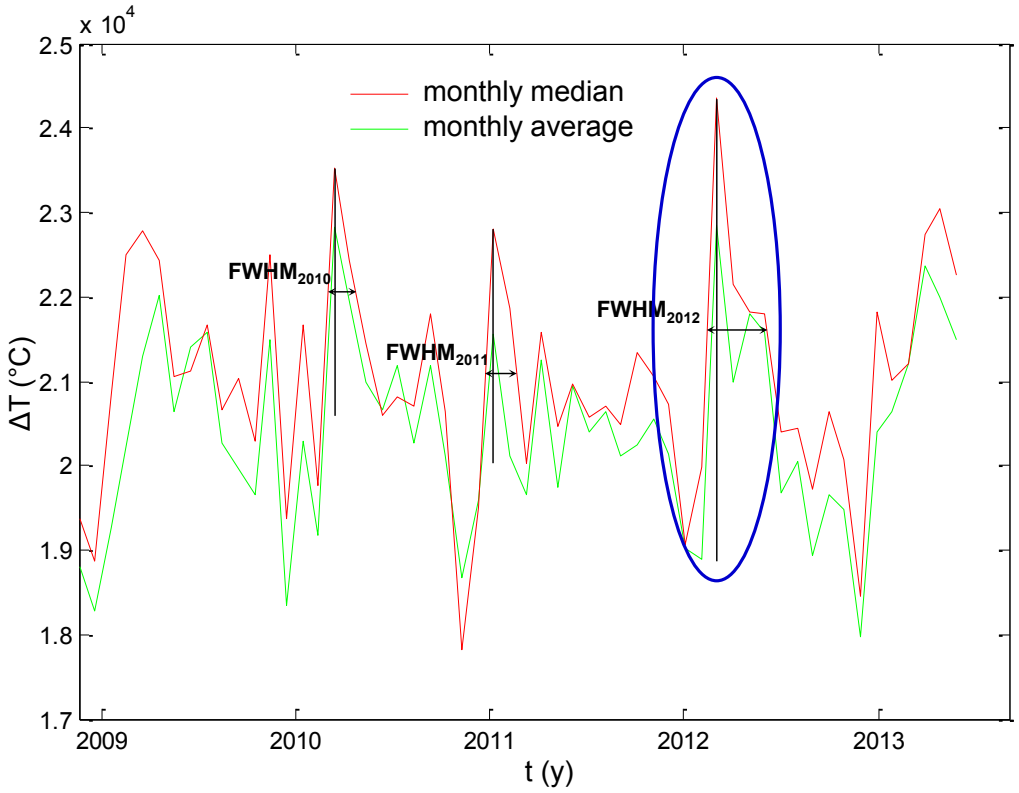

Figure 4.29: Time series of temperature variation for the period 2009-2013.

In order to study the time evolution of the number of pixels with the highest and the lowest temperatures inside the anomaly area, a histogram analysis has been performed (Fig. 4.30). For each year, the histogram is produced by splitting the temperature data of the anomaly area into bins of equal size 2 °C and counting the number of pixels that fall within the bins. This number of pixels has been, , normalized with respect to the total number of pixels of the anomaly area and the number of days of acquisition of the considered period. The histograms show that the distribution tails, which are a measure of the occurrence frequency of the highest temperatures, varies over time: in particular, from 2007 to 2008, the distribution tail decreases from 68 to 62 °C, it remains constant until 2010 and, then, it increases again from 62 to 68 °C from 2010 to 2011. Moreover, in the period 2008-2011 an increase of the pixel fraction at the lowest temperatures is apparent. Such an increase of the low temperature zone inside the anomaly area, which is particularly highlighted in 2011, would explain the reason why the temperature peak at the end of 2011 is absent in the time series in Fig 4.26 while is visible in the time series of Fig. 4.17, which, instead, is constructing by following the maximum temperature of the anomaly area. In 2012, a decrease of the pixels fraction with temperature between 22 and 28 °C is found, which is in agreement with the downward trend of the anomalous temperature (Fig. 4.26). In the first six months of 2013, it is possible to observe an increase of the pixels fractions with temperature between 8-22 °C and an extension of the distribution tail that indicates an increase of the pixels fraction with the highest temperatures, which could justify the slight upward trend evident in the same year.

In Tab. 4.1, values of mode, median and average estimated from the histograms are summarized. As it is shown in the table, the mode and the median of the distributions exhibit similar trends – they first increase, reaching their maximum values in the years 2008 and 2009, and then decrease - whereas the the average remains constant over time.

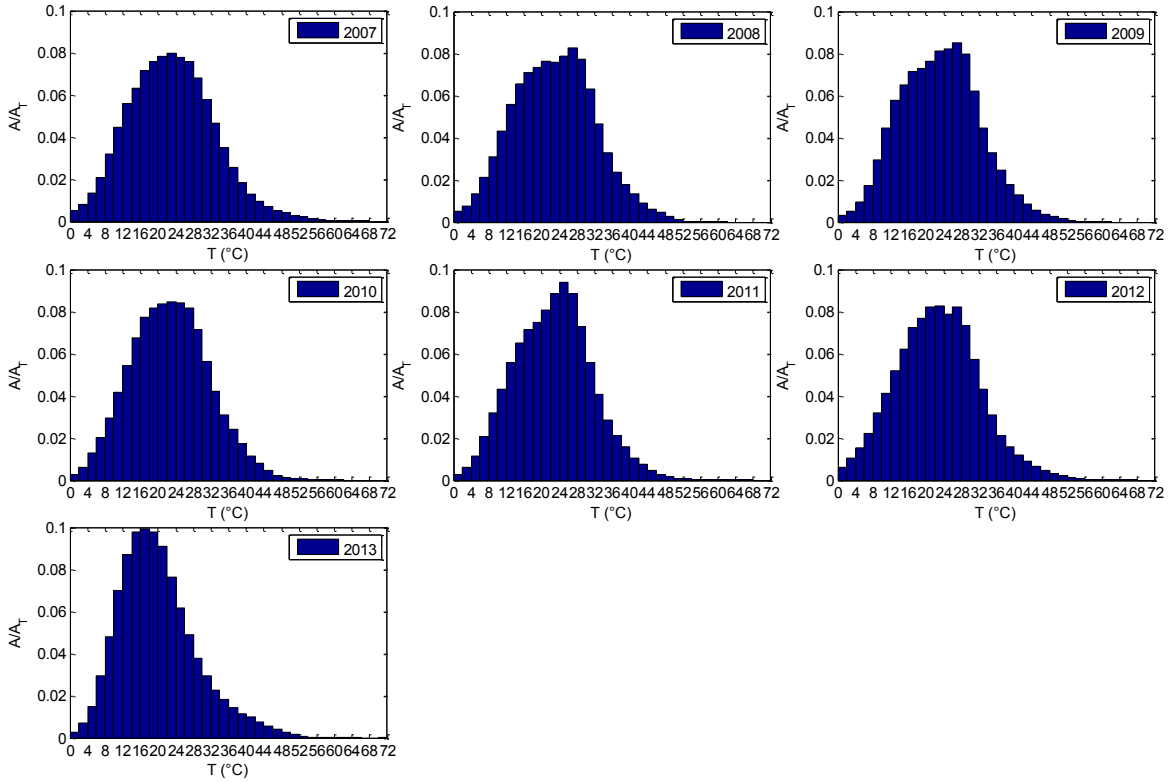

Figure 4.30: Histograms of the pixels distribution in the anomaly area vs temperature.

Table 4.1: Mode, median and average of histograms in Fig. 4.30.

	mode (°C)	**median (°C)**	**average (°C)**
2007	23	21	23
2008	27	23	23
2009	27	23	23
2010	25	21	23
2011	25	21	23
2012	23	21	23

Finally, the heat flux of the anomaly area has been calculated considering the convective component of the thermal flux [Bromley et al., 2011]:

$$Q_c = h_c A(T_a - T_b) \ , \tag{4.1}$$

where h_c=11 W/m^2°C is the convective heat transfer coefficient of air, A is the considered anomaly area (m^2), T_a and T_b are the sum of the temperatures of the anomaly area and the background, respectively.

Interestingly, the convective component of the heat flux shown in Fig. 4.31, which is of the order of ~10 kW, is of the same order of magnitude of the heat flux estimated in other active volcanic areas [Chiodini et al., 2005; Matsushima et al., 2003; Bromley et al., 2011]. For instance, for the Solfatara fumarolic field, Chiodini et al. estimate a heat flux of the order of 100 MW over an area of 620,000 m^2, which is equivalent to a heat flux of the order of 10 kW over an area 9000 time smaller as that considered in this study.

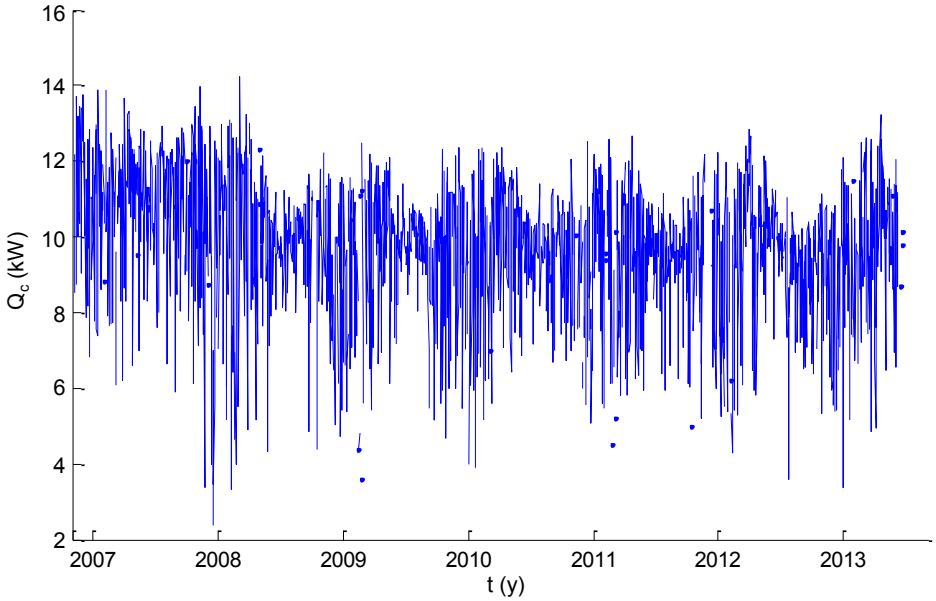

Figure 4.31: Convective heat flux vs time.

Chapter V

Inverting IRT data by Prony's method

Searching for inversion methods of experimental data is a topic of fundamental importance in applied geophysics.

In the case of IRT, the solution of the inverse problem consists in retrieving the size, shape and location of the heat anomaly source by using the measured temperature data. This inverse problem is ill-posed, i.e. the solution is not unique and the inversion is not stable, as arbitrarily small errors in the data can yield arbitrarily large changes in the solution. To overcome the ill-posed character of this problem several inversion procedures have been proposed like neural networks, genetic algorithms and least-squares minimization. Neural networks and genetic algorithms are considered global methods since they search over wide ranges of parameter values, which require many evaluations of the goal function. In contrast, least squares methods are local methods as they start from one set of parameter values and modify them to look for the minimum of the residue. Even if local methods allows finding a more accurate solution and are computationally cheaper than global ones, the latter are more robust in the sense that are designed to avoid trapping in a local minimum, as can be the case with local methods.

Several authors have implemented all these methods to solve ill-posed inverse problems in the field of photothermal NDE methods [Glorieux et al., 1999; Li Voti et al., 2005; Bison et al., 2006; Marcuzzi and Marinetti, 2008; Apiñaniz et al., 2010; Chen and Zhang, 2010; Celorrio et al., 2013].

In this thesis, a new approach is proposed to solve the inverse problem based on the assumption that the thermal decays can be expressed as sum of exponential terms. Actually, others authors have already used independent exponential terms to describe thermal decays but as fit functions [Delplech et al., 1994; Maierhofer et al., 2003; Sun, 2006].

Conversely, the new approach proposed for the inversion of the cooling thermal decays determines the number of the damped exponential terms by the application of the Prony's method. The method, based on Prony's theorem [1795], is a mathematical procedure which can reproduce a temporal decay transient finding its different exponential components and the relative weights. The idea of applying such a method to IRT data arises from a hypothesized correspondence between the time-domain induced polarization (TDIP) transients and the cooling thermal decays. Induced polarization (IP) is a geophysical method used to identify subsurface materials (such as ore), or physical anomalies due to electrochemical phenomena, by analyzing the electrical depolarization transients observed when a steady current injected in the subsurface through two electrodes is shut off. As the Prony's method seems fully describe time-domain IP discharge curves, which relax as sum of decreasing exponentials [Patella et al., 1987; Patella and Di Maio, 1989; Di Maio and Patella, 1990], an application of the method is here proposed for the quantitative interpretation of cooling transients.

In the following sections, a description of the Prony's method and its application to IRT data are presented.

5.1 Prony's method

The Prony's method is an analysis technique for determining the values of parameters of a linear sum of damped complex exponential functions that describe any decay transient obtained from uniformly sampled data [Prony, 1795; Hildebrand, 1974; Marple, 1987].

The Prony's analysis is not only a signal analysis technique but also a system identification method, which is widely used in the areas of power system electromechanical oscillations [Trudnowski et al., 1991; Sanchez-Gasca and Chow, 1999; Xiao et al., 2004], biomedical monitoring [Sava and McDonnell, 1995, 1996], radar [Chuang and Moffat, 1976;Carriere and Moses, 1992], analysis of radiative fluxes in planetary atmospheres [Wiscombe and Evans, 1977], geophysical sensing [Lang et al., 1987].

Prony theorem

A record of evenly spaced (in time) data sequence is assumed to be expressed in the form of superposition of complex damped exponentials, as follow:

$$y(t) = \sum_{m=1}^{N} A_m e^{b_m t} \quad , \tag{5.1}$$

where the coefficients b_m (negative) are the poles in the complex frequency domain, the coefficients A_m the corresponding residues and N is the total number of damped exponential components.

By application of Prony's method, the $2N$ unknowns in Eq. (5.1), i.e. the N poles and the N residues, can be determined from M ($\geq 2N$) data values of $y(t)$ sampled at a constant rate Δt, which can be indicate with:

$$y(t_n) = y[n] \quad ,$$

where $t_n = n\Delta t$ with $n = 0, 1, \dots, M-1$.

Therefore Eq. (5.1) can be rewritten as:

$$y(t_n) = y[n] = \sum_{m=1}^{N} A_m e^{b_m n\Delta t} = \sum_{m=1}^{N} A_m z_m^n \quad . \tag{5.2}$$

When $y(t)$ is a real function, of course the b_m and A_m unknowns must be real or pairs of complex conjugate values.

The procedure is based on the following property. Putting

$$z^N + \alpha_{N-1} z^{N-1} + \alpha_{N-2} z^{N-2} + \cdots + \alpha_1 z + \alpha_0 = 0 \tag{5.3}$$

the algebraic equation, whose roots are the N (complex) numbers $e^{b_m \Delta t}$, the vector α, with components $\alpha_0, \alpha_1, \ldots, \alpha_N = 1$ appearing in equation (5.3), is such that

$$\sum_{p=0}^{N} \alpha_p y_{p+k} = 0 \tag{5.4}$$

for every k integer and $p+k=n=0, 1, \ldots, M-1$. Eq. (5.4) is known as Prony's theorem [Angot, 1958].

In practice, the method computes A_m and b_m in three basic steps [Singh, 2003]:

- **Solve linear prediction model, which is constructed by observed data set.**

First, Eq. (5.2) is written as a linear prediction model:

$$y[n] = \alpha_1 y[n-1] + \alpha_2 y[n-2] + \cdots + \alpha_N y[n-N], \text{ with } n=N, N+1, \ldots, M-1 \text{ .} \tag{5.5}$$

In Eq (5.5), $y[n]$ can be written in matrix form for various values of n as:

$$d = D\alpha \quad , \tag{5.6}$$

where

$$d = \begin{bmatrix} y[N] \\ y[N+1] \\ \vdots \\ y[M-1] \end{bmatrix}, \quad D = \begin{bmatrix} y[N-1] & y[N-2] & \cdots & y[0] \\ y[N] & y[N-1] & \cdots & y[1] \\ \cdots & \cdots & \cdots & \cdots \\ y[M-2] & y[M-3] & \ldots & y[M-N-1] \end{bmatrix} \text{ and } \alpha = \begin{bmatrix} \alpha_1 \\ \alpha_2 \\ \cdots \\ \alpha_N \end{bmatrix} .$$

Assuming $M>2N$, the coefficients vector α can be estimated by solving the over-determined least square problem, which is computed by inverting Eq. (5.6), i.e.

$$\alpha = D/d \text{ .} \tag{5.7}$$

- **Find roots of characteristic polynomial formed the linear prediction coefficients.**

Once the vector α was derived from Eq. (5.7), the roots z_m of the following polynomial equation,

$$\sum_{p=0}^{N} \alpha_p z^p = 0 \quad \text{for } z=z_1, \ldots, z_m \quad \text{and } \alpha_N=1 \text{ ,} \tag{5.8}$$

can be computed [Angot, 1958].

Therefore, the poles b_m can be obtained from the following relationship:

$$b_m = \frac{\ln z_m}{\Delta t} \quad . \tag{5.9}$$

- **Solve the original set of linear equations to yield the coupling coefficients A_i.**

Since the roots z_m are now known, the coefficients A_i can be derived from Eq. (5.2) that in matrix form reads:

$$Y = ZA \quad , \tag{5.10}$$

where

$$Y = \begin{bmatrix} y[0] \\ y[1] \\ \vdots \\ \vdots \\ y[M-1] \end{bmatrix}, \quad Z = \begin{bmatrix} 1 & 1 & \cdots & 1 \\ z_1 & z_2 & \cdots & z_N \\ \cdots & \cdots & \cdots & \cdots \\ z_1^{M-1} & z_2^{M-1} & \cdots & z_N^{M-1} \end{bmatrix} \quad \text{and} \quad A = \begin{bmatrix} \alpha_1 \\ \alpha_2 \\ \cdots \\ \alpha_N \end{bmatrix} \quad .$$

Hence, the Prony's algorithm involves the solution of two systems of linear equations of order *N*, and the solution of an algebraic equation of degree *N*.

The necessary condition to apply the Prony's method is that the system relaxes as sum of decreasing exponentials. Moreover, in order to obtain *N* poles and *N* residues it is necessary to have at least *M=2N* regularly spaced data. Generally, *N* is not a priori known, so a very large number of data (*M*>>2*N*) has to be considered; hence the application of the method provides *M* poles, and *M* corresponding residues, consisting of *N* real poles, and *N* real residues, that describe the signal, and *M-N* complex conjugate values that describe the noise of the measurement.

5.2 Application of Prony's analysis to IRT data

An algorithm which solves the Prony's problem has been implemented. In particular, the developed code requires in input number and values of the experimental data, and gives

in output poles and residues that quantitatively reconstruct the experimental thermal transient.

Firstly, the algorithm has been tested on synthetic curves obtained as damped exponential sums with different numbers of exponential terms and time sampling steps. For all the examined cases, the code provides in output the correct poles and residues, i.e. the coefficients and the exponential terms used to generate the synthetic data.

Afterwards, the Prony's method has been applied to synthetic thermal decay curves. In particular, decay curves from the Newton's law of cooling have been considered. Newton's law of cooling states that the rate of temperature of a homogeneous body is proportional to the temperature difference between the body and its surroundings:

$$\frac{dT}{dt} = -R(T - T_a) \,, \tag{5.11}$$

where R is a positive proportionality constant depending on the properties of the material being cooled and T_a is the environmental temperature which is supposed to be constant. Applying the initial condition $T(t = 0) = T_i$, the solution of Eq. (5.11) reads:

$$T(t) = T_a + (T_i - T_a)e^{-Rt} \,, \tag{5.12}$$

which represents the Newton's law of cooling and states that the temperature of the body approaches the temperature of its surroundings as time goes.

Thermal decay curves were generated by considering different media of different thicknesses as reported in Tab. 5.1, where α_{nom} [m^2/s] and L_{nom} [m] are the nominal thermal diffusivity and the nominal thickness of the media, respectively, and $R_{nom} = \alpha_{nom}/L_{nom}^2$ [1/s]. More in detail, the curves were obtained by considering a cooling time period of 2490 s, a time step of 10 s, and an environmental temperature of 286 K. Eq. (5.12) was normalized with respect to the initial temperature, T_i, and, therefore, becomes,

$$T_N(t) = \frac{T(t)}{T_i} \,. \tag{5.13}$$

Table 5.1: Thermal diffusivity, α_{nom}, thickness, L_{nom}, and cooling constant, R_{norm}, used to generate the cooling thermal curves.

material	α_{nom} [m/s^2]	L_{nom} [m]	R_{nom} [1/s]
cement	$7.60\text{x}10^{-7}$	0.01	$7.60\text{x}10^{-3}$
		0.10	$7.60\text{x}10^{-5}$
		1.00	$7.60\text{x}10^{-7}$
tuff	$4.40\text{x}10^{-7}$	0.01	$4.40\text{x}10^{-3}$
		0.10	$4.40\text{x}10^{-5}$
		1.00	$4.40\text{x}10^{-7}$
plexiglass	$1.10\text{x}10^{-7}$	0.01	$1.10\text{x}10^{-3}$
		0.10	$1.10\text{x}10^{-5}$
		1.00	$1.10\text{x}10^{-7}$

The Prony's method was applied to each curve corresponding to the nine cases of Tab. 5.1; Tab. 5.2 summarizes the values obtained for the poles (b) and the corresponding residues (A) provided by the Prony's analysis. It is interesting to note that in all cases the Prony's method determines two real exponentials: the first one, indicated by the coefficients A_1 and b_1 in Tab. 5.2, represents the term at zero frequency ($b_1 \sim 0$), i.e. the asymptotic value of the cooling transient [T_a in Eq. (5.12)], the second exponential, indicated by the coefficients A_2 and b_2, returns the parameters most likely related to the test material. Indeed, the values of the pole b_2 exactly match the cooling constants (R_{nom}) of the considered media.

These results seem to indicate that in the case of homogeneous media, the Prony's analysis should yield two real exponential terms, respectively related to the characteristic parameters of the medium and to the environment temperature value.

As example, Fig. 5.1 shows how the curve, reconstructed as sum of the two retrieved exponential terms, perfectly overlaps the theoretical curve, also when the number of data does not allow appreciating the asymptotic part of the curve (Fig. 5.1c).

Table 5.2: Results obtained from the application of the Prony's method to normalized thermal transients from Newton's law of cooling.

material	A_1 **[K]**	b_1 **[1/s]**	A_2 **[K]**	b_2 **[1/s]**
cement	0.98	-4.13×10^{-15}	1.72×10^{-2}	7.60×10^{-3}
	0.98	-2.14×10^{-13}	2.05×10^{-2}	7.60×10^{-5}
	0.97	-2.70×10^{-11}	2.56×10^{-2}	7.60×10^{-7}
tuff	0.98	-1.79×10^{-14}	1.55×10^{-2}	4.40×10^{-3}
	0.97	-1.85×10^{-12}	2.72×10^{-2}	4.40×10^{-5}
	0.97	-2.52×10^{-11}	2.89×10^{-2}	4.40×10^{-7}
plexiglass	0.98	-2.87×10^{-14}	1.89×10^{-2}	1.10×10^{-3}
	0.98	-2.22×10^{-12}	2.39×10^{-2}	1.10×10^{-5}
	0.97	-1.67×10^{-11}	2.75×10^{-2}	1.10×10^{-7}

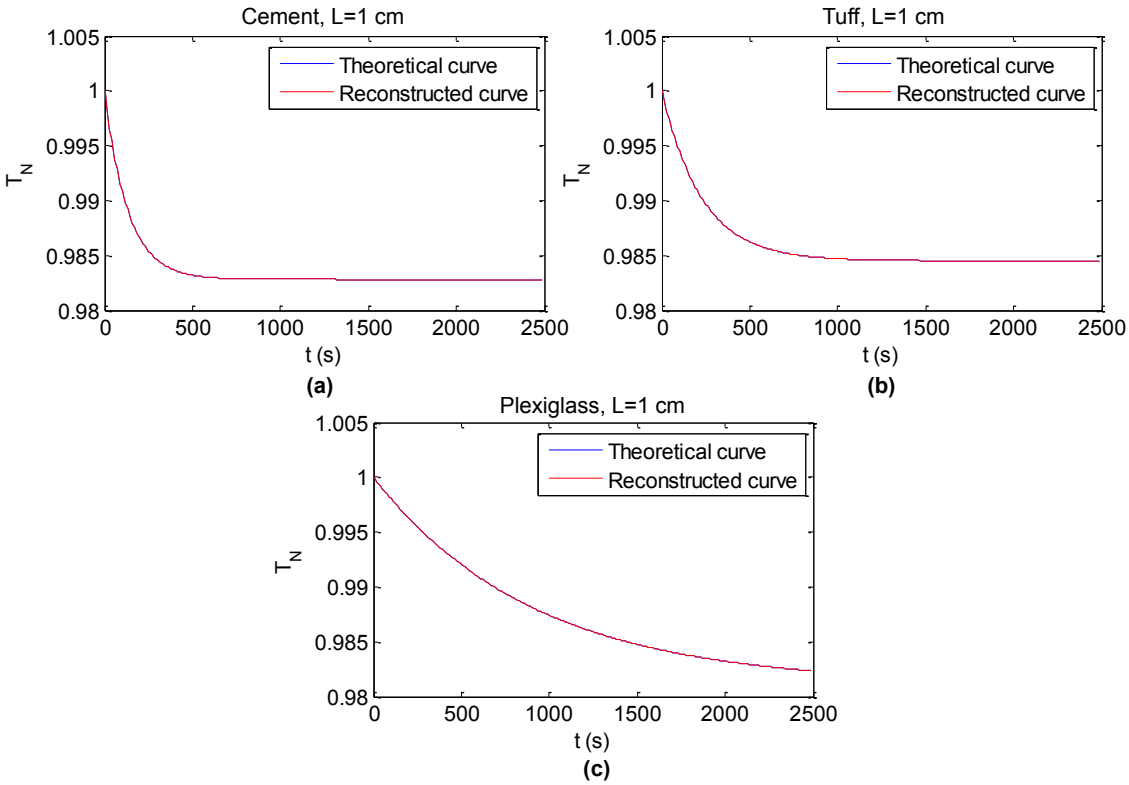

Figure 5.1: Comparison between the theoretical curve and the reconstructed curve by using the Prony's method in the case of an ideal 1cm thick sample made of cement (a), tuff (b) and plexiglass (c).

After testing the effectiveness of the Prony's method on synthetic thermal data, experimental IRT data, coming from laboratory surveys, were analyzed (see Chapter 3). First, data from sound zones of the laboratory specimen I, were considered. In particular, the thermal transient of five surface pixels located on sound zones of the specimen, i.e. non corresponding to in-depth defect occurrence, were considered (Fig. 5.2).

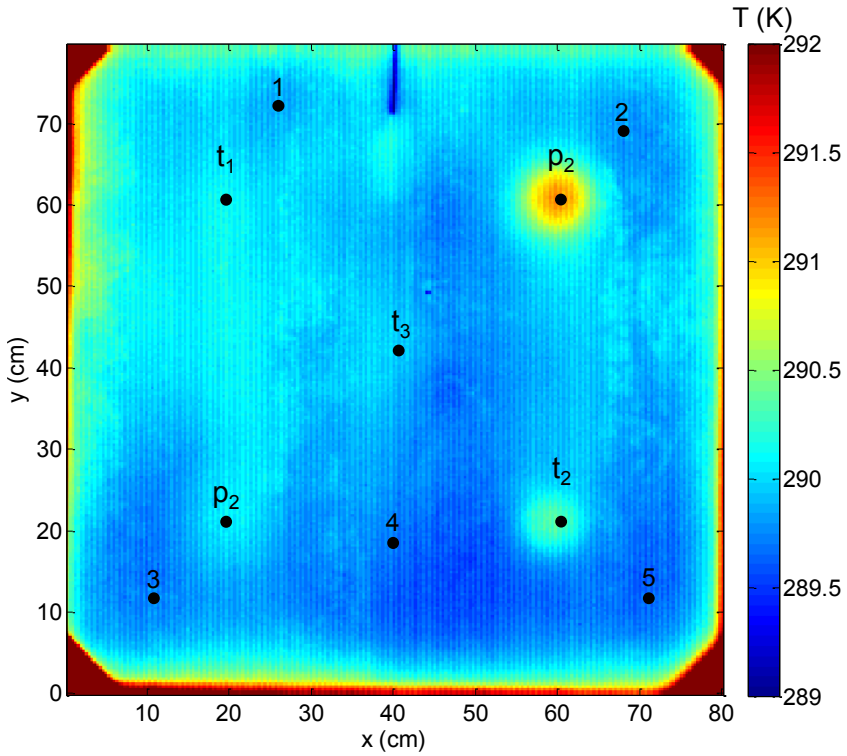

Figure 5.2: A thermogram of the specimen I showing the position of the defects and the five sound pixels considered for the Prony's analysis.

In this case, on the basis of the previous study, two exponential terms were expected from the Prony's analysis, since the specimen is made of a single layer of cement. However, the obtained results have provided both two and three exponential terms, as reported in Tab. 5.3. The different number of exponential terms might be probably ascribed to a non-homogeneous heating and/or to noise factors, such as high porosity of the cement and/or presence of the sample lodging support; the synthetic analysis, of course, did not take into account these factors.

Table 5.3: Results of the Prony's analysis on the experimental thermal transients relative to the five pixels shown in Fig. 5.2.

Pixel number	A_1 **[K]**	b_1 **[1/s]**	A_2 **[K]**	b_2 **[1/s]**	A_3 **[K]**	b_3 **[1/s]**
1	289.6	-8.2×10^{-7}	1.8	-1.9×10^{-3}	0.9	-2.1×10^{-2}
2	289.4	-5.5×10^{-7}	1.7	-1.7×10^{-3}	1.0	-1.6×10^{-2}
3	289.5	-1.0×10^{-6}	1.9	-2.0×10^{-3}	-	-
4	289.5	-9.3×10^{-7}	1.7	-1.9×10^{-3}	-	-
5	289.4	-8.9×10^{-7}	1.7	-1.8×10^{-3}	-	-

Anyway, it is worth noting that the maximum value of the experimental curves,

$$T_{rec}(t=0) = \sum_{i=1}^{N} A_i e^{b_i t} \quad \text{with } N=2 \text{ or } 3 \ , \tag{5.14}$$

can be reconstructed more accurately in the case of three exponential terms (Tab. 5.4). This evidence is better highlighted by the overlap of the experimental and reconstructed curves shown in Fig.5.3.

Table 5.4: Experimental, $T_{exp}(t=0)$, and reconstructed, $T_{rec}(t=0)$, maximum temperature values and their difference, Δ.

Pixel number	T_{exp} **(**t**=0) [K]**	T_{rec} **(**t**=0) [K]**	Δ **[K]**
1	292.3	292.3	0.0
2	292.3	292.1	0.2
3	292.3	291.3	1.0
4	292.1	291.2	0.9
5	292.0	291.0	1.0

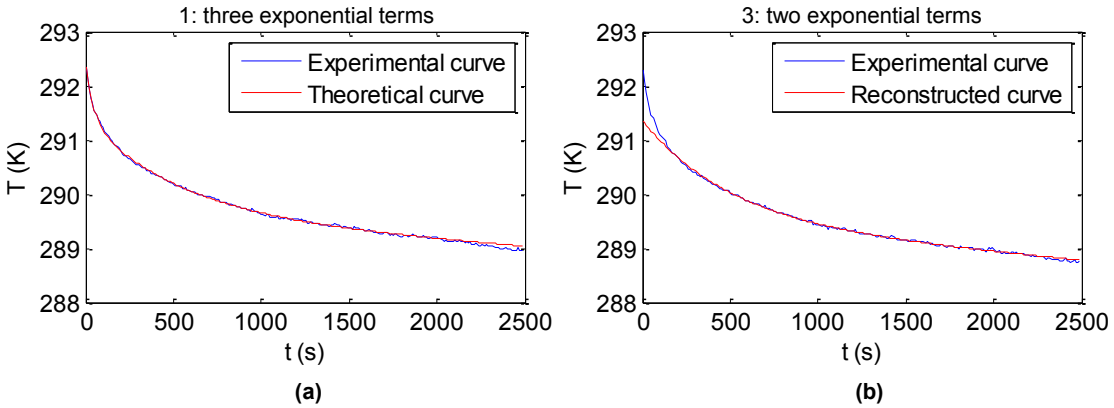

Figure 5.3: Comparison between the experimental curve of the sound pixel 1 (a) and 3 (b) of Fig. 5.2 and the reconstructed theoretical curve by using the Prony's method.

Thus, the Prony's method is able to reproduce with a high degree of accuracy a thermal decay transient by finding the exponential components and the relative weights. However, assuming that the exponential term at zero frequency corresponds to the environmental temperature, the identification of suitable relationships between the others exponential components and the characteristics (i.e., nature, thickness) of the investigated media is not easy to perform. In this case, the simple relationship found for the case of Newton's law of cooling (Tab. 5.2),

$$R = \frac{\alpha}{L^2} = -b \tag{5.15}$$

does not work. Indeed, by considering α=7.6x10^{-7} for the cement and assuming that heat reached a depth of about 0.07 m, it turns out that R is of the order of 10^{-4}, which is smaller than the values of the poles (actually, if L=0.02 m, R=1.9x10^{-3} 1/s). Furthermore, for the case of pixels 1 and 2, the presence of the third exponential term is not easy to interpret.

The problem is even more complicated if non homogeneous zones are considered. Indeed, as concerns the defected zones, the results have provided three exponential terms except in one case in which they are four (Tab. 5.5). It is noted that, actually, on the basis of the synthetic study, three exponential terms were effectively expected from the Prony's analysis but the first term is not at zero frequency, in fact the corresponding

coefficient is higher than the environmental temperature (T_{env}=287 K). The Prony's method does not find the asymptotic term probably because the data set is small; indeed the experimental curves, acquired for 2500 s, do not show the reaching of a thermal equilibrium. It is worth noting that, despite the asymptotic term is not returned, the reconstructed curves well overlap the experimental ones (Fig. 5.4).

Table 5.5: Results of the Prony's analysis on the experimental thermal transients relative to the defects of Specimen I shown in Fig. 5.2.

Defect	A_1 **[K]**	b_1 **[1/s]**	A_2 **[K]**	b_2 **[1/s]**	A_3 **[K]**	b_3 **[1/s]**	A_4 **[K]**	b_4 **[1/s]**
p_1	289.8	$-9.6\text{x}10^{-7}$	2.1	$-1.9\text{x}10^{-3}$	1.5	$-2.1\text{x}10^{-2}$	-	-
p_2	290.1	$-1.4\text{x}10^{-6}$	2.9	$-1.2\text{x}10^{-3}$	1.2	$-2.8\text{x}10^{-2}$	-	-
t_1	289.8	$-1.0\text{x}10^{-6}$	2.0	$-2.0\text{x}10^{-3}$	1.0	$-1.3\text{x}10^{-2}$	0.6	$-1.4\text{x}10^{-1}$
t_2	289.6	$-1.2\text{x}10^{-6}$	2.5	$-1.4\text{x}10^{-3}$	0.6	$-1.9\text{x}10^{-2}$	-	-
t_3	289.6	$-9.3\text{x}10^{-6}$	2.0	$-1.8\ \text{x}10^{-3}$	1.1	$-1.8\text{x}10^{-2}$	-	-

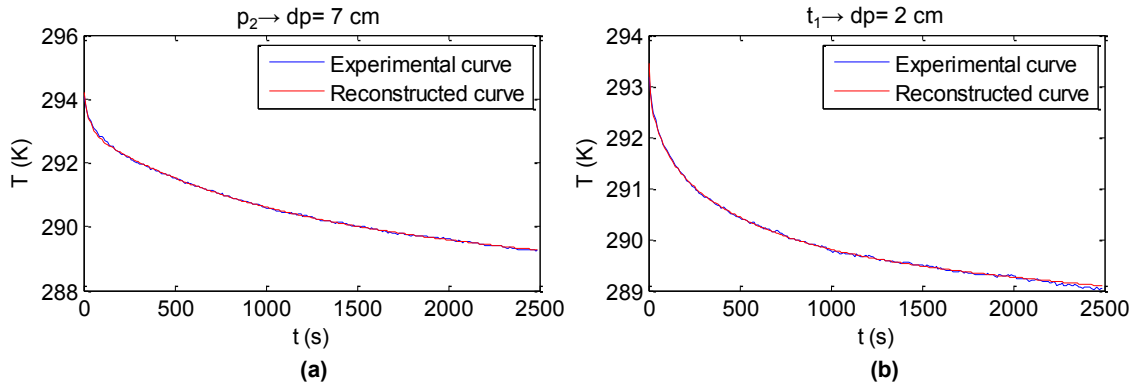

Figure 5.4: Comparison between the experimental curve of defect p_2 (a) and t_1 (b) of Fig. 5.2 and the reconstructed theoretical curve by using the Prony's method (dp=depth of the top of the defect).

As concern the research of the relationships between the exponential terms and the characteristics of the media, it is not possible to hypothesize that different exponential terms are related with different materials because thermal diffusivities of materials are of the same order of magnitude (Tab. 5.1) and the known geometrical properties,

summarized in Tab. 5.6, can not explain the variation of the order of magnitude in the exponential terms (Tab. 5.5).

Table 5.6: Nominal diameter, thickness and depth of the plastic (p_1, p_2) and tuff (t_1, t_2, t_3) defects of the specimen I in Fig. 5.2.

Defect	Diameter (cm)	Thickness (cm)	Depth (cm)
p_1	7	3	7
p_2	7	3	2
t_1	7	3	7
t_2	7	3	2
t_3	10	3	12

Moreover, in the case of defects of specimen I the maximum value of the experimental curves, calculated considering N=3 or 4 in Eq. (5.14), can be accurately obtained (Tab. 5.7).

Table 5.7: Experimental, $T_{exp}(t=0)$, and reconstructed, $T_{rec}(t=0)$, maximum temperature values and their difference, Δ, for the defects of Fig. 5.2.

Defect	T_{exp} (t=0) [K]	T_{rec} (t=0) [K]	Δ [K]
p_1	293.2	292.4	0.1
p_2	294.1	292.4	0.1
t_1	293.2	293.5	0.3
t_2	292.8	292.7	0.1
t_3	292.8	292.7	0.1

The Prony's method was also applied to the data provided by the investigation on the specimen II (Fig. 5.5). As previously mentioned (see Chapter 3), this specimen is made of a double layer of plaster and marble with defects of plastic and cork; it is divided in two parts, side A, with plaster layer 1 cm thick, and side B, with plaster layer 2 cm thick (Tab. 5.8). For more details see Chapter 3.

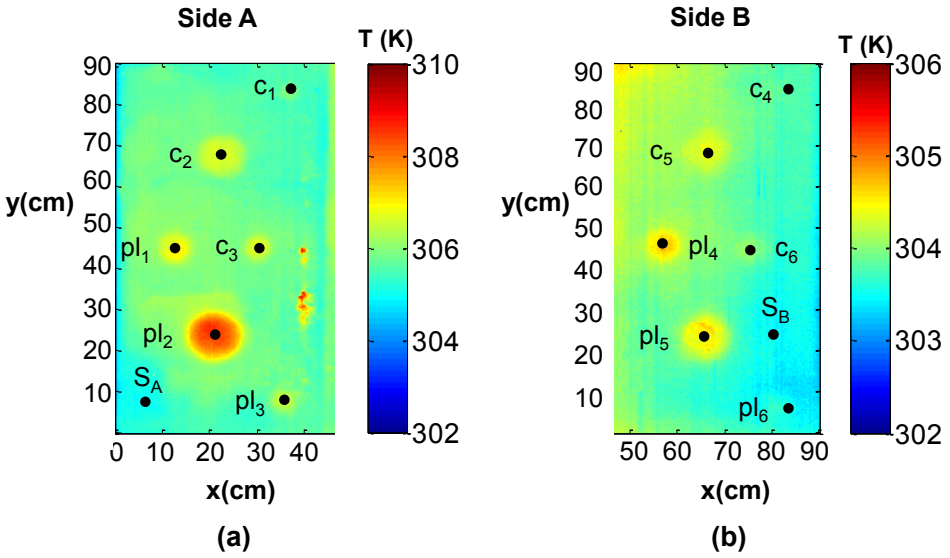

Figure 5.5: Thermograms of the two side of specimen II showing the position of the defects considered for the Prony's analysis.

Table 5.8: Nominal diameter, thickness and depth of the cork ($c_1 \div c_6$) and plastic ($pl_1 \div pl_6$) defects of the specimen II of Fig. 5.5.

Defect Side A	Diameter (cm)	Thickness (cm)	Depth (cm)	Defect Side B	Diameter (cm)	Thickness (cm)	Depth (cm)
c_1	4	0.15	0.85	c_4	4	0.15	1.85
c_2	10	0.15	0.85	c_5	10	0.15	1.85
c_3	6	0.15	0.85	c_6	6	0.15	1.85
pl_1	6	0.20	0.80	pl_4	6	0.20	1.80
pl_2	10	0.20	0.80	pl_5	10	0.20	1.80
pl_3	4	0.20	0.80	pl_6	4	0.20	1.80

The application of the Prony's method have provided two exponential terms for surface pixels located on sound area, on plastic defects on side A and on all defects on side B, whereas three exponential terms were provided for surface pixels located on the cork defects on side A (Tab. 5.9 and 5.10). The difference in the number of exponential terms could be ascribed to the presence of air in the cork defects. The effect of air would be appreciable only on side A being the defect depth double on side B. However, the

negative coefficient A_3 of defects c_1 and c_2 (see Tab. 5.9) are not easy to interpret. Moreover, for the smallest defects on side B (i.e. c_4 and pl_6 in Fig. 5.5b), which are not shown in Tab. 5.10, the analysis provided only one exponential term of the order of 10^{-6}. This is probably due to the position of the defects that are too close to the edges.

Table 5.9: Results of the Prony's analysis on the experimental thermal transients relative to the side A of specimen II shown in Fig. 5.5a.

Side A	A_1 **[K]**	b_1 **[1/s]**	A_2 **[K]**	b_2 **[1/s]**	A_3 **[K]**	b_3 **[1/s]**
sound	304.1	$-1.2\text{x}10^{-6}$	1.9	$-2.1\text{x}10^{-3}$	-	-
pl_1	304.2	$-1.3\text{x}10^{-6}$	3.8	$-2.3\text{x}10^{-3}$	-	-
pl_2	303.8	$-1.0\text{x}10^{-6}$	6.5	$-2.1\text{x}10^{-3}$	-	-
pl_3	303.8	$-1.2\text{x}10^{-6}$	3.7	$-2.2\text{x}10^{-3}$	-	-
c_1	304.3	$-1.4\text{x}10^{-6}$	2.0	$-2.3\text{x}10^{-3}$	-2.2	$-1.7\text{x}10^{-2}$
c_2	304.3	$-1.3\text{x}10^{-6}$	4.1	$-2.6\text{x}10^{-3}$	-1.6	$-5.2\text{x}10^{-3}$
c_3	304.3	$-1.4\text{x}10^{-6}$	2.5	$-2.2\ \text{x}10^{-3}$	1.8	$-7.9\text{x}10^{-3}$

Table 5.10: Results of the Prony's analysis on the experimental thermal transients relative to the side B of specimen II shown in Fig. 5.5b.

Side B	A_1 **[K]**	b_1 **[1/s]**	A_2 **[K]**	b_2 **[1/s]**
sound	303.9	$-1.0\text{x}10^{-6}$	3.1	$-2.8\text{x}10^{-3}$
pl_4	303.5	$-6.3\text{x}10^{-7}$	4.2	$-1.5\text{x}10^{-3}$
pl_5	303.3	$-6.9\text{x}10^{-7}$	4.0	$-1.5\text{x}10^{-3}$
c_5	303.6	$-7.6\text{x}10^{-7}$	3.4	$-1.7\text{x}10^{-3}$
c_6	302.8	$-3.4\text{x}10^{-8}$	3.6	$-1.4\text{x}10^{-3}$

However, also in this case the Prony's method allows to identify the right trend of the experimental curves (Fig. 5.6) even if the maximum temperature value is not always properly reconstructed (Tabs 5.11 and 5.12).

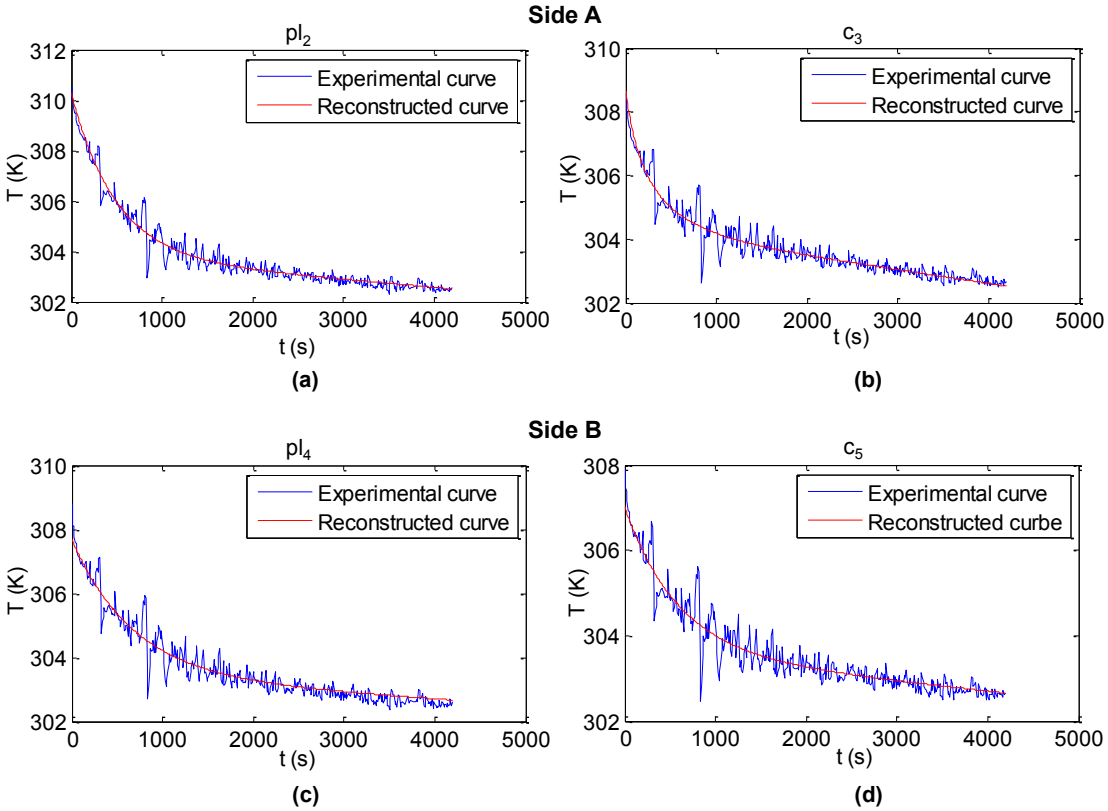

Figure 5.6: Comparison between the experimental curve of defect pl_2 (a), c_3 (b), pl_4 (c) and c_5 (d) of Fig. 5.5 and the reconstructed theoretical curve by using the Prony's method.

Table 5.11: Experimental, $T_{exp}(t=0)$, and reconstructed, $T_{rec}(t=0)$, maximum temperature values and their difference, Δ, for the defects of Fig. 5.5a.

Defect Side A	T_{exp} **(**t**=0) [K]**	T_{rec} **(**t**=0) [K]**	Δ **[K]**
sound	307.1	306.0	1.1
pl_1	308.7	308.0	0.7
pl_2	310.5	310.3	0.2
pl_3	307.9	307.5	0.4
c_1	307.8	304.1	3.7
c_2	308.3	306.8	1.5
c_3	308.6	308.6	0.0

Table 5.12: Experimental, $T_{exp}(t=0)$, and reconstructed, $T_{rec}(t=0)$, maximum temperature values and their difference, Δ, for the defects of Fig. 5.5b.

Defect Side B	T_{exp} **(**t**=0) [K]**	T_{rec} **(**t**=0) [K]**	Δ **[K]**
sound	307.5	307.0	0.5
pl_4	308.8	307.7	1.1
pl_5	308.4	307.3	1.1
c_5	307.9	307.0	0.9
c_6	307.5	306.4	1.1

In conclusions, nevertheless the proposed interpretative approach could provide an appropriate inversion scheme of thermographic data, the problem of interpretation of the exponential parameters in terms of quantities that characterize the investigated structures is still open and currently in progress.

Conclusions

The research activity was focused on development, testing and application of numerical methods for solving the thermal problem and analyzing thermographic data in the architectural and environmental fields.

First, numerical codes, based on the Conservative Finite Difference approximation, were implemented in MATLAB environment to solve the 1D and 2D heat conduction problem. The codes allow to simulate the thermal response of homogeneous and in-homogeneous media by varying both geometry (i.e, width, depth) and thermal properties (i.e., thermal conductivity, specific heat, density) of the constituent materials and initial internal temperature distribution.

The developed numerical codes were tested on IRT measurements performed on two specimens consisting of one- and two-layer structures with several defects of different geometry and materials. Synthetic thermal curves were calculated and compared with the experimental thermal transients of different surface pixels of the investigated structures. The numerical analysis has demonstrated that the application of the developed codes can provide, with a good level of accuracy, joint information about both nature and geometry of anomaly sources of homogeneous or multi-layer structures, even if IRT data come from short times of heating and cooling phases, which do not allow for reaching of the thermal equilibrium.

Then, the codes have been applied to IRT data for architectural and environmental studies.

As concern the application to architectural structures, IRT data acquired on two different archaeological buildings were analyzed. The first quantitative analysis refers to data acquired in the Marcus Fabius Rufus' House, located in the archaeological area of Pompeii (Naples, Italy). The numerical study has permitted to discriminate layered structures and to identify the state of conservation of the constituent materials [Di Maio et al., 2012b].

The second application in architectural field regards a quantitative analysis of IRT data acquired on the east wing of the Dome of Magdeburg (Magdeburg, Germany). The numerical study allowed to characterize the plaster score made of three layers, i.e. a lime wash layer that overlaps two lime mortar layers. In particular, depth, thickness and nature of the thermal anomaly sources were defined and attributed mainly to degradation of the lime mortar layer at different depths. Such results have provided helpful indications for restoration work planning [Di Maio et al., 2013].

As concern the applications to environmental field, a numerical analysis was performed in the attempt to reproduce the thermal evolution of the Phlegraean magmatic system (Naples, Italy) during the last 40,000 years. A careful study on the initial values of the physical properties of the Phlegraean caldera geological structure was conducted. The main finding is that temperatures measured in the geothermal wells drilled inside the caldera at depths larger than 2,500 m can be reproduced under the assumption of conduction heat propagation, while hydrothermal convection has to be taken into account to properly describe heat propagation above such depths.

Furthermore, a new method for analyzing long-term time series of IRT data recorded by a permanent network located at the monitoring station of Pisciarelli (Campi Flegrei) was developed. The proposed approach is based on the evaluation of temperature changes of the investigated area during the last seven years. So far, downward trends at the end of 2007 and during the entire year 2012 are identified, and possible correlations with the results from different analyses and GPS elevation data are work in progress.

Finally, a new approach to invert IRT data based on the Prony's method has been proposed. The application of the method to synthetic and experimental thermal data showed significant correlations between the exponential coefficients coming from the

Prony's analysis and the physical properties of test homogeneous materials. The interpretation of the inverted results is more difficult when inhomogeneous structures are considered and the search for possible correlations is currently in progress.

Appendix A1

LU factorization and solution of a tridiagonal system

The equations system obtained by the application of the 1D implicit conservative FD formulation can be represented in matrix form as $A \cdot v = d$, where:

$$A = \begin{bmatrix} b_1 & c_1 & 0 & 0 & 0 & 0 \\ a_2 & b_2 & c_2 & 0 & 0 & 0 \\ 0 & a_3 & b_3 & c_3 & 0 & 0 \\ 0 & 0 & \ddots & \ddots & \ddots & 0 \\ 0 & 0 & 0 & a_{N-1} & b_{N-1} & c_{N-1} \\ 0 & 0 & 0 & 0 & a_N & b_N \end{bmatrix}, \qquad v = \begin{bmatrix} T_1^n \\ T_2^n \\ T_3^n \\ \vdots \\ T_{N-1}^n \\ T_N^n \end{bmatrix}, \qquad d = \begin{bmatrix} d_1 \\ d_2 \\ d_3 \\ \vdots \\ d_{N-1} \\ d_N \end{bmatrix}.$$

This system can be solved by using LU factorization with backward substitution. The coefficient matrix is positive definite (and symmetric in the case of conduction or diffusion without convection), so LU factorization without pivoting can be used [Recktenwald, 2004].

Given the coefficient matrix A, L and U have to be found such that $A=L \cdot U$. They have the form:

$$L=\begin{bmatrix} e_1 & & & & & \\ a_2 & e_2 & & & & \\ & a_3 & e_3 & \ddots & & \\ & & \ddots & \ddots & & \\ & & & a_{N-1} & e_{N-1} & \\ & & & & a_N & e_N \end{bmatrix}; \qquad U=\begin{bmatrix} 1 & f_1 & & & & \\ & 1 & f_2 & & & \\ & & 1 & f_3 & & \\ & & & \ddots & \ddots & \\ & & & & 1 & f_{N-1} \\ & & & & & 1 \end{bmatrix}.$$

To evaluate the nonzero terms of the L and U matrices, the product of such coefficients is set equal to the corresponding coefficients of A:

$$e_1 = b_1$$

$$e_1 f_1 = c_1$$

$$a_2 = a_2$$

$$a_2 f_1 + e_2 = b_2$$

$$e_2 f_2 = c_2$$

$$a_i = a_i$$

$$a_i f_{i-1} + e_i = b_i \quad i = 2, \dots, N-1$$

$$e_i f_i = c_i$$

$$\vdots$$

$$a_n = a_n$$

$$a_n f_n + e_n = b_n$$

The obtained linear system of n equations is solved providing the e_i and f_i coefficients:

$$f_1 = c_1/e_1 = c_1/b_1$$

$$e_2 = b_2 - a_2/f_1$$

$$f_2 = c_2/e_2$$

$$e_i = b_i - a_i/f_{i-1}$$

$$f_i = c_i / e_i$$

$$e_N = b_N - a_N f_{N-1} .$$

Since $A=L \cdot U$, the system $A \cdot v=d$ is equivalent to $(L \cdot U) \cdot v=d$ or $L \cdot (U \cdot v)=d$. Setting $w=U \cdot v$, the system of equations becomes $L \cdot w=d$. Since L is a lower triangular matrix, the first system, $L \cdot w=d$, is solved with a *forward substitution.* Then, the second system, $U \cdot v=w$, is solved with a *backward substitution* since U is upper triangular matrix.

The application of the *Backward Time, Centered Space* (BTCS) scheme to heat equation provides a coefficient matrix that does not change from time step to time step [Recktenwald, 2004]. Consequently, the factors L and U are obtained only once at the beginning of the numerical simulation, while the two triangular systems are solved at each time step using the following relations:

- Forward substitution to solve $L \cdot w = d$:

  $w_1 = d_1 / e_1$;

  $w_i = (d_i - a_i w_{i-1}) / e_i \quad i = 2, \dots, N$

- backward substitution to solve $U \cdot v = w$:

  $v_n = w_n$;

  $v_i = w_i - f_i w_{i+1} \quad i = N-1, \dots, 1.$

References

Aamodt L.C., Maclachlan Spicer J.W., Murphy J.C., *Analysis of characteristic thermal transit times for time-resolved infrared radiometry studies of multilayered coatings*. Journal of Applied Physics, 68: 6087-98, 1990.

AGIP, *Modello geotermico del Sistema flegreo(Sintesi)*. Report, Servizi centrali per l'Esplorazione, Settore Esplorazione e Ricerca, San Donato Milanese, Italia, pp. 23, 1987.

Ames W.F., *Numerical methods for partial differential equations*. Academic Press Inc., Boston, Massachusetts, third edition, pp. 451, 1992.

Angot F., *Complements de Mathematique*. Masson, Paris, France, sixth edition, pp. 865, 1958.

Apiñaniz E., Mendioroz A., Salazar A., Celorrio R., *Analysis of the Tikhonov regularization to retrieve thermal conductivity depth-profiles from infrared thermography data*. Journal of Applied Physics, 108: 064905, 2010.

Arienzo I., Moretti R., Civetta L., Orsi G., Papale P., *The feeding system of Agnano-Monte Spina eruption Campi Flegrei (Italy): Dragging the past into present activity and future scenarios*. Chemical Geology, 270: 135-147, 2010.

Aubert M., *Practical evaluation of steady heat discharge from dormant active volcanoes: case study of Vulcarolo fissure (Mount Etna, Italy).* Journal of Volcanology and Geothermal Research, 92: 413–29, 1999.

Aubert M., Diliberto S., Finizola A., Chébli Y., *Double origin of hydrothermal convective flux variations in the Fossa of Vulcano (Italy)*. Bulletin of Volcanology, 70: 743-51, 2008.

Avdelidis N.P. and Moropoulou A., *Emissivity considerations in building thermography*, Energy and Buildings, 35: 663-7, 2003.

Avdelidis N.P. and Moropoulou A., *Applications of infrared thermography for the investigation of historic structures*. Journal of Cultural Heritage, 5: 119-27, 2004.

Babbage C., *Observation on the temple of Serapis at Pozzuoli near Naples*. R. and J.E. Taylor, London, England, 1847.

Bai W. and Wong B.S., *Evaluation of defects in composite plates under convective environments using lock-in thermography*. Measurement Science and Technology, 12: 142-50, 2001.

Bailey J.E., Harris A.J.L., Dehn J., Calvari S., Rowland S., *The changing morphology of an open lava channel on Mt. Etna*. Bulletin of Volcanology, 68: 497-515, 2006.

Barberi, F., Innocenti, F., Lirer, L., Munno, R., Pescatore, T., Santacroce, R., *The Campanian Ignimbrite: a major prehistoric eruption in the Neapolitan area Italy*. Bulletin Volcanologique, 41: 10-31, 1978.

Barberi F., Corrado G., Innocenti F., Luongo G., *Phlegrean Fields 1982-1984: Brief chronicle of a volcano emergency in a densely populated area.* Bulletin of Volcanology, 47: 175-85, 1984.

Bennett Jr C.A. and Patty R.R., *Thermal wave interferometry: a potential application of the photoacoustic effect.* Applied Optics, 21: 49-54, 1982.

Bianco F., Del Pezzo E., Saccorotti G., Ventura G., *The role of hydrothermal fuids in triggering the July–August 2000 seismic swarm at Campi Flegrei, Italy: Evidence from seismological and mesostructural data*, Journal of Volcanology Geothermal Research, 133: 229-46, 2004.

Bison P.G., Ceseri M., Fasino D., Inglese G., *Active Infrared Thermography in Nondestructive Evaluation (2): Detection of Hidden Damages from Real Data*. Proceedings of SIMAI congress, Ragusa, Italy, 2006.

Bonafede M., Dragoni M., Boschi E., *Heat diffusion and size reduction of a spherical magma chamber*. Bulletin of Volcanology, 47: 343-47, 1984.

Bonafede M., and Mazzanti M., *Modelling gravity variations consistent with ground deformation in the Campi Flegrei caldera (Italy)*. Journal of Volcanology and Geothermal Research, 81: 137-57, 1998.

Breislak S. *Essai Mineralogiques sur le Solfatare de Pouzzole; Part 3, Observations sur l'Exterieur du 1792. Cratere de la Solfatare*. Giaccio, Naples, Italy, 170-77, 1792.

Brink A., Maierhofer Ch., Rölling M.H., Wiggenhauser H., *Application of quantitative impulse thermography for structural evaluation in civil engineering – Comparison of experimental results and numerical simulations*. Proceedings of 6th QIRT conference, Dubrovnik, Croatia, eds. D. Balageas, G. Busse and G.M. Carlomagno, 35-40, 2002.

Bromley C.J, Van Manen S.M, Mannington W., *Heat flux fom steaming ground: reducing uncertainties*. Proceeding of 36th workshop on Geothermal Reservoir Engineering, Stanford, California, 2011.

Bucur V., *Techniques for high resolution imaging of wood structure: a review*. Measurement Science and Technology, 14: R91-R98, 2003.

Busse G., *Optoacoustic phase angle measurement for probing a metal*, Applied Physics Letters. 35: 759-60, 1979.

Busse G., *Nondestructive Evaluation of Polymer Materials*, NDT&E International, 27: 253-62, 1994.

Busse G. and Rosencwaig A., *Subsurface imaging with photoacoustics*. Applied Physics Letters, 36: 815-6, 1980.

Busse G., Wu D., Karpen W, *Thermal wave imaging with phase sensitive modulated thermography*. Journal of Applied Physics, 71: 3962-5, 1992.

Caliro S., Chiodini G., Moretti R., Avino R., Granieri D., Russo M., Fiebig J., *The origin of the fumaroles of La Solfatara (Campi Flegrei, South Italy)*, Geochimica et Cosmochimica Acta, 71: 3040-55, 2007.

Calvari S., Coltelli M., Neri M., Pompilio M., Scribano V., *The 1991–1993 Etna eruption: chronology and lava flow-field evolution*. Acta Vulcanologica, 4: 1-14, 1994.

Carlomagno G.M. and Berardi P.G., *Unsteady thermotopography in non-destructive testing*. Proceeding of 3rd Infrared Information Exchange, St. Louis, Missouri, ed. Warren C., 33-40, 1976.

Carlomagno G.M. and Meola C., *Infrared thermography in the restoration of cultural properties*. Proceedings of SPIE, Thermosense XXIII, Orlando, Florida, eds. A.E. Rozlosnik and R.B. Dinwiddie, 4360: 203-14, 2001.

Carlomagno G.M. and Meola C., *Comparison between thermographic techniques for frescoes NDT*, NDT&E International, 35: 559-65, 2002.

Carlomagno G.M., Di Maio R., Fedi M., Meola C., *Integration of infrared thermography and high-frequency electromagnetic methods in archaeological surveys*. Journal of Geophysics and Engineering, 8: S93-S105, 2011.

Carslaw H.S. and Jaeger J.C., *Conduction of heat in solids*. Clarendon Press, Oxford, England, second edition, pp. 510, 1986.

Carriere R., Moses R.L., *High resolution radar target modeling using a modified Prony estimator.* Antennas and Propagation, IEEE Transactions, 40: 13-8, 1992.

Cassignol C., Gillot P., *Range and effectiveness of unspiked potassium-argon dating: experimental ground work and application.* Numerical dating in stratigraphy, ed. Odin G.S., Wiley, New York, 160-79, 1982.

Catena A. and Catena G., *Use of a Hand-held Thermal Imager to Detect Cavities and Rotten Tissue in Trees*. Proceedings of 1st Annual Meeting of the Remote Sensing and Photogrammetry Society, London, England, 2001.

Celorrio R., Mendioroz A., Salazar A., *Characterization of vertical buried defects using lock-in vibrothermography: II. Inverse problem*. Measurement Science and Technology, 24: 065602, 2013.

Chen Z-J and Zhang S-Y, *Thermal Depth Profiling Reconstruction by Multilayer Thermal Quadrupole Modeling and Particle Swarm Optimization*. Chinese Physics Letters, 27: 026502, 2010.

Chiodini G., Todesco M., Caliro S., Del Gaudio C., Macedonio G., Russo M., *Magma degassing as a trigger of bradyseismic events: The case of Phlegrean Fields (Italy)*, Geophysics Research Letters, 30: 1434, 2003.

Chiodini G., Granieri D., Avino R., Caliro S., Costa A., Werner C., *Carbon dioxide diffuse degassing and estimation of heat release from volcanic and hydrothermal systems*. Journal of Geophysical Research, 110: B08204, 2005.

Chiodini G., Vilardo G., Augusti V., Granieri D., Caliro S., Minopoli C., Terranova, C., *Thermal monitoring of hydrothermal activity by permanent infrared automatic stations: results obtained at Solfatara di Pozzuoli, Campi Flegrei (Italy)*. Journal of Geophysical Research, 112: B12206, 2007.

Chiodini G., Caliro S., Cardellini C., Granieri D., Avino R., Baldini A., Donnini M., Minopoli C., *Long term variations of the Campi Flegrei (Italy) volcanic system as revealed by the monitoring of hydrothermal activity*, Journal of Geophysics Research, 115: B03205, 2010.

Chiodini G., Caliro S., De Martino P., Avino R., Gherardi F., *Early signals of new volcanic unrest at Campi Flegrei caldera? Insights from geochemical data and physical simulations*. Geology, 40: 943-46, 2012.

Chuang C.W. and Moffatt D.L., *Natural Resonances of Radar Targets Via Prony's Method and Target Discrimination*. Aerospace and Electronic Systems, IEEE Transactions, 12: 583-9, 1976.

Ciocia C. and Marinetti S., *In-situ emissivity measurement of construction materials.* E-book proceedings of 11th QIRT conference, Naples, Italy, Paper QIRT2012-168, 2012.

Civetta L., Orsi, G. Pappalardo, L. Fisher, R.V. Heiken G., Ort M., *Geochemical zoning, mingling, eruptive dynamics and depositional processes - the Campanian Ignimbrite, Campi Flegrei caldera, Italy*. Journal of Volcanology and Geothermal Research, 75: 183-219, 1997.

Clauser C. and Huenges E., *Thermal Conductivity of Rocks and Minerals, Rock Physics and Phase Relations - a Handbook of Physical Constants*. AGU Reference Shelf , 3, 1995.

Corrado G., De Lorenzo S., Mongelli F. Tramacere A., Zito G.M., *Surface heat flow density at the Phlegrean Fields caldera, Southern Italy*. Geothermics, 16: 358-373. 1998.

Crisci G.M., Di Gregorio S., Rongo R., Scarpelli M., Spataro W., Calvari S., *Revisiting the 1669 Etnean eruptive crisis using a cellular automata model and implications for volcanic hazard in the Catania area*. Journal of Volcanological and Geothermal Research, 123: 211-230, 2003.

D'Oriano C., Poggianti E., Bertagnini A., Cioni R., Landi P., Polacci M., Rosi M., *Changes in the eruptive style during the A.D. 1538 Monte Nuovo eruption (Phlegrean Fields, Italy): the role of syn-eruptive crystallization*. Bulletin of Volcanology, 67: 601-21, 2005.

De Natale G., Troise C., Pingue F., Mastrolorenzo G., Pappalardo L., Battaglia M., Boschi E., *The Campi Flegrei caldera: unrest mechanisms and hazards*. Geological Society, London, England, Special Publications, 2006.

De Siena L., Del Pezzo E., Bianco F., *Seismic attenuation imaging of Campi Flegrei: Evidence of gas reservoirs, hydrothermal basins, and feeding systems*. Journal of geophysical research, 115: B09312, 2010.

De Vita S., Orsi G., Civetta L., Carandente A., D'Antonio M., Deino A., Di Cesare T., Di Vito M. A., Fisher R. V., Isaia R., Marotta E., Necco A., Ort M. H., Pappalardo L., Piochi M., and Southon J., *The Agnano-Monte Spina eruption (4100 years BP) in the restless Campi Flegrei Caldera (Italy)*. Journal of Volcanology and Geothermal Research, 91: 269-301, 1999.

De Vivo B., Rolandi G., Gans P.B., Calvert A., Bohrson W.A., Spera F.J., Belkin H.E., *Nex constraints on the pyroclastic eruptive histpry of the Campanian volcanic Plain (Italy)*. Mineralogy and Petrology, 73:47-65, 2001.

De Vivo B., Petrosino P., Lima A., Rolandi G., Belkin H.E., *Research progress in volcanology in Neapolitan area, southern Italy: a review and alternative views*. Mineralogy and Petrology, 99: 1-28, 2010.

De Witt D.P and Nutter G.D, *Theory and practice of radiation thermometry*. John Wiley and Sons, New York, USA, pp. 1152, 1988.

Deino A.L., Orsi G., De Vita S., Piochi M., *The age of the Neapolitan Yellow Tuff caldera-forming eruption (Campi Flegrei caldera – Italy) assessed by $^{40}Ar/^{39}Ar$ dating method*. Journal of Volcanology and Geothermal Research, 133: 157-70, 2004.

Del Gaudio G., Ricco C., Aquino I., Brandi G., Serio C., Siniscalchi V., *Misure di livellazione di precisione e dati tiltmetrici per il controllo delle deformazioni del suolo ai Campi Flegrei*. Osservatorio Vesuviano, Naples, Open File Report, 4, 2005.

Del Gaudio, C., Aquino I., Ricciardi G.P., Ricco C., Scandone R., *Unrest episodes at Campi Flegrei: A reconstruction of vertical ground movements during 1905-2009*, Journal of Volcanology and Geothermal Research, 195: 48-56, 2010.

Del Negro C., Fortuna L., Herault A., Vicari A., *Simulation of the 2004 lava flow at Etna volcano using the magflow cellular automata model*. Bulletin of Volcanology, 70: 805-12, 2008.

Della Vedova B., Mongelli F., Pellis G., Squarci P., Taffi L., Zito G., *Heat-flow map of Italy*. CNR - International Institute of Geothermal Research, ed. Gori L.d., Pisa, Italy, 1991.

Dellino P., Isaia R., La Volpe L., Orsi G., *Statistical analysis of textural data from complex pyroclastic sequence: implication for fragmentation processes of the Agnano-Monte Spina eruption (4.1 ka) at Phlegraean Fields (Southern Italy)*. Bulletin of Volcanology, 63: 443-61, 2001.

Dellino P., Isaia R., La Volpe L., Orsi G., *Interaction between particles trasported by fallout and surge in the deposits ofAgnano-Monte Spina eruption (Campi Flegrei, Southern Italy)*. Journal of Volcanology and Geothermal Research, 133: 193–210, 2004.

Delpech P.M., Krapez J.C., Balageas D.L., *Thermal defectometry using the temperature decay rate method*. Proceedings of 2th QIRT conference, Paris, France, eds. D. Balageas, G. Busse and G.M. Carlomagno, 201-6, 1994.

Desideri U., Leonardi D., Proietti S., *Application of infrared thermography to study behaviour of biogas captation wells*. Proceeding of 11th International Waste Management and Landfill Symposium, Cagliari, Italy, 2007.

Di Carlo A., *Telethermography with thermostimulus in the study of temporal arteritis*. Infrared Physics & Technology, 46: 57-61, 2004.

Di Maio R. and Patella D., *Interpolation of induced polarization transients by the Generalized Cole-Cole relaxation model*. Theory and Practice of Applied Geophysics, 4: 379-93, ISBN: 3-528-06396-3, 1990.

Di Maio R., Patella D., Petrillo Z., Siniscalchi A., Cecere G., De Martino P., *Application of electric and electromagnetic methods to the definition of the Campi Flegrei caldera (Italy)*. Annals of Geophysics, 43: 1590-1815, 2000.

Di Maio R., Fedi M., La Manna M., Grimaldi M., Pappalardo U., *The contribution of the geophysical prospecting in the reconstruction of the buried ancient environments of the Marcus Fabius Rufus house (Pompeii, Italy)*. Archaeological Prospection, 17: 259-69, 2010.

Di Maio R., Meola C., Grimaldi M., Pappalardo U., *New insights for conservation of Villa Imperiale (Pompeii, Italy) through non-destructive exploration*. International Journal of Architectural Heritage, 6: 562-78, doi:10.1080/15583058.2011.593392, 2012a.

Di Maio R., Mancini C., Meola C., Piegari E., *Numerical modelling of architectonic structures' thermal response. Laboratory and in-situ data analysis*. E-book proceedings of 11th QIRT conference, Naples, Italy, Paper QIRT2012-349, 2012b.

Di Maio R., Maierhofer C., Mancini C., Piegari E., *A quantitative analysis of IRT data for the evaluation of plaster degradation at the Dome of Magdeburg (Germany)*. Proceeding of EGU General Assembly 2013, Vienna, Austria, 2013.

Di Renzo V., Arienzo I., Civetta L., D'Antonio M., Tonarini S., Di Vito M., Orsi G., *The magmatic feeding system of the Campi Flegrei caldera: Architecture and temporal evolution*. Chemical Geology, 281: 227-41, 2011.

Di Vito M., Lirer L., Mastrolorenzo G., Rolandi G., *The Monte Nuovo eruption (Campi Flegrei, Italy)*. Bullettin of Volcanology, 49: 608-15, 1987.

Di Vito M., Isaia R., Orsi G., Southon J., De Vita S., D'Antonio M., Pappalardo L., Piochi M., *Volcanism and deformation since 12,000 years at the Campi Flegrei caldera (Italy)*. Journal of Volcanology and Geothermal Research, 91: 221-46, 1999.

Dumoulin J., Ibos L., Marchetti M., Ludwig S., Mazioud A. *Active Infrared Thermography applied to detection and characterization of non-emergent defects on asphalt pavement*. Proceedings of Non-Destructive Testing in Civil Engineering, Nantes, France, 2009.

Dvorak J.J. and Mastrolorenzo G., *The mechanism of recent vertical crustal movements in Campi Flegrei caldera, Southern Italy*. Geology Society of America, Special Paper, pp. 263, 1991.

ENEL, *Inventario delle risorse geotermiche nazionali, Regione Campania: schede pozzi*. Untà nazionale geotermica, Pisa, Italy, pp. 245, 1987.

Fedele F., Giaccio B., Isaia R., Orsi G., *Ecosystem impact of the Campanian Ignimbrite eruption in Late Pleistocene Europe*. Quaternary Research, 57: 420-24, 2002.

Fisher R.V., Orsi G., Ort,M., Heiken G., *Mobility of a large-volume pyroclastic flow-emplacement of the Campanian ignimbrite, Italy*. Journal of Volcanology and Geothermal Research, 56: 205–220, 1993.

Fletcher C.A.J., *Computational techniques for fluid dynamics.* Springer-Verlag, New York, New York, second edition, pp. 401, 1988.

Forbes J.D., *Physical notice in the Bay of Naples; Number 5, on the Temple of Jupiter Serapis at Pozzuoli and the phenomena which it exhibits*. Edinburgh Journal of Science New Series, 1: 260-86, 1829.

Fourier J., *Théorie Analytique de la Chaleur*. Didot F., Paris, France, pp.300, 1822.

Frank, D.G., *Hydrothermal Processes at Mount Rainier*. Ph.D. dissertation, University of Seattle, Washington, pp. 195, 1985.

Friedman J.D., Williams D.L., Frank D., *Structural and heat flow implications of infrared anomalies at Mt. Hood, Oregon, 1972-1977*. Journal of Geophysical Research, 87: 2793-803, 1982.

Galmiche F., Vallerand S., Maldague X., *Pulsed phase thermography with the wavelet transform*. Proceedings of QNDE, Montréal, Canada, eds. Thompson D.O and Chimenti D.E., 19A: 609-15, 2000.

Gaudin D. Beauducel F., Allemand P., Delacourt C., Finizola A., *Heat flux measurement from thermal infrared imagery in low-flux fumarolic zones: Example of the Ty fault (La Soufrière de Guadeloupe)*. Journal of Volcanology and Geothermal Research, 267: 47-56, 2013.

Gerasimova E., Plekhov O., Bayandin Y., Naimark O., Freynd G., *Identification of breast cancer using analysis of thermal signals by nonlinear dynamics methods*. E-book proceedings of 11th QIRT conference, Naples, Italy, Paper QIRT2012-190, 2012.

Gerya T.V., *Introduction to numerical geodynamic modelling*. Cambridge University Press, Cambridge, England, pp. 345, 2010.

Giberti G., Moreno S., Sartoris G., *Thermal history of Phlegraean Fields (Italy) in the last 50,000 years: a schematic numerical model*. Bulletin of Volcanology, 47: 331-41, 1984.

Glorieux C., Li Voti R., Thoen J., Bertolotti M., Sibilia C., *Photothermal depth profiling: analysis of reconstruction errors.* INVERSE PROBLEMS, 15: 1149-63, 1999.

Grimaldi M., *VII 16 Insula Occidentalis 22. Casa di M. Fabius Rufus*. Pompei (Regiones VI–VII), eds. Aoyagi M., Pappalardo U., Insula Occidentalis, 257-418, 2006.

Grinzato E., Bison P.G, Bressan C. and Mazzoldi A., *NDE of frescoes by infrared thermography and lateral heating*. Proceedings of 4th QIRT conference, Lodz, Poland, eds. D. Balageas, G. Busse and G.M. Carlomagno, 64-70, 1998.

Grinzato E., Bison P.G., Marinetti S., *Monitoring of ancient buildings by the thermal method*. Journal of Cultural Heritage, 3: 21-9, 2002.

Grinzato E., Vavilov V., Bison P.G., Marinetti S., *Hidden corrosion detection in thick metallic components by transient IR thermography*. Infrared Physics & Technology, 49: 234-8, 2007.

Große Ophoff M., Hoffmeier L., Real W., Weinmann A., *Umwelt Kultur Schutz, Innovationen zur Erhaltung des Kulturerbes im Osten Deutschlands*, Edition Leipzig, pp. 304, 2011.

Gunther R.T., *The submerged Greek and Roman Foreshore near Naples*. Archaeologia, 58: 499–560, 1903.

Harris A.J.L. and Maciejewski A.J.H., *Thermal surveys of the Vulcano Fossa fumarole field 1994-1999: evidence for fumarole migration and sealing*. Journal of Volcanology and Geothermal Research, 102: 119-47, 2000.

Harris A.J.L., Flynn L.P., Matias O., Rose W.I., Cornejo J., *The evolution of an active silicic lava flow field: an ETM+ perspective*. Journal of Volcanology and Geothermal Research 135: 147-68, 2004.

Harris A.J.L., Lodato L., Dehn J., Spampinato L., *Thermal characterization of the Vulcano fumarole field*. Bulletin of Volcanology, 71: 441-58, 2009.

Heriansyah R. and Abu-Bakar S.A.R., *Defect Depth Estimation in Passive Thermography Using Neural Network Paradigm*, Proceeding of 6th International Conference on Circuits, Systems, Electronics, Control & Signal processing, Cairo, Egypt, 421-5, 2007.

Hildebrand F.B., *Introduction to Numerical Analysis*. McGraw-Hill, New York, New York, second edition, pp.704, 1974. Hooshmand H., Hashmi M., Phillips E.M., *Infrared thermal imaging as a tool in pain management - An 11 year study: Part I of II*. Thermology International, 11: 53-65, 2001a.

Hooshmand H., Hashmi M., Phillips E.M., *Infrared thermal imaging as a tool in pain management - An 11 year study: Part II Clinical applications*. Thermology International, 11: 117-29, 2001b.

Ibarra-Castanedo C., *Quantitative subsurface defect evaluation by Pulsed Phase Thermography: depth retrieval with phase.* Ph.D. Thesis, Laval University, 2006.

Ibarra-Castanedo C., Galmiche F., Darabi A., Pilla M., Klein M., Ziadi A., Vallerand S., Pelletier J.F., Maldague X., *Thermographic nondestructive evaluation: overwiew of recent progress*. Proceeding of SPIE, Thermosense XXV, eds. Cramer K.E. and X. Maldague, 5073: 450-9, 2003.

Ibarra-Castanedo C. and Maldague X., *Pulsed Phase Thermography Reviewed*, QIRT Journal, 1: 47-70, 2004.

Ibarra-Castanedo C., Bendada A., Maldague X., *Image and signal processing techniques in pulsed thermography*. GESTS International Transactions on Computer Science and Engineering, 22: 89-100, 2005.

Ibarra-Castanedo C., Genest M., Piau J.M., Guibert S., Hakim Bendada A., Maldague X., *Chapter 14: Active Infrared Thermography Techniques for the Nondestructive Testing of Materials*. In: Ultrasonic and Advanced Methods for Nondestructive Testing and Material Characterization, ed. Chen C.H., World Scientific Publishing, pp. 325-48, 2007a.

Ibarra-Castanedo C., Bendada A., Maldague M., *Thermographic Image Processing for NDT*. Proceeding of 4th Conferencia Panamericana de END, Buenos Aires, Argentina, 2007b.

Kaneko T. and Wooster M.J., *Landsat infrared analysis of fumarole activity at Unzen volcano. Time series comparison with gas and magma fluxes*. Journal of Volcanology and Geothermal Research, 89: 57-64, 1999.

Karpen W., Wu D., Steegmuller R., Busse G., *Depth profiling of orientation in laminates with local lock-in thermography.* Proceeding of 3th QIRT conference, Sorrento, Italy, Balageas D., Busse G. and Carlomagno G.M., 281-6, 1994.

Krapez J.C. and Cielo P., *Thermographic Nondestructive Evaluation: Data Inversion Procedures, I: 1D Analysis*. Research in Nondestructive Evaluation, 3: 81-100, 1991a.

Krapez J.C., Maldague X., Cielo P., *Thermographic Nondestructive Evaluation: Data Inversion Procedures, II: 2D Analysis and Experimental Results*. Research in Nondestructive Evaluation, 3: 101-24, 1991b.

Kuo P.K., Feng Z.J., Ahmed T., Favro L.D., Thomas R.L. and Hartikainen J., *Parallel thermal wave imaging using a vector lockin video technique.* Photoacoustic and Photothermal Phenomena, 58: 415-8, 1988.

Lanari R., Berardino P., Borgström S., Del Gaudio C., De Martino P., G. Fornaro, S. Guarino, Ricciardi G.P., Sansosti E., Lundgren P., *The use of IFSAR and classical geodetic techniques for caldera unrest episodes: Application to the Campi Flegrei uplift event of 2000*. Journal of Volcanology and Geothermal Research, 133: 247-60, 2004.

Lang S., Kurkjian A., McClellan J., Morris C., Parks T., *Estimating slowness dispersion from arrays of sonic logging waveforms*. GEOPHYSICS, 52: 530-544, 1987.

Lega M. and Napoli M.R.A., *Aerial infrared thermography in the surface waters contamination monitoring*. Desalination and water Treatment, 23: 141-51, 2010.

Lega M., Kosmatka J., Ferrara C., Russo F., Napoli R.M.A., Persechino G., *Using advanced aerial platforms and infrared thermography to track environmental contamination*. Environmental Forensics, 13: 332-8, 2012.

Lehto A., Jaarinen J., Tiusanen T., Jokinen M., Luukkala M., *Magnitude and phase in thermal wave imaging*. Electronics Letters, 17: 364-5, 1981.

Li Voti R., Sibilia C., Bertolotti M., *Photothermal Depth Profiling by Thermal Wave Backscattering and Genetic Algorithms*. International Journal of Thermophysics, 26: 1833-48, 2005.

Lirer L., Luongo G., Scandone R.*, On the volcanological evolution of Campi Flegrei.* EOS Transactions of the American Geophysical Union, 68: 226–34, 1987.

Lopez P., Sahli H., Vilarino D. L., Cabello D., *Detection of perturbations in thermal IR signatures: an inverse problem for buried land mine detection*. Proceedings of Nondestructive Evaluation and Health Monitoring of Aerospace Materials and Composites II, San Diego, California, eds. Gyekenyesi A.L. and Shull P.J., SPIE5046: 242-252, 2003.

Lyell C., *Principles of Geology*. J. Murray, London, England, eleventh edition, pp. 164-79, 1872.

Macedonio G. and Tammaro U. (eds*), Rendiconto sull' attività di sorveglianza anno 2003*. Osservatorio Vesuviano, Naples, Italy, 2005.

Maclachlan-Spicer W., Kerns W.D., Aamodt L.C., Murphy J.C., *Time-resolved infrared radiometry (TRIR) of multilayer organic coatings using surface and subsurface heating*. Proceedings of SPIE, Thermosense XIII, Orlando, Florida, ed. Baird G.S., 1467: 311-21, 1991.

Maierhofer C., Brink A., Röllig M., Wiggenhauser H., *Detection of shallow voids in concrete structures with impulse thermography and radar*. NDT&E International, 36: 257-63, 2003.

Maierhofer C., Wiggenhauser H., Brink A., Röllig M., *Quantitative numerical analysis of transient IR-experiments on buildings*. Infrared Physics & Technology, 46: 173-80, 2004.

Maierhofer C., Brink A., Rollig H., Wiggenhauser H., *Quantitative Impulse-Thermography as non-destructive testing method in civil engineering - Experimental results and numerical simulations*. Construction and Building Materials, 19: 731-7, 2005.

Maierhofer C., Arndt R., Röllig M., Rieck C., Walther A., Scheel H., Hillemeier B., *Application of impulse-thermography for non-destructive assessment of concrete structures*. Cement & Concrete Composites 28: 393-401, 2006.

Maldague X., *Introduction to NDT by active infrared thermography*. Materials Evaluation, 6: 1060-73, 2002.

Maldague X. and Marinetti S., *Pulse Phase Infrared Thermography.* Journal of Applied Physics, 79: 2694-8, 1996.

Manduchi G., Marinetti S., Bison P., Grinzato E., *Application of neural network computing to thermal non-destructive evaluation*. Neural Computing & Applications, 6: 148-57, 1997.

Marcuzzi F., Marinetti S., *Efficient reconstruction of corrosion profiles by infrared thermography*. Journal of Physics: Conference Series, 124: 012033, 2008.

Marple S.L., *Digital spectral analysis with applications*. Prentice-Hall, Englewood Cliffs, New Jersey, pp. 492, 1987.

Martini M., *L'attività recente dei Campi Flegrei*. ARC, 5: 7-12, 2013.

Matsushima N., Kazahaya K., Saito G., Shinohara H., *Mass and heat flux of volcanic gas discharging from the summit crater of Iwodake volcano, Satsuma-Iwojima, Japan, during 1996–1999*. Journal of Volcanology and Geothermal Research, 126: 285-301, 2003.

Mazioud A., Ibos L., Dumoulin J., *Detection of a mosaic hidden behind a plaster layer by IR thermography*. E-book proceedings of 10th QIRT conference, Quebec City, Canada, Paper QIRT2010-087, 2010.

Meola C., *Infrared thermography of masonry structures*. Infrared Physics and Technology, 49: 228-33, 2007.

Meola C. and Carlomagno G.M., *Recent advances in the use of infrared thermography*. Measurement Science and Technology, 15: R27-R58, 2004.

Meola C., Carlomagno G.M., Squillace A., Prisco U., Morace R.E., *Analysis of composites with infrared thermography*. Macromolecular Symposia, 228: 273-86, 2005.

Minkina W. and Dudzik S., *Infrared Thermography: Errors and Uncertainties*. John Wiley & Sons, Ltd, Chichester, England, pp. 212, 2009.

Morhange C., Bourcien M., Laborel J., Giallanella C., Goiran J.P., Crimaco L., Vecchi L., *New data on historical relative sea level movements in Pozzuoli Phlaegrean Fields, Southern Italy*. Physics and Chemistry of the Earth, A24: 349-54, 1999.

Morton K.W. and Mayers D.F., *Numerical solution of partial differential equations: an introduction*. Cambridge University Press, Cambridge, England, second edition, pp. 278, 1994.

Niccolini A., *Tavola Cronologica–metrica delle Varie Altezze Tracciate della Superficie del Mare fra la Costa di Amalfi ed il Promontorio di Gaeta nel Corso di Diciannove Secoli*. Flautina, Naples, Italy, 11-52, 1839.

Niccolini A., *Descrizione della gran terma puteolana volgarmente detta Tempio di Serapide*. Stamperia Reale, Naples, Italy, 1845.

Oppenheimer C., Francis P.W., Rothery D.A., Carlton R.W.T., Glaze L.S., *Infrared image analysis of volcanic thermal features: Láscar Volcano, Chile, 1984–1992*. Journal of Geophysical Research, 98: 4269-86, 1993.

Orsi G. and Scarpati C., *Stratigrafia e dinamica eruttiva del Tufo Giallo Napoletano*. Bollettino Gruppo Nazionale Vulcanologia, 2: 917-30, 1989.

Orsi G., De Vita S., Di Vito M., *The restless, resurgent Campi Flegreu nested caldera (Italy): constraints on its evolution and configuration*. Journal of Volcanology and Geothermal Research, 74: 179-214, 1996.

Orsi G., Di Vito M.A., Isaia R., *Volcanic hazard assessment at the Campi Flegrei Caldera*. Bulletin of Volcanology, 66: 514-30, 2004.

Osiander R., Maclachlan-Spicer J.W., Amos M., *Thermal inspection of S_iC/S_iC ceramic matrix composites*. Proceeding of SPIE, Thermosense *XX*, Orlando, Florida, eds. Snell J.R. and Wurzbach R.N., 3361: 339-49, 1998.

Pappalardo L., Civetta L., D'Antonio M., Deino A., Di Vito M., Orsi G., Carandente A., De Vita S., Isaia R., Piochi M., *Chemical and Sr-isotopical evolution of the Phlegraean magmatic system before the Campanian Ignimbrite and the Neapolitan Yellow Tuff eruptions*. Journal of Volcanology and Geothermal Research, 91: 141-66, 1999.

Pappalardo L., Civetta L., De Vita S., Di Vito M.A., Orsi G., Carandente A., Fisher R.V., *Timing of magma extraction during the Campanian Ignimbrite eruption (Campi Flegrei caldera)*. Journal of Volcanology and Geothermal Research, 114: 479-97, 2002.

Parascandola A., *I Fenomeni Bradisismici del Serapeo di Pozzuoli, Naples*, privately published, 1947.

Patankar S.V., *Numerical heat transfer and fluid flow*. McGraw-Hill, New York, New York, pp. 214, 1980.

Patella D., Pinto I., Castricone M., Di Maio R., *Fitting IP discharges by Prony's method*. Bollettino di Geofisica Teorica ed Applicata, 29: 33-41, 1987.

Patella D. and Di Maio R., *On the analysis of Cole-Cole relaxation transients in the induced polarization prospecting method*. Theory and Practice of Applied Geophysics, 3: 205-19, ISBN: 3-528-06369-6, 1989.

Peltier A. , Finizola A., Douillet G.A., Brothelande E., Garaebiti E., *Structure of an active volcano associated with a resurgent block inferred from thermal mapping: The Yasur-Yenkahe*

volcanic complex (Vanuatu). Journal of Volcanology and Geothermal Research, 243-244: 59-68, 2012.

Pickering S. and Almond D., *Matched excitation energy comparison of the pulse and lock-in thermography NDE techniques*. NDT&E international, 41: 501-9, 2008.

Pieri D.C. and Abrams M., *ASTER watches the world's volcanoes: a new paradigm for volcanological observations from orbit*. Journal of Volcanology and Geothermal Research, 135: 13-28, 2004.

Pilla M., *A Novel Contrast Method for Pulse Thermography Data*, Ph.D. Thesis, Politecnico di Milano, 2002.

Pilla M., Klein M., Maldague X., Salerno A., *New Absolute Contrast for Pulsed Thermography*. E-book proceedings of 6th QIRT conference, Dubrovnik, Croatia, Paper QIRT2002-004, 2002.

Pinkerton H. and Wilson L., *Factors controlling the lengths of channel-fed lava flows*. Bulletin of Volcanology, 56: 108-20, 1994.

Piochi M., Kilburn C.R.J., Di Vito M.A., Mormone A., Tramelli A., Troise C., De Natale G. *The volcanic and geothermally active Campi Flegrei caldera: an integrated multidisciplinary image of its buried structure*. International Journal of Earth Sciences (Geologische Rundschau), 103: 401-421, 2014.Prony R., *Essai ésperimental et analytique: sur les lois de la dilatabilité des fluids élastique et sur celles de la force expansive de la vapeur de l'alkool, à différentes temperatures*. Journal de l'École Polytechnique Floréal et Plairial, 1: 24-76, 1795.

Rantala J., Wu D., Busse G., *Amplitude modulated lock-in vibrothermography for NDE of polymers and composites*. Research in Nondestructive Evaluation, 7: 215-28, 1996.

Recktenwald G.W., *Finite-Difference approximations to the Heat Equation*. Mechanical Engineering, 10: 1-27, 2004.

Rinaldi A.P., Todesco M., Bonafede M., *Hydrothermal instability and ground displacement at the Campi Flegrei caldera*. Physics of the Earth and Planetary Interiors, 178: 155-161, 2010.

Rodríguez F.L., de Paulo Nicolau V., Oshiro H., Tancredi D., *Non-destructive evaluation of composite materials by pulsed-phase thermography: depth inversion*. Proceeding of 21st Brazilian Congress of Mechanical Engineering, Natal, Brazil, 2011.

Rolandi G., Bellucci F., Heizler M.T., Belkin H.E., De Vivo B., *Tectonic controls on the genesis of ignimbrites from the Campanian Volcanic Zone, southern Italy*. Mineralogy and Petrology, 79: 3-31, 2003.

Rosi M. and Sbrana A., *Phlegrean Fields*. CNR, Quaderni de La ''Ricerca Scientifica'', 114: 1-175, 1987.

Rosi M., Vezzosi L., Aleotti P., De Cenzi M., *Interaction between caldera collapse and eruptiove dynamics during the Campanian Ignimbrite eruption, Phlegrean Fields, Italy*. Bulletin of Volcanology, 57: 541-54, 1996.

Saccorotti G., Petrosino S., Bianco F., Castellano M., Galluzzo D., La Rocca M., Del Pezzo E., Zaccarelli L., Cusano P., *Seismicity associated with the 2004–2006 renewed ground uplift at Campi Flegreicaldera, Italy*. Physics of the Earth and Planetary Interiors, 165: 14–24, 2007.

Saintey M.B. and Almond D.P., *An artificial neural network interpreter for transient thermography image data*. NDT&E International, 5: 291-5, 1997.

Sanchez-Gasca J.J. and Chow J.H., *Performance comparison of three identification methods for the analysis of electromechanical oscillations*. Power System, IEEE Transactions, 14: 995-1002, 2002.

Sansivero F., Vilardo G., De Martino P., Augusti V., Chiodini G., *Campi Flegrei volcanic surveillance by thermal IR continuous monitoring*. E-book proceedings of 11th QIRT conference, Naples, Italy, Paper QIRT2012-333, 2012.

Sava H.P. and McDonnel J.T.E, *Modified forward-backward overdetermined Prony method and its application in modelling heart sounds*. IEE Proceedings – Vision, Image and Signal Processing, 142: 375-80, 1995.

Sava H.P. and McDonnel J.T.E, *Spectral composition of heart sounds before and after mechanical heart valve implantation using a modified forward-backward Prony's method.* Biomedical Engineering, IEEE Transactions, 43(7): 734-42, 1996.

Scacchi A., *La regione vulcanica fluorifera della Campania (*II Edition). Memorie del Regio Comitato Geologico d'Italia, Firenze, Italy, second edition, 1890.

Scandone R., Bellucci F. Lirer L., Rolandi G., *The structure of the Campanian Plain and the activity of Neapolitan Volcanoes*, Journal of Volcanology and Geothermal Research, 48: 1-31, 1991.

Scarpati C., Cole P., Perrotta A., *The Neapolitan Yellow Tuff - a large volume multiphase eruption from Campi Flegrei, Southern Italy*. Bulletin of Volcanology, 55(5): 343-56, 1993.

Scarpati C., Perrotta A., Lepore S., Calvert A., *Eruptive history of Neapolitan volcanoes: constraints from 40Ar–39Ar*. Geological Magazine 150: 412-25, 2013.

Sekioka M. and Yuhara K., *Heat-flux estimation in geothermal areas based on heat balance of ground surface*. Journal of Geophysical Research, 79: 2053-8, 1974.

Shepard S.M., *Advances in Pulsed Thermography*. Proceeding of SPIE, Thermosense XXVIII, Orlando, Florida, eds. Rozlosnik A.E. and Dinwiddie R.B., 4360: 511-5, 2001.

Siegel R. and Howell J., *Thermal radiation heat transfer*. CRC press, Washington, USA, fourth edition, pp. 864, 2001.

Singh S., *Application of Prony analysis to characterize pulsed corona reactor measurements*. Master Thesis, University of Wyoming, 2003.

Smith V.C., Isaia R., Pearce N.J.G., *Tephrostratigraphy and glass compositions of post-15 kyr Campi Flegrei eruptions: implications for eruption history and chronostratigraphic markers*. Quaternary Science Reviews, 30: 3638-60, 2011.

Spampinato L., Calvari S., Oppenheimer C., Boschi E., *Volcano surveillance using infrared cameras*. Earth-Science Reviews, 106: 63-91, 2011.

Sun J.G., *Analysis of Pulses Thermography methods for defect depth prediction*. Journal of Heat Transfer, 128: 329-38, 2006.

Susa M., Ibarra-Castanedo C., Maldague X., Bendada A., Svaic S., Boras I., *Pulse thermography applied on a complex structure sample: comparison and analysis of numerical and experimental results*. Proceeding of IV Pan American Conference in END, Buenos Aires, Argentina, 2007.

Thành N.T., Sahli H., Hào D. N., *Finite-difference methods and validity of a thermal model for landmine detection with soil property estimation*. Geoscience and Remote Sensing, 45: 656–74, 2007.

Thomas R.L., Pouch J.J., Wong Y.H., Favro L.D., Kuo P.K., Rosencwaig A., *Subsurface flaw detection in metals by photoacoustic microscopy*. Journal Applied Physics, 51: 1152-6, 1980.

Todesco M., Chiodini G., Macedonio G., *Monitoring and modelling hydrothermal fluid emission at La Solfatara (Phlegrean Fields, Italy). An interdisciplinary approach to the study of diffuse degassing*. Journal of Volcanology and Geothermal Research, 125: 57-79, 2003.Trasatti E., Casu F., Giunchi C., Pepe S., Solaro G., Tagliaventi S., Berardino P., Manzo M., Pepe A., Ricciardi G. P., Sansosti E., Tizzani P., Zeni G., Lanari R., *The 2004-2006 uplift episode at Campi Flegrei caldera (Italy): constraints from SBAS-DInSAR ENVISAT data and Bayesian source inference*. Geophysics Research Letters, 35: L07308, 2008.

Treagoureas A., Beneito A., Berne P., Gonze M.A., Sabroux J.C., Savanne D., Pokryszka Z., Tauzieade C., Cellier P., Laville P., Milward R., Arnaud A., Levy F., Burkhalter R., *Comparison of seven methods for measuring methane flux at a municipal solid waste landfill site*. Waste Management and Research, 17: 453-8, 1999.

Troise C., De Natale G., Pingue F., Obrizzo F., Martino P.D., Tammaro U., Boschi E. *Renewed ground uplift at campi flegrei caldera (Italy): New insight on magmatic processes and forecast*. Geophysical Research Letters, 34: L03301, 2007.

Trudnowski D.J., Smith J.R., Short T.A., Pierre D.A., *An application of Prony methods in PSS design for multimachine systems*. Power Systems, IEEE Transactions, 6: 118-26, 2002.

Vavilov V.P., Kauppinen T., Grinzato E., *Thermal characterization of defects in buildings envelopes using long square pulse and slow thermal wave techniques.* Research in Nondestructive Evaluation, 9: 181-200, 1997.

Vilardo G., Alessio G., and Luongo G., *Analysis of the Magnitude-Frequency Distribution for the 1983– 1984 Earthquake Activity of Campi Flegrei, Italy*. Journal of Volcanology and Geothermal Research, 48: 115–25, 1991.

Vilardo G., Chiodini G., Augusti V., Granieri D., Caliro S., Minopoli C.and C. Terranova, *The permanent thermal infrared network for the monitoring of hydrothermal activity at the Solfatara and Vesuvius volcanoes*. Conception, verification, and application of innovative techniques to study active volcanoes, eds. Marzocchi W. and A. Zollo, INGV: 483-95, 2008.

Vollmer M. and Möllmann C.P., *Infrared Thermal Imaging: Fundamentals*, *Research and Applications*. Wiley-VCH Verlag GmbH, Weinheim, Germany, pp. 593, 2010.

Vosteen H.D. and Schellschmidt R., *Influence of temperature on thermal conductivity, thermal capacity and thermal diffusivity for different types of rock*. Physics and Chemistry of the Earth, 28: 499-509, 2003.

Weiser M., Röllig M., Arndt R., Erdmann B., *Development and test of a numerical model for pulse thermography in civil engineering*. Heat and Mass Transfer, 46: 1419-28, 2010.

Wiscombe W.J. and Evans J.W., *Exponential-sum fitting of radiative transmission functions.* Journal of Computational Physics, 24, 416-44, 1977.

Wisniewski M., Lindow S., Ashworth E., *Observations of ice nucleation and propagation in plants using infrared video thermography*. Plant Physiology, 113: 327-34, 1997.

Wohletz K., Orsi G., De Vita S., *Eruptive mechanisms of the Neapolitan Yellow Tuff nterpreted from stratigraphic, chemical and granulometric data*. Journal of Volcanology and Geothermal Research, 67: 263-90, 1995.

Wohletz K., Civetta L., Orsi G., *Thermal evolution of the Phlegrean magmatic system*. Journal of Volcanology and Geothermal Research, 91: 381-414, 1999.

Wright R., Flynn L.P., Harris A.J.L., *Evolution of lava flow-field at Mount Etna, 27-28 October 1999, observed by Landsat 7 ETM+.* Bulletin of Volcanology, 63: 1-7, 2001.

Wu D., *Lockin thermography for defect characterization in veneered wood*. Proceeding of 2th QIRT conference, Sorrento, Italy, eds. Balageas D., Busse G. and Carlomagno G.M., 298-302, 1994.

Wu D., Rantala J., Karpen W., Zenzinger G,. Schönbach B., Rippel W., Steegmüller R., Diener L., Busse G., *Applications of lockin-thermography methods*. Proceeding of QNDE, New York, New York, eds. Thompson D.O and Chimenti D.E., 15: 511-8, 1996a.

Wu D., Salerno A., Malter U., Aoki R., Kochendorfer R., Kachele P.K., Woithe K., Pfister K., Busse G., *Inspection of aircraft structural components using lock-in thermography.* Proceeding of 3rd QIRT conference*,* Paris, France, eds. Balageas D., Busse G. and Carlomagno G.M., 251-6, 1996b.

Wu D. and Busse G., *Lock-in Thermography for NonDestructive Evaluation of Materials*, Revue Générale de Thermique**,** 37: 693-703, 1998.

Wu D., Zweschper Th., Salerno A., Busse G., *Lock-in thermography for nondestructive evaluation of aerospace structures.* NDT.net, 3, 1998.

Xiao J., Xie X., Han Y., Wu J., *Dynamic tracking of low-frequency oscillations with improved Prony method in wide-area measurement system*. Proceedings of IEEE Power Meeting, Denver, Colorado, 1: 1104-9, 2004.

Yuhara K., Ehara S., Tagomori K., *Estimation of heat discharge rates using infrared measurements by a helicopter-borne thermocamera over the geothermal areas of Unzen Volcano, Japan*. Journal of Volcanology and Geothermal Research, 9: 99-109, 1981.

Yuhara K., Sekioka M., Ehara S., *Infrared measurement on Satsuma-Iwojima island, Kagoshima, Japan, by helicopter-borne thermocamera*. Archiv für Meteorologie, Geophysik und Bioklimatologie, 27: 171-81, 1978.

Zimanowski B., Wohletz K., Dellino P., Büttner R., *The volcanic ash problem*. Journal of Volcanology and Geothermal Research, 122: 1-5, 2003.

Zollo A., Maercklin N., Vassallo M., Dello Iacono D., Virieux J., Gasparini P., *Seismic reflections reveal a massive melt layer feeding Campi Flegrei caldera*. Geophysicical Research Letters, 35: L12306, 2008.

Zore Z., Stanec M., Zore I.F., Metejčić A., Boras I., Rodić A., Švaić S., *Thermography in Breast Cancer Diagnosis*. E-book proceedings of 11th QIRT conference, Naples, Italy, Paper QIRT2012-247, 2012.